

University of Rzeszów
Faculty of Mathematics and Natural Sciences

Tatyana Sizyuk

**Modeling and simulation of laser produced plasma sources for EUV
photons generation**

**Dissertation completed with the requirements for the
PhD- Degree in Physics under the supervision
of Prof. Ahmed Hassanein, the Paul L. Wattlelet Professor
of Nuclear Engineering, Purdue University**

Rzeszów, 2014

ACKNOWLEDGMENTS

First of all, I would like to express my sincere gratitude and deep appreciation to my advisor Prof. Ahmed Hassanein. He is the greatest teacher in my life who has taught me thinking, allowed me believing in myself, and without whom all this would have never been possible.

I would also like to express my infinite thanks to Prof. Igor Tralle for his huge work in arrangement of this defense, for his helpful advice, and for his care and patience. I also thank the Faculty of the Department of Physics of Rzeszów University for their appreciation and help in facilitating my defense of this thesis.

I would like to say many thanks to my husband Prof. Valeryi Sizyuk for his continuous valuable discussions and debates related to the plasma physics processes and the challenges of computational physics. His understanding and patience during the course of my thesis preparation is greatly appreciated. I also very much appreciate the useful simulating discussions and the close interactions with my colleagues at our CMUXE at Purdue University.

I also would like to say few words of appreciation and thanks to my closest people in my life. First, my thankfulness to my great son for his encouragements and willingness to help and support my efforts during this work. My deepest gratitude to my mom for her wisdom, kindness, and patience. Her understanding and support always give me great pleasure in my life. Many thanks also to my brother who has served as a model in understanding the value of life and the persistence to succeed.

Finally, I would like to sincerely thank the college of engineering and the school of nuclear engineering at Purdue University for their support and help during my preparation of this thesis.

CONTENTS

List of Acronyms.....	4
List of Figures.....	5
1. Introduction.....	14
1.1 The history of EUVL.....	14
1.2 Choice of optimal material.....	18
1.3 Review of EUV sources: DPP, LPP, and LDP.....	18
1.4 Integrated modeling for the solution of the LPP source challenges.....	22
1.5 Summary of applicant's contributions.....	24
2. Description of models and methods.....	27
3.1 General equations set.....	27
2.2 Laser energy absorption.....	30
2.3 Radiation transport.....	32
2.3.1 Traditional models for radiation transport.....	33
2.3.2 Direct numerical solution of RT equation using Gaussian method.....	34
2.3.3 Monte Carlo Radiation Transport.....	40
2.4 Models testing and benchmarking.....	45
3. Modeling, analysis and optimization of LPP sources.....	50
3.1 Effect of laser parameters and geometrical containment on EUV photons output.....	50
3.1.1 Laser wavelength influence.....	50
3.1.2 Target geometry influence on plasma evolution.....	52
3.1.3 Plasma production and containment by multiple laser beams.....	56
3.1.4 Comparative analysis of plasmas created by CO ₂ and Nd:YAG lasers.....	60
3.1.5 Low efficiency of EUV sources from small droplets.....	64
3.2 Complex mechanisms in optimization of dual-beam systems.....	73
3.2.1 Dual-pulse systems as ways for optimization of sources from small droplets..	74
3.2.2 Dependence of laser energy absorption efficiency on plasma conditions.....	76
3.2.3 Influence of laser wavelength and intensity on vaporization dynamics.....	86
3.2.4 Dependence of source location and intensity on plasma conditions.....	96
3.3 Kinetic energies of ions in LPPs and their effect on optic mirrors lifetime.....	100
3.4 Smallest efficient target and opportunities for EUV power increase.....	104
3.4.1 Mass density requirement for the efficient EUV source.....	104
3.4.2 Potentials for EUV power increase.....	108
4. Summary.....	110
5. References.....	116

List of Acronyms

3D	Three dimensional
CE	Conversion efficiency
CMUXE	Center for Materials Under eXtreme Environment
CRE	Collisional-radiative equilibrium
DOF	Depth of focus
DPP	Discharge produced plasma
EUV	Extreme ultraviolet
EUVL	Extreme ultraviolet lithography
HEIGHTS	High Energy Interaction with General Heterogeneous Target Systems
HFS	Hartree-Fock-Slater
HVM	High volume manufacturing
FWHM	Full width at half maximum
IC	Integrated circuit
IF	Intermediate focus
ITMC-DYN	Ion Transport in Materials and Compounds
LDP	Laser-assisted discharge produced plasma
LPP	Laser produced plasma
LTE	Local thermodynamic equilibrium
MCRT	Monte Carlo radiation transport
MHD	Magnetohydrodynamics
MLM	Multilayer mirrors
RTE	Radiation transport equation

List of Figures

Figure 1: Schematic of depth of focus (defined as the distance over which the focus is smallest)

Figure 2: Time-integrated spectral intensity for Ti, Sn, Sm, Ta, and Au [16]

Figure 3: Z scaling of the EUV conversion efficiency near 13 nm or 95 eV [16]

Figure 4: Schematic illustration of the Dense Plasma Focus device [6]

Figure 5: Schematic illustration of laser photons interaction with droplet target and developed plasma plume [18]

Figure 6: Schematic illustration of LDP device [21]

Figure 7: Time scale of dual-beam laser systems illustrates one of the parameters for optimization - delay time between pulses

Figure 8: Schematic illustration of laser energy deposition in 3D computational domain

Figure 9: Calculation of the quanta distribution in cylindrical geometry

Figure 10: Monte Carlo modeling of radiation transport in plasma [18]

Figure 11: Experimental parameters used in modeling for benchmarking

Figure 12: Efficiency of LPP devices using tin planar target. Comparison of experimental and theoretical data [16, 49]

Figure 13: Dependence of CE on CO₂ laser beam intensity in experiments [50] and HEIGHTS modeling [18]

Figure 14: Dependence of CE on Nd:YAG laser intensity both experimentally (CMUXE laboratory) and simulation (HEIGHTS package) [51]

Figure 15: (a) density, (b) temperature, and (c) velocity of tin plasma distributions at 9.0 ns. Single laser case: energy of laser pulse 45 mJ, wavelength 1064 nm

Figure 16: Efficiency of the LPP device as a function of laser beam intensity for three laser wavelengths [52]

Figure 17: Electron temperature and density (white contours) distribution in planar (left) and droplet (right) target models [51]

Figure 18: Radiation fluxes in EUV range in planar (left) and droplet (right) target models [51]

Figure 19: Location and intensity of EUV power collected during 20 ns in 2π sr in planar (left) and droplet (right) target models [51]

Figure 20: Dependence of CE on laser intensity for sphere and planar targets [51]

Figure 21: Location and intensity of EUV power collected during 20 ns in 2π sr in planar (left) and droplet (right) target models [51]

Figure 22: Laser intensity and spot size dependence of CE [51]

Figure 23: Three-beam LPP device, φ - radial angle, and θ - axial angle [52]

Figure 24: Efficiency of the three-beam LPP device as a function of axial angle (green line). Maximum temperature of plasma (red line) [52]

Figure 25: Efficiency of the three-beam LPP device as a function of the total pulses energy for the axial angle $\theta = 30^\circ$ [52]

Figure 26: Temperature fields for (x-y) cross-section in point of maximum temperature at 9 ns. One-laser case corresponds $\theta = 0^\circ$

Figure 27: (a) density, (b) temperature, and (c) velocity of tin plasma distributions at 40 ns in z-x plane [52]

Figure 28: Time profile of laser beam intensity and EUV radiation output for 10.6 μm laser wavelength [56]

Figure 29: Time profile of laser beam intensity and EUV radiation output for 1.06 μm laser wavelength [56]

Figure 30: Experimental time profile of laser beam intensity and modeled EUV radiation output for 10.6 μm laser wavelength [56]

Figure 31: EUV source location and intensity in relation with density and temperature of plasma created by CO_2 laser [57]

Figure 32: EUV source location and intensity in relation with density and temperature of plasma created by Nd:YAG laser [57]

Figure 33: EUV radiation fluxes in plasma created by CO_2 laser [57]

Figure 34: EUV radiation fluxes in plasma created by Nd:YAG laser [57]

Figure 35: Incident and reflected laser energy in plasmas created from tin planar and droplet targets with 30 μm spot size [58]

Figure 36: Comparison of absorbed laser energy in plasmas created from tin planar and droplet targets using laser with small spot size and from planar with large laser spot size [58]

Figure 37: Laser energy absorption at 30 ns in plasma created from tin foil by CO_2 laser. Plasma density is shown by white contours [58]

Figure 38: Laser energy absorption at 30 ns in plasma created from tin droplet by CO_2 laser. Plasma density is shown by white contours [58]

Figure 39: Temperature and density (white contours) distribution at 30 ns in plasma created from tin foil by CO_2 laser [58]

Figure 40: Temperature and density (white contours) distribution at 30 ns in plasma created from tin droplet by CO_2 laser [58]

Figure 41: Location and intensity of the EUV source at 30 ns from the planar target [58]

Figure 42: Location and intensity of the EUV source at 30 ns from the droplet target [58]

Figure 43: Electron temperature and mass density (g/cm^3) distribution at 35 ns in plasma created from 100 μm droplet by CO_2 laser with 30 μm spot (0.6% CE) [61]

Figure 44: Electron temperature and mass density (g/cm^3) distribution at 35 ns in plasma created from 100 μm droplet by CO_2 laser with 50 μm spot (0.9% CE) [61]

Figure 45: Plasma temperature and density (white contours) distribution at 35 ns of CO_2 laser pulse with 220 μm spot diameter [62]

Figure 46: Plasma temperature and density (white contours) distribution at 35 ns of CO_2 laser pulse with 30- μm spot diameter [62]

Figure 47: EUV source from 30- μm droplet heated by CO_2 laser with 30 μm spot size [62]

Figure 48: EUV source from 30- μm droplet heated by CO_2 laser with 50 μm spot size [62]

Figure 49: Location and intensity of the EUV power collected during 150 ns in 2π sr in planar target [18]

Figure 50: Location and intensity of the EUV power collected during 150 ns in 2π sr in spherical target [18]

Figure 51: Laser energy distribution for 100 μm spot size (FWHM), 30 ns duration (FWHM) and $1 \times 10^{10} \text{ W}/\text{cm}^2$ intensity; droplet diameter 30 μm [18]

Figure 52: Mass density distribution of plasma plume from tin droplet of 30 μm diameter [18]

Figure 53: Laser energy absorption at optimized intensities of: 1) 532 nm laser; 2) CO_2 without pre-pulse; 3) CO_2 after pre-pulse [18]

Figure 54: Mass density of plasma plume from the droplet of 30 μm created by 532 nm laser and expanded during 80 ns [18]

Figure 55: The dependence of CE on CO₂ spot size applied after pre-pulse on tin target. For comparison CE of CO₂ laser with 100 μm spot size and 100 μm droplet without pre-pulse is given [18]

Figure 56: CO₂ laser energy absorption in material and in plasma from 30 μm droplet without pre-pulse – 0.45% CE. Gray curve shows laser energy which was absorbed in plasma after reflection, green curve shows reflected laser energy which was not absorbed in evolving plasma [61]

Figure 57: CO₂ laser energy absorption in pre-plasma created from 30 μm droplet by 266 nm laser and expanded during 450 ns – 2.9% CE. Gray curve shows laser energy which was absorbed in plasma after reflection, green curve shows reflected laser energy which was not absorbed in evolving plasma [61]

Figure 58: CO₂ laser energy absorption during pulse in material and plasma from 30 μm droplet without pre-pulse. Laser pulse was used with 30 ns (FWHM) duration and 30 μm (FWHM) spot size [61]

Figure 59: CO₂ laser energy absorption during pulse in pre-plasma created from 30 μm droplet by 266 nm laser and expanded during 450 ns. Laser pulse was used with 30 ns (FWHM) duration and 300 μm (FWHM) spot size [61]

Figure 60: Mass density distribution at the end of pre-pulse laser beam with 1064 nm wavelength and intensity of 10¹⁰ W/cm² [57]

Figure 61: Mass density distribution after 100 ns delay in pre-plasma created by the laser beam with 1064 nm wavelength and intensity of 10¹⁰ W/cm² [57]

Figure 62: Mass density distribution at the end of pre-pulse laser beam with 266 nm wavelength and intensity of 10¹⁰ W/cm² [57]

Figure 63: Mass density distribution after 100 ns delay in pre-plasma created by the laser beam with 266 nm wavelength and intensity of 10^{10} W/cm² [57]

Figure 64: Dependence of evaporation dynamics on pre-pulse laser wavelength at different intensities. Laser beam parameters used are 30 μm spot size and 10 ns duration [57]

Figure 65: Dependence of evaporation dynamics on pre-pulse laser intensity at 1064 nm wavelength. Laser beam parameters used are 30 μm spot size and 10 ns duration [57]

Figure 66: Sn erosion by CO₂ laser with 100 μm spot and 10^{11} W/cm² intensity [61]

Figure 67: Sn erosion by Nd:YAG (1064 nm) laser with 100 μm spot and 10^{11} W/cm² intensity [61]

Figure 68: Radiation to the target from laser and from plasma created by CO₂ laser with intensity of 10^{11} W/cm² [61]

Figure 69: Radiation to the target from laser and from plasma created by Nd:YAG laser with intensity of 10^{11} W/cm² [61]

Figure 70: Dependence of evaporation dynamics on pre-pulse laser beam intensity at 1064 nm wavelength: total evaporated mass in g. Laser beam parameters used are 20 μm spot size and 10 ns [58]

Figure 71: Percentage of evaporated mass from 20 μm droplet. Laser beam parameters used are 20 μm spot size and 10ns duration [58]

Figure 72: Mist density from 50-μm droplet created by pre-pulse laser with 266 nm wavelength, ~10 mJ, 50 μm spot. Dotted line shows initial shape of droplet [20]

Figure 73: Mist density from 50-μm droplet created by pre-pulse laser with 1064 nm wavelength, 400 mJ, 100 μm spot. Dotted line shows initial configuration of fragmented droplet [20]

Figure 74: Vaporization of 50- μm droplet by laser photons and by LPP with 1064 nm wavelength laser, 10 ns FWHM, 400 mJ, 100 μm spot [20]

Figure 75: Mass density evolution of distributed fragments after CO₂ laser pulse heating with total mass equivalent to 50 μm droplet [20]

Figure 76: EUV source collected in 2π sr during 70 ns in plasma created by CO₂ laser without pre-pulse [57]

Figure 77: EUV source collected in 2π sr during 70 ns in plasma created by CO₂ laser with pre-pulse [57]

Figure 78: EUV Source strength and location from 100 μm droplet without pre-pulse; CO₂ laser with 300 μm spot, 30 ns pulse [61]

Figure 79: EUV Source strength and location due to pre-plasma created from 50 μm droplet and expanded during 500 ns; CO₂ laser with 300 μm spot, 30 ns pulse [61]

Figure 80: CE from 30 μm droplet as function of delay between pulses and spot size of CO₂ [57]

Figure 81: Ions kinetic energies of HEIGHTS modeling of planar Sn target; 15 mJ for pre-pulse and 90 mJ for CO₂ laser [20]

Figure 82: Ions kinetic energies in CMUXE experiments from planar Sn target; 15 mJ for pre-pulse and 90 mJ for CO₂ laser [60]

Figure 83: Ions kinetic energies produced by CO₂ in pre-plasma created by Nd:YAG laser

Figure 84: Ions kinetic energies produced by CO₂ in vacuum chamber conditions

Figure 85: MLM surface response to Sn ions with Gaussian distribution of energies around 50 eV [20]

Figure 86: MLM surface response to Sn ions with Gaussian distribution of energies around 2.5 keV [20]

Figure 87: Mass density distribution developed by 266 nm laser from 50 μm droplet at optimum delay time for efficient coupling with CO₂ laser with 500 μm spot size [20]

Figure 88: Mass density distribution developed by 266 nm laser from 20 μm droplet at optimum delay time for efficient coupling with CO₂ laser with 300 μm spot size [20]

Figure 89: Mass density distribution developed by 266 nm laser from 10 μm droplet at optimum delay time for efficient coupling with CO₂ laser with 200 μm spot size [20]

Figure 90: Mass density distribution after pre-pulse (10 ns FWHM) (left) and 200 ns delay (right). Pre-plasma was created from 20 μm droplet by laser beam with 266 nm wavelength and intensity of 2×10^{10} W/cm² [58]

Figure 91: CE from 20 μm droplet as function of delay time between the pre-pulse and the main CO₂ laser pulse [58]

Figure 92: EUV source from 50- μm droplet preheated by 266 nm laser and distributed during 500 ns. Main laser is CO₂ with 500 μm spot and 350 mJ [20]

Figure 93: EUV source from 20- μm droplet preheated by 266 nm laser and distributed during 300 ns. Main laser is CO₂ with 300 μm spot and 140 mJ [20]

ABSTRACT

This work describes results of detailed comprehensive modeling, analysis, and optimization of laser-produced plasmas (LPP) for the development of an efficient and debris-free photons source for extreme ultraviolet lithography (EUVL), which is currently the most promising technology for the manufacture of the next generation computer chips. The efficient production and collection of the 13.5 nm photon radiation by the plasma is related to plasma opacity, which depends on level populations of different ionic states, ionization balance, and electron density and temperature. For obtaining the highest conversion efficiency (CE, conversion from laser to EUV in-band, 13.5±1%, radiation) from LPP sources, ideal plasma temperatures and densities should be created for the longest possible period of time with the maximum collectable size. Accurate and comprehensive multidimensional modeling of various processes involved in laser target interaction can help in predictions of plasma behavior and achieving the most favorable conditions for maximizing EUV photons generation and collection. Any potential increase in CE is directly translated into huge economical benefits to consumers and to the semiconductor industries.

1. INTRODUCTION

1.1 The history of EUVL

Ever since the invention of the transistor in 1947 and the integrated circuit (IC) in the late 1950s, semiconductor technology has undergone rapid advances. From a basic technical point of view, developments have been straightforward. They have mainly involved putting more and smaller transistors on integrated circuits. More transistors allow increased functionality, and smaller size allows increased switching speed and less power consumption for each transistor. The whole process has conformed to Moore's law, formulated by Gordon Moore in 1965 [1].

Moore stated that the number of components per IC roughly doubles every second year. In recent decades, the single most important driver of Moore's law has been the inventions of microlithography. This lithographic process generates a semiconductor wafer partially covered with photoresist so that the uncovered regions are available for different kinds of processing, such as etching, ion implantation, or metallization. One of the most important lithographic processes is exposure, when light shines on select parts of the resist and microelectronic elements are formed [2]. Resolution of an optical system, such as projection-lithography system, is traditionally determined by the Rayleigh criterion,

$$Resolution = 0.61 \frac{\lambda}{NA} \quad (1)$$

where λ is the wavelength of the light and NA is the numerical aperture of the optical system ($NA = \sin \theta_{\max}$ for vacuum, where θ_{\max} is the half-angle of the maximum cone of light that can

exit the lens). However, the Rayleigh criterion treats the ability to resolve two point sources and not the printability of semiconductor structures. In this case, the object size is

$$Object\ size = k \frac{\lambda}{NA} \quad (2)$$

where the "*k*-factor" is introduced [2]. According to Eq. (2), the minimum component size can be achieved by increasing the numerical aperture or decreasing the wavelength or *k*-factor. Until about 1993-1994, *k* was stable at 0.8; it has since been decreased to almost 0.4 by using binary masks [3]. As illustrated in Table 1, there has been a continuous increase in *NA* and decrease in wavelength over the years.

Table 1. Progress with lithography instruments [2]

Wavelength, nm	<i>NA</i>	Year	Light Source
436	0.30	1982	Hg arc lamp (g-line)
365	0.45	1990	Hg arc lamp (i-line)
365	0.60	1994	Hg arc lamp (i-line)
248	0.50	1994	Hg arc lamp or KrF excimer laser
248	0.60	1997	KrF excimer laser
248	0.70	1999	KrF excimer laser
193	0.60	1999	ArF excimer laser
193	0.75	2001	ArF excimer laser

Several ways exist for further improvement in semiconductor technology. However, e.g., increasing the *NA* causes problems with the depth of focus (DOF), as illustrated in Fig. 1. The DOF should be larger than the photoresist coating thickness for optimal performance. Alignment difficulties arise when the distance over which the image is sharp is only slightly larger than the

resist thickness. Use of extreme ultraviolet light (wavelength between 10 and 15 nm) in this regard is a promising solution for future semiconductors manufacture.

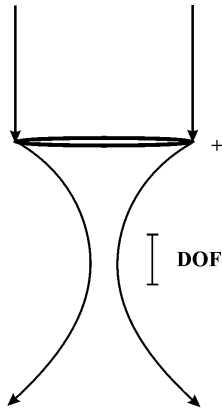


Fig. 1. Schematic of depth of focus (defined as the distance over which the focus is smallest)

The EUV light is absorbed very strongly in most materials, including gases; thus, all optics and the source should be placed into a vacuum. For the same reason lenses cannot be used: optical systems should consist of mirrors. Because reflection of a single surface is very low (about 4%), stacked multilayer mirrors (MLM) are used, for which the reflection adds up. EUVL scanners are based on MLM with a peak reflectivity at 13.5 nm. The choice of using Mo/Si multilayer has determined the needed wavelength to be around 13.5 nm for maximum reflectivity [4].

The EUV light can be generated by several methods: discharge produced plasma (DPP), laser produced plasma (LPP), or hybrid technique, that is, laser-assisted discharge produced plasma (LDP). Each method has its advantages as well as disadvantages. In order to meet the industrial companies' requirements for high volume manufacturing, the EUV source is required to have a power of 250 W at a wavelength of 13.5 nm (2% bandwidth) [5]. Various LPP, DPP, and LDP devices are under investigation by different research groups [6-11]. Currently several of the EUV sources come close to the power level demanded by the commercial chip manufacturers. The CE

of generating EUV radiation is the key factor in successful development of the source. Many additional factors are important to the EUV device efficiency: plasma material, form and size of the radiated area, collectable solid angle, debris amount, etc. Because many physical processes are involved and many technical problems need to be solved when optimizing a particular EUV device, laboratory experiments would be very expensive and time consuming and only computer modeling can generate a complete picture within a reasonable time and at a reasonable cost. Ideally, an integrated physical model should be developed specifically for simulating plasma behavior in DPP and LPP devices. The model should include the atomic physics, hydrodynamics, radiation transport, heat conduction, and EUV production and collection. The EUV source should be modeled comprehensively: from the energy input mechanism; to plasma formation; to EUV output from the pinch or laser target; and to the mirror collector system and reflection. Each physical process should be described accurately with all physics involved, and each physical problem should be solved by most advanced and reliable numerical schemes. The EUV power collected at intermediate focus (IF) of the manufacturer's EUVL stepper in this case can then be predicted most correctly.

This work describes results of comprehensive modeling, analysis, and optimization of LPP devices based on multi-dimensional integrated models included in the HEIGHTS (High Energy Interaction with General Heterogeneous Target Systems) package [6, 12]. This thesis describes HEIGHTS models, compares analysis of various processes occurring in LPP devices and their influence on plasma evolution, and studies the effect of various device parameters on EUV source optimization. Modeling results are presented for tin foils as well as spherical tin droplets as target material. Various parameters of laser beams are studied to maximize the conversion efficiency such as varying laser wavelength, beam intensity, duration, and spot size as well as for

dual-beam systems that further increase the complexity of optimization. Self-consistency for efficient coupling of the first laser for pre-plasma development with the second main laser for EUV photons production was analyzed adjusting all parameters for both laser beams and delay time between pulses. Modeling results were benchmarked against in-house experiments at the Center for Materials Under eXtreme Environment (CMUXE) as well as against various worldwide experimental results.

1.2 Choice of optimal material

In the mid-1980s, O'Sullivan et al. found that a strong narrowband emission is generated from plasma of rare earth elements, that the peak wavelength scales with the atomic number of the element, and that Sn plasma emits a strong band with the spectral peak at 13.5 nm [13]. However, Sn plasma was not considered as EUV source for a long time, since Sn plates generated tremendous amount of debris that significantly contaminated chamber surfaces and decreased lifetime of optical mirrors [14]. A Xe jet was favored as appropriate target material to solve the debris problem. Then EUVL turned into a promising candidate for next generation lithography only after the demonstration of long lifetime of MLM exposed to Xe plasma [15]. However, the required EUV power at the IF jumped during last years from several watts to 100W and higher. The rapid increase of the required EUV power excluded Xe as a candidate for a fuel, because the CE at 13.5 nm of Xe plasma cannot be larger than 1% and it is related to its emissivity peak at 11 nm wavelength.

One of the most comprehensive initial studies of target materials as possible sources for EUV photons production were done by Spitzer, et al. in 1996 [16]. Researchers at Lawrence Livermore National Laboratory performed experimental studies of laser irradiation on several

materials for possible EUV radiation and their results showed that tin is one of the most promising target materials for EUV production around 13.5 nm wavelength. Figure 2 shows time-integrated spectral intensity in plasma produced from several materials by laser with 0.532- μm wavelength and $2 \times 10^{11} \text{ W/cm}^2$ intensity.

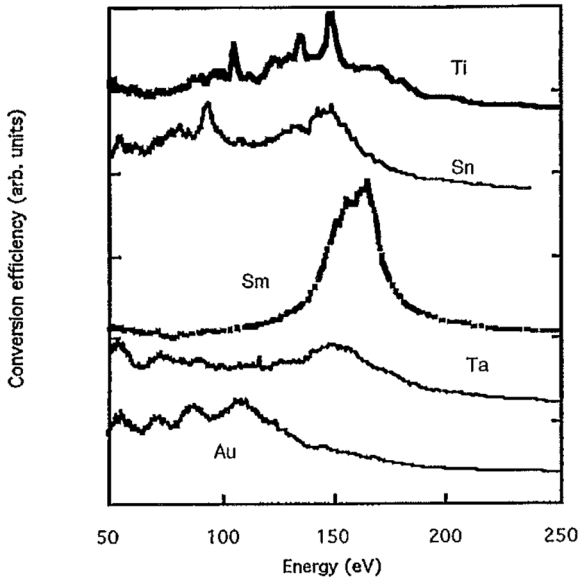


Fig. 2. Time-integrated spectral intensity for Ti, Sn, Sm, Ta, and Au [16]

These experiments examined also the dependence of the CE on the intensity of laser pulse, wavelength, and the pulse width of the laser beam.

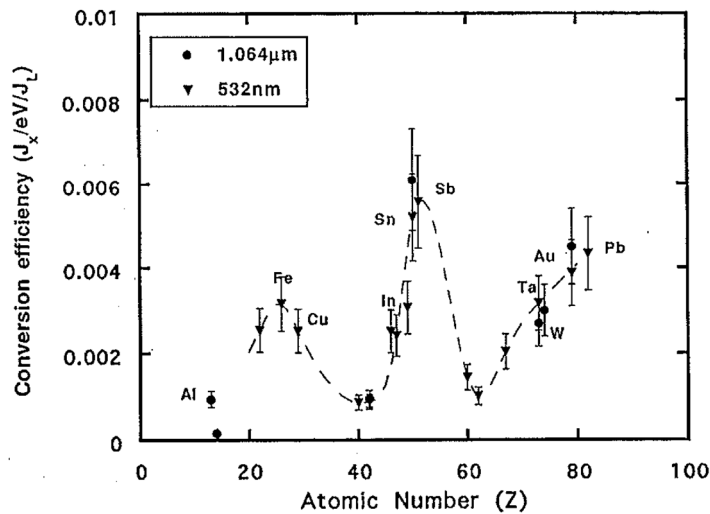


Fig. 3. Z scaling of the EUV conversion efficiency near 13 nm or 95 eV [16]

Figure 3 illustrates the effect of laser wavelength on the CE and Z scaling (dependence on atomic number) of the EUV conversion efficiency near 13 nm or 95 eV. The results are shown in terms of $J/(J \text{ eV})$ [17].

The above-mentioned experiments showed again that Sn plasma could be the most efficient EUV source. In spite of extreme difficulty of avoiding Sn deposition on chamber surfaces, requirements of high CE and high EUV power at IF forced the EUV community to the developments of sources based on Sn and Sn-doped targets.

1.3 Review of EUV sources: DPP, LPP, and LDP

A key challenge for the EUV radiation plasma devices is achieving sufficient brightness to support the throughput requirements of high volume manufacturing (HVM) lithography exposure tools.

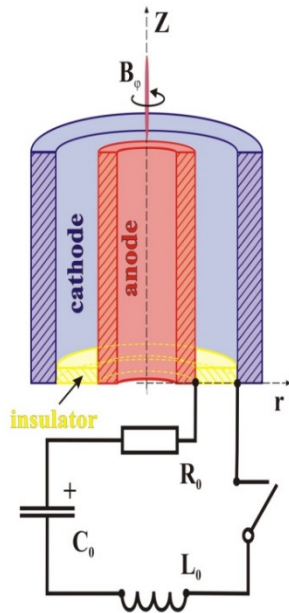


Fig. 4. Schematic illustration of the Dense Plasma Focus device [6]

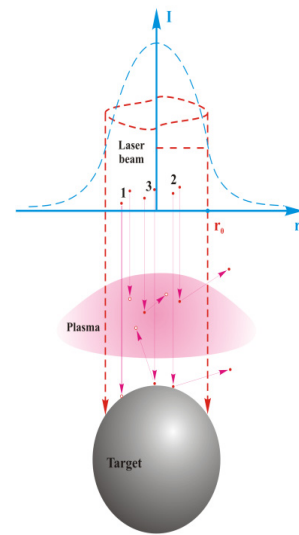


Fig. 5. Schematic illustration of laser photons interaction with droplet target and developed plasma plume [18]

The history of developments for EUVL includes more than twenty years of experimental and theoretical work. Many EUV source concepts were considered at the beginning. They include several devices using DPP (Fig. 4), i.e., dense plasma focus, Z-pinch device, and hollow-cathode tube [6], and devices using LPP (Fig. 5) [7-9]. Several criteria were considered for the optimization of these systems including efficient EUV output and collection, minimized debris production and mitigation, components lifetime, and source brightness for the HVM devices. Compact technologies like dense plasma focus or capillary Z-pinch discharges reached very rapidly fundamental limits as far as power scalability and lifetime were concerned [17].

Recent achievements in the development of bright EUV photon source show two distinctive directions, i.e., laser-assisted discharge plasma (Fig. 6) [11, 17] and dual-beam laser plasma (Fig. 7) [10, 19, 20]. Laser beams are utilized in both cases for target vaporization and the initial creation of matter used for the subsequent ionization and plasma plume optimization for EUV devices (DPP or LPP) for maximum EUV radiation output.

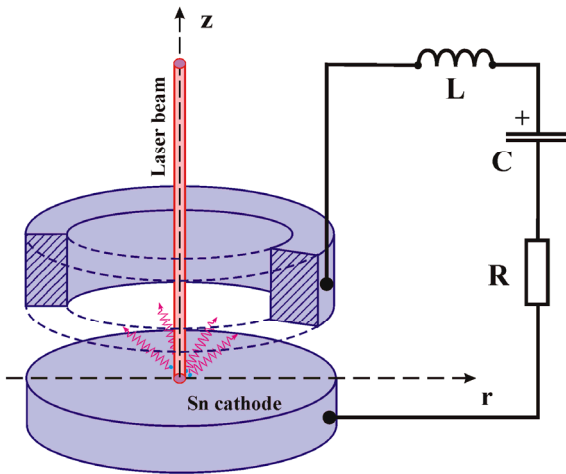


Fig. 6. Schematic illustration of LDP device [21]

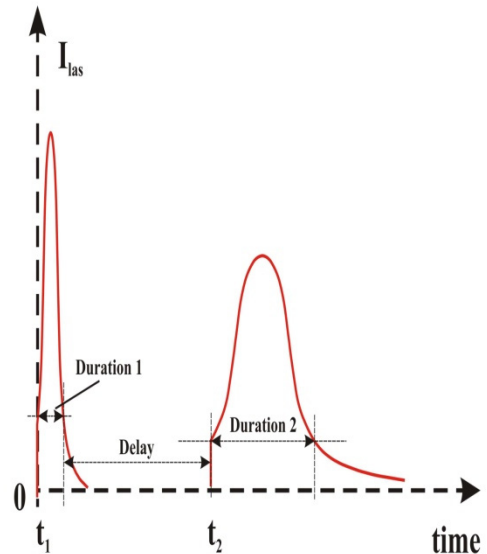


Fig. 7. Time scale of dual-beam laser systems illustrates one of the parameters for optimization - delay time between pulses

Both, LDP and LPP, devices have their own key challenges. The challenges of LDP sources are mostly related to engineering issues such as spatial tolerances, heat removal, capacitor banks [17], as well as lower CE in comparison with LPP devices. Some challenges of LPP sources are related to power scaling versus debris mitigation/mirror lifetime, laser frequency scaling versus droplet minimum stable distance, droplets breakdown, evaporation and expansion processes. Many of these issues are principle challenges for physicists and are still not solved.

1.4 Integrated modeling for the solution of the LPP source challenges

In recent years, LPP processes for the optimization of EUV production were studied using several target materials such as xenon, lithium, and tin [22-24], different target geometry and composition (solid, liquid, cluster grains, etc.) [25, 26], and various laser radiation parameters (radiation power density, wavelength, and pulse duration) [27]. Numerous experiments and computer simulations were made to increase the EUV radiation power. Such analysis also included the use of pre-pulses for formation of optimum plasma plume for EUV production during the main laser pulse [19, 28-30]. The optimization of target geometry for efficient laser energy absorption was analyzed using liquid-jets [31], droplets with tuning of droplet size and laser spot size ratio [32], and the use of planar targets with various thicknesses [33]. The implementation of mass-limited Sn-doped targets for the production of optically thin plasma and minimization of tin debris was also studied [33, 34].

These studies showed various directions in optimization of LPP devices for EUVL. However, the optimum solution for EUV source using LPP devices is still not found. Comprehensive analysis of all parameters and device configurations with consideration of all possible attendant effects is required to predict the ways for achieving efficient EUV photons source for HVM.

Main determining parameters of LPP system with single laser beam include laser wavelength, intensity, spot size, and pulse duration. Optimization of these parameters is significantly influenced by target geometry and composition. Optimization of such complicated systems as LDP and LPP with dual-beam lasers depends on both, characteristics of the initial laser for pre-plasma production and the main energy source for EUV photons generation. Parameters of the initial laser beams for creation of pre-plasma determine the temporal and spatial characteristics of EUV devices. Since combination of many factors in both sources influences the production of radiating media with specific characteristics, optimization of these systems would require significant costly experimental efforts.

The objectives of this thesis are examination of laser produced plasmas in various configurations and possible solutions of the LPP source challenges for EUVL. This work summarizes results of comprehensive analysis of LPP processes, their effect on EUV photons emission and collection and the ways of EUV sources optimization. The work is based on the state-of-the art models and simulations using the HEIGHTS computer package. HEIGHTS simulation package incorporates detailed models in full 3D geometry of multiple laser interactions with various target materials for EUV Lithography as well as for applications in fusion energy, nuclear and high energy physics, directed energy lethality, and surface modifications of materials.

The package includes 3D description of main processes occurred in LPP systems, that allows self-consistent advanced simulations and predictions without any fittings or adjustment parameters. This modeling and simulation included all phases of laser target evolution: from laser/target interaction, energy deposition, target vaporization, ionization, plasma hydrodynamic expansion, thermal and radiation energy redistribution, and EUV photons collection as well as

detailed mapping of photons source size and location. Testing and benchmarking results showed evidence of correct processes implementation. It showed also that accurate computer simulation with sufficient details can be used with confidence to understand, design, and optimize LPP systems and save significant time and cost compared to conducting numerous expensive experiments.

1.5 Summary of applicant's contributions

The author of this thesis contributed significantly to the development of the HEIGHTS comprehensive package, physical models of target response and plasma formation, and utilized the developed models for analysis of laser-produced plasma (LPP) systems as potential light sources for extreme ultraviolet lithography (EUVL).

The main specific contributions to the models development include:

- Implementation of model for target vaporization based on the surface atoms kinetics;
- Development of models for hydrodynamics and thermal conduction for two-component plasma to simulate plasma evolution in presence of ambient gas;
- Development and improvement of algorithms for parallel calculations on multi-processor computers;
- Models benchmarking and debugging for various geometries;
- Upgrade of ITMC-DYN (Ion Transport in Materials & Compounds-Dynamic Version) - Monte Carlo based package designed for simulation of ions/target interactions. This upgrades included modeling of dynamic update of target composition during interaction processes, particles diffusion, chemical erosion, surface segregation, molecular recombination and desorption of gaseous species from the surface. One main purpose of

this development was done to study the effect of energetic ions produces in LPP devices on the photon collection optical mirror system.

The main contributions to the analysis of plasmas in LPP systems and following optimization of EUV sources include:

- Comprehensive self-consistent analysis of plasma physics processes and plasma behavior in various LPP systems;
- Thorough and systematic evaluation and optimization of parameters in LPP devices which influence EUV photons production and collection;
- Prediction, for the first time, of location, intensity and size of EUV source in LPP systems;
- Detailed simulation, for the first time, of the output power limits from the smallest possible spherical targets for the most efficient EUV source;
- Proposition, for the first time, of fourth harmonic of Nd:YAG laser as the most efficient way for target preparation in dual-laser beam systems;
- Explanation, for the first time, of many worldwide experimental results, which were obtained before and after models prediction. These include effect of longer laser wavelengths in combination with small targets on having low efficiency of LPP source; effect of target geometry on the CE of LPP systems; and the effect of delay time between pulses in dual-beam laser systems on plasma characteristics and requirements for the second laser parameters to produce the highest CE;
- Prediction, for the first time, opportunities for potential increase in source power (critical for economic impact of the semiconductor industry) and the challenges related to such source power increase;

- Prediction of degradation of the optical multi-layer mirror systems for EUV photons collection in various LPP systems.

These developments and findings were published in several high-quality high-impact physical journals during the course of this thesis work.

2. DESCRIPTION OF MODELS AND METHODS

Guidance and realistic predictions of experimental results are possible with the state of the art comprehensive modeling that complies with the following important requirements: 1) computer package includes complete set of models for accurate description of all physics processes involved in LPP systems; 2) models are well tested and benchmarked separately in each interaction physics phase as well as in an integrated system; 3) simulations within the package should be able to be extended to reasonable range of experimental parameters without any parametric adjustments or fittings. Accurate modeling and comprehensive understanding of plasma physics processes in LPP should consider details of spatial and temporal input power deposition from laser sources, absorption/reflection of laser light from the surface of solid/liquid target, hydrodynamic evolution of target, absorption/reflection of laser from the evolving target vapor, atomic physics and vapor ionization, absorption/reflection in heated plasma layer, and photon generation and transport during different phases of the evolving target.

2.3 General equations set

The plasma motion dynamics are considered using the set of four conservation laws: mass density, momentum, energy, and magnetic field in the form of

$$\frac{\partial q}{\partial t} + \nabla \cdot \mathbf{F}_q = 0 \quad (3)$$

where q is the conservation parameter and \mathbf{F}_q is the flux of this parameter.

In application to plasma as a continuous, compressible medium, Eq. 3 can be converted to the following expressions for conservation of mass, momentum, and total energy:

$$\begin{aligned}
\frac{\partial \rho}{\partial t} + \nabla \cdot (\rho \mathbf{v}) &= 0, \\
\frac{\partial}{\partial t} \rho \mathbf{v} + \nabla \cdot (\rho \mathbf{v} \mathbf{v} + p_h) &= 0, \\
\frac{\partial e_h}{\partial t} + \nabla \cdot [\mathbf{v}(e_h + p_h)] &= 0,
\end{aligned} \tag{4}$$

where, ρ is the density of plasma, \mathbf{v} is the velocity of plasma, p_h is the hydrodynamic pressure,

and $e_h = \frac{\rho v^2}{2} + e_{\text{int}}$ is the sum of kinetic and internal energy densities of plasma. Because EUV lithography applications are using the LPP devices with the radiation power density of $10^{10} - 10^{12}$ W/cm² the influence of thermo magnetic processes on the plasma behavior was ignored [12].

Because inverse bremsstrahlung is the main mechanism of laser radiation absorption in plasma, the electrons are the main recipient of the laser radiation energy. The maximal energy that can be transmitted from one particle to another particle by elastic interaction is given by [35]

$$E_{\text{max}} = \frac{4m_1 m_2}{(m_1 + m_2)^2} E_1 = C_{tr} E_1 \tag{5}$$

where m_1 and E_1 are the mass and energy of the bullet particle, and m_2 is the mass of the recoil particle. The transmission coefficient for the equal particles (electron-electron or ion-ion) reaches ~ 1.0 . The transmission between electron and ion (Xe^+ for example) is much smaller, $C_{tr}^{ei} \sim 1.6 \times 10^{-5}$. These estimations show that the thermal energy will be transferred from the electrons to the ions with a time delay. The temperature of the electrons will differ from that of the ions because laser heating is a very fast process as a rule. Describing the laser plasma as a mixture of two species (electronic and ionic) is more correct and enables one to explain numerous physical

phenomena of laser heating: electrons overheating and acceleration, magnetic field generation, and so forth.

The HEGHTS model of plasma evolution takes into account the principle of electro-neutrality of plasma. This approach neglects local charge separation and enables one to split the energy equation only. The continuity and pulse equations consider plasma motion as a whole. Moreover, it was found that the best way for total energy control is to solve the energy equation for the whole plasma. The energy of the plasma components is separated by the introduction of an additional energy equation for electrons, which takes into account the mechanism of energy exchange between the ionic and electronic parts.

After taking into account heat conduction and radiation transport, the general form of the hydrodynamic equation set is given in two-temperature approximation by:

$$\begin{aligned}
\frac{\partial \rho}{\partial t} + \nabla \cdot (\rho \mathbf{v}) &= 0 \\
\frac{\partial \rho \mathbf{v}}{\partial t} + \nabla \cdot (\rho \mathbf{v} \mathbf{v} + p_h) &= 0 \\
\frac{\partial e_h}{\partial t} + \nabla \cdot [\mathbf{v}(e_h + p_h) - \lambda_e \nabla T_e - \lambda_i \nabla T_i - \mathbf{S}_{rad}] &= Q_{las} \\
\frac{\partial e_i}{\partial t} + \nabla \cdot [\mathbf{v}(e_i + p_i) - \lambda_i \nabla T_i] &= Q_{ei}
\end{aligned} \tag{6}$$

Here, $e_h = e_e + e_i + e_{kin}$ is the total energy; e_e is the electronic component of the plasma energy, which includes thermal energy of electrons and ionization energy; e_i is the ion component of the plasma energy; and $e_{kin} = \frac{\rho v^2}{2}$ is the kinetic energy of the plasma. Analogous to energy, pressure has electron and ion parts: $p_h = p_e + p_i$. The thermal conduction in the plasma is considered as the combined result of the electron $\lambda_e \nabla T_e$ and ion $\lambda_i \nabla T_i$ components, where λ is

the conductivity coefficient and T is the temperature. The radiation transport process is represented here as flux \mathbf{S}_{rad} and the laser heating source as Q_{las} . The Q_{ei} term is the energy interchange between electrons and ions.

Since the set of equations has convective terms (hydrodynamic flux) and dissipative terms (heat conduction, laser heating, radiation transport, and electron-ion interaction), splitting methods is used in numerical algorithm to separate the hyperbolic and parabolic parts [12, 36-37]. Energy dissipation mechanisms are used as correction factors for the results of the predicted convection fluxes. The energy distribution in domain is considered separately for ions and electrons. Explicit methods and implicit with sparse linear equations solver are implemented for the solution of heat conduction equation in the condensed target and in plasma.

2.2 Laser energy absorption

Monte Carlo method is used for accurate modeling of various energy inputs from laser radiation, i.e., absorption/reflection in solid/liquid target, absorption/reflection in target vapor, and absorption/reflection in plasma layer (Fig. 8). Experimental optical properties were used for laser reflection from liquid tin. Laser photons absorption in vapor was simulated based on the main features of the collision-induced absorption such as a quadratic dependence of the absorption coefficient on the density and a weak dependence on the temperature [38]. Inverse bremsstrahlung absorption was used for simulation of laser photons interaction with plasma. The classical value for the

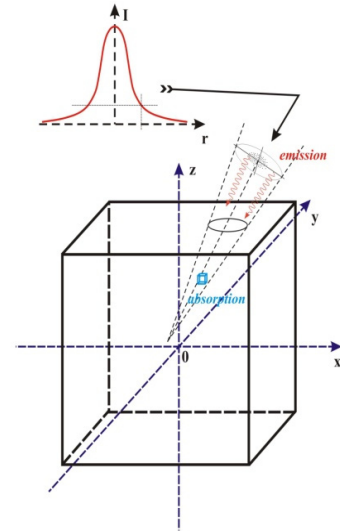


Fig. 8. Schematic illustration of laser energy deposition in 3D computational domain

absorption coefficient k_{abs}^{las} that describes the collisional absorption mechanism is [39]

$$k_{abs}^{las} = \frac{16\pi Z n_e^2 e^6 \ln \Lambda(\nu)}{3c\nu^2 (2\pi m_e k_B T_e)^{3/2} (1 - \nu_p^2/\nu^2)^{1/2}} \quad (7)$$

where e , n_e , m_e , and T_e are the electron charge, density, mass, and temperature, respectively;

Ze is the ionic charge; c is the light speed; ν is the frequency of the laser light; $\nu_p = \sqrt{\frac{n_e e^2}{\pi m_e}}$ is

the plasma frequency; and k_B is the Boltzmann constant. The Coulomb logarithm is given by

[40]

$$\ln \Lambda = \ln \left[\frac{3}{2} \sqrt{\frac{(k_B T_e)^3}{\pi n_e}} \frac{1}{Ze^3} \right] \quad (8)$$

In the simulations this Monte Carlo modeling of laser photons absorption and reflection in liquid/vapor/plasma as well as photon transport in plasma interplays with surface vaporization processes. The vaporized layer above the target surface initializes the processes of laser photons absorption in vapor/plasma that prevents their penetration to target surface. At the same time, radiated plasma photons add their energy to further heating of the droplet and this energy load to the target can be significant from the well-developed hot plasma plume.

Detailed models for target vaporization are based on target thermophysical properties as well as the kinetics of evaporation. The model establishes the connection between the surface temperature and the net atom flux leaving the surface taking into account the possibility of recondensation [41]. The time-dependent net evaporation rate may be approximated by:

$$\begin{aligned}
J(T) &= J_e^{eq}, \quad \text{if } t < t_v \\
J(T) &= J_e^{eq}[0.8 + 0.2 \exp(-(t - t_v)/10\tau_c)], \quad \text{if } t > t_v
\end{aligned} \tag{9}$$

where τ_c is the above-surface vapor collision time; t_v is the preheat time for preparing the vapor zone when recondensation become significant; J_e^{eq} is the equilibrium evaporation flux which can be estimated as:

$$J_e^{eq}(T) = 5.8 \times 10^{-2} \frac{\alpha \sqrt{AP_v(T_v)}}{\rho(T_v) \sqrt{T_v}} \tag{10}$$

where α is the sticking probability; A is the atomic mass; $P(T_v)$ is the saturated vapor pressure; $\rho(T_v)$ is the density at the surface; and T_v is the vapor temperature.

2.3 Radiation transport

Radiation transport theory was initially developed based on the classical problem of calculating star luminance, from which numerical methods and solution approximations of the radiation transport equation were developed [42]. Gas in the star body is optically very thick, and the space around the star is optically very thin. This enabled simple approximations of radiation transport equation (RTE): diffusion approximation, radiative heat conduction, forward/reverse, etc. [43].

Laboratory plasmas require special treatment in this regard. Such plasmas usually have high gradients of radiation energy density at small spatial lengths. Simple approximations are invalid as a rule for most practical applications. Advanced physical/mathematical models and numerical methods should be applied for correct interpretation of radiation energy distribution. Two main separate research approaches are being investigated, verified and compared in the frame of HEIGHTS simulation package for various plasma science applications: direct numerical solution

of RT equation using Gaussian quadrature method for volume integration along photons path and Monte Carlo models with several weighting factors to enhance accuracy and reduce the extensive computational time required for the simulation. These approaches provide significant insight on the appropriate numerical techniques for multidimensional solution of complex dense plasma physics applications.

2.3.1 Traditional models for radiation transport

Typical methods for the solution of radiation transport equations include:

- Radiation diffusion approximation method is based on the approximation for the relation between spectral radiation flux and spectral radiation energy density as:

$$S_\nu = -\frac{l_\nu c}{3} \nabla U_\nu \quad (11)$$

where l_ν is the length of photon path before absorption (corrected to take into account induced emission).

Radiation with low density gradient in the photon path is assumed in this approximation that is correct for the isotropic radiation field. The above equation can be transformed to the typical equation for the diffusion process with relation between the quanta flux and their density as:

$$J_\nu = -D_\nu \nabla N_\nu, \text{ where } D_\nu = \frac{l_\nu c}{3} \quad (12)$$

In the field, where radiation density has high gradient or at the borders of the domain with optically thin plasma, this approximation can lead to significant errors.

- Forward-reverse method considers two directions of radiation transport with the assumed isotropic distribution in each of the directions. This model can be described similar to diffusion approximation with the diffusion coefficient:

$$D_\nu = \frac{l_\nu c}{4} \quad (13)$$

- Radiative heat conduction model calculates radiation flux proportionally to the temperature gradient that is applicable in the environment with local thermodynamic equilibrium (LTE):

$$S = -\frac{16\sigma T^3}{3} \nabla T \quad (14)$$

The assumptions considered in the above methods make them inapplicable for laboratory plasma applications where the radiation density can have high gradient, quanta dispersion is anisotropic, and the accuracy of the uncertainty in the calculated plasma parameters can significantly influence the performance, validity, and the outcome of the anticipated application, e.g., radiation energy output for EUV lithography devices in the range of $13.5 \pm 1\%$ nm photons. Hence two advanced models were considered for the description of radiation transport for the application in different areas of laboratory plasma.

2.3.2 Direct numerical solution of RT equation using Gaussian method

The main goal of this method is to obtain the radiation flux and its divergence in each cell of the MHD domain mesh:

$$Q_{rad} = \nabla \cdot \vec{S}_{rad} \quad (15)$$

The radiation flux is integrated by a spectrum and by an angular variable. It depends on the distribution of plasma thermodynamic parameters (temperature and density) in the entire volume under consideration:

$$\vec{S} = \int_0^\infty \vec{S}_E dE \quad \vec{S}_E = \int_{4\pi} I_E \vec{\Omega} d\Omega \quad (16)$$

where I_E is the spectral radiation intensity and $\vec{\Omega}$ is a unit vector in the direction of quanta distribution. For the solid angle $d\Omega = \sin \theta d\theta d\varphi$, expression for the spectral flux is:

$$S_E = \int_0^{2\pi} d\varphi \int_0^{\pi} I_E(\varphi, \theta) \cos \theta \sin \theta d\theta \quad (17)$$

where φ and θ are the angles that determine the direction of the quanta distribution.

In the case of cylindrical symmetry, for example, the spectral flux at the point with coordinates r_0 and z_0 is described by the equation:

$$S_E = 2 \int_0^{\pi} d\varphi \int_0^{\pi} I_E(\varphi, \theta) \cos \theta \sin \theta d\theta \quad (18)$$

where the symmetry of the quanta distribution on the corner φ is taken into account. Here, φ is the angle between the projection of the quanta direction to the plane, perpendicular to the z -axis and normal to the cylindrical surface; and θ is the angle between the quanta direction and the z -axis (Fig. 9).

Simple projections of the radiation flux on the radial r - and axial z -axis give:

$$S_{RE}(r_0, z_0) = 2 \int_0^{\pi} d\varphi \int_0^{\pi} \cos \varphi \sin^2 \theta I_E(r_0, z_0, \varphi, \theta) d\theta$$

$$S_{ZE}(r_0, z_0) = 2 \int_0^{\pi} d\varphi \int_0^{\pi} \cos \theta \sin \theta I_E(r_0, z_0, \varphi, \theta) d\theta \quad (19)$$

The spectral radiation intensity $I_E(r_0, z_0, \varphi, \theta)$ is found from the solution of the radiation transport equation:

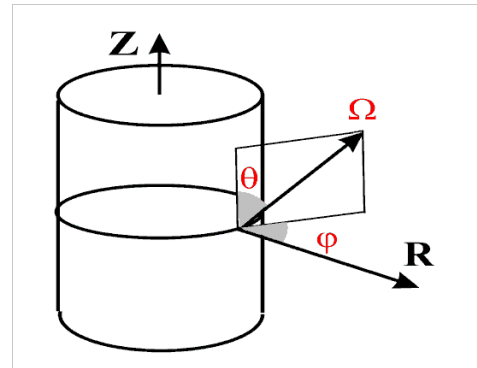


Fig. 9 Calculation of the quanta distribution in cylindrical geometry

$$\frac{dI_E}{ds} = \kappa_{Eemi} I_{Ep} - \kappa_{Eabs} I_E \quad (20)$$

Here, κ_{Eabs} is a spectral absorption coefficient for quanta with energy E , κ_{Eemi} is a spectral emission coefficient, I_E is the spectral intensity, and I_{Ep} is the spectral equilibrium intensity. The RTE represents the energy conservation law for the radiation intensity. The equilibrium intensity I_{Ep} is defined by the Planck function:

$$I_{Ep} = \frac{\hbar\omega^3}{4\pi^2 c^2} \cdot \frac{1}{e^{\frac{\hbar\omega}{\kappa T}} - 1} = \frac{\hbar^3 \omega^3}{4\pi^2 c^2 \hbar^2} \cdot \frac{1}{e^{\frac{\hbar\omega}{\kappa T}} - 1} = \frac{1}{4\pi^2 c^2 \hbar^2} \cdot E^3 (e^{\frac{E}{\kappa T}} - 1)^{-1}, \text{ or}$$

$$I_{Ep} = \frac{\kappa^3 T^3}{4\pi^2 c^2 \hbar^2} \cdot \frac{E^3}{\kappa^3 T^3} (e^{\frac{E}{\kappa T}} - 1)^{-1} = \frac{\kappa^3 T^3}{4\pi^2 c^2 \hbar^2} \cdot x^3 (e^x - 1)^{-1}, \text{ where } x = \frac{E}{\kappa T} \quad (21)$$

Equation (20) is a one-dimensional differential equation relative to the intensity along the ray of the quanta distribution. A formal solution of a Cauchy problem is given for this equation:

$$I_E(s) = I_E(s_0) \exp\left\{-\int_{s_0}^s \kappa_{Eabs}(s') ds'\right\} + \int_{s_0}^s I_{Ep}(s') \kappa_{Eemi}(s') \exp\left\{-\int_{s'}^s \kappa_{Eabs}(s'') ds''\right\} ds' \quad (22)$$

which expresses the fact that the intensity at any point in a given direction is the result of the emission at all anterior points s' , reduced by the factor $\exp\left\{-\int_{s_0}^s \kappa_{Eabs}(s') ds'\right\}$ as result of the absorption by intervening matter.

Equation (20) can be written as:

$$\frac{dI_E}{ds} = \kappa_{abs} \left(\frac{\kappa_{emi}}{\kappa_{abs}} I_{Ep} - I_E \right) \quad \text{or} \quad \frac{dI_E}{d\tau} = \frac{\kappa_{emi}}{\kappa_{abs}} I_{Ep} - I_E \quad (23)$$

where $d\tau = \kappa_{abs} ds$. This leads to:

$$I_E(\tau) = I_E(\tau_0) \exp\left\{-\int_{\tau_0}^{\tau} d\tau'\right\} + \int_{\tau_0}^{\tau} \frac{k_{emi}(\tau')}{k_{abs}(\tau')} I_{Ep}(\tau') \exp\left\{-\int_{\tau'}^{\tau} d\tau''\right\} d\tau' \quad (24)$$

The numerical approximation of Eq. (24) is obtained by the spatial discretization, assuming that the changing of temperature and density (and accordingly, the spectral coefficients) is insignificant within the one-cell boundaries. Then, the spectral intensity value on the observation ray is found by integration of values in the cells using:

$$I_E(\tau_i) = I_E(\tau_{i-1}) e^{-(\tau_i - \tau_{i-1})} + \frac{k_{emi}(\tau_i)}{k_{abs}(\tau_i)} \int_{\tau_{i-1}}^{\tau_i} I_{Ep}(\tau') \exp\left\{-\int_{\tau'}^{\tau_i} d\tau''\right\} d\tau' \quad (25)$$

Integrating yields

$$I_E(\tau_i) = I_E(\tau_{i-1}) e^{-(\tau_i - \tau_{i-1})} + \frac{k_{emi}(\tau_i)}{k_{abs}(\tau_i)} \left[I_{Ep}(\tau_i) - I_{Ep}(\tau_{i-1}) e^{-(\tau_i - \tau_{i-1})} - \int_{\tau_{i-1}}^{\tau_i} \exp\left\{-\int_{\tau'}^{\tau_i} d\tau''\right\} dI_{Ep}(\tau') \right] \quad (26)$$

and

$$I_E(\tau_i) = I_E(\tau_{i-1}) e^{-(\tau_i - \tau_{i-1})} + \frac{k_{emi}(\tau_i)}{k_{abs}(\tau_i)} \left[I_{Ep}(\tau_i) - I_{Ep}(\tau_{i-1}) e^{-(\tau_i - \tau_{i-1})} - \int_{\tau_{i-1}}^{\tau_i} \exp\left\{-\int_{\tau'}^{\tau_i} d\tau''\right\} (I_{Ep}(\tau'))' d\tau' \right] \quad (27)$$

In view of the chosen discretization, the Planck function derivative is a constant value in each cell. Thus,

$$I_E(\tau_i) = I_E(\tau_{i-1}) e^{-\Delta\tau_i} + \frac{k_{emi}(\tau_i)}{k_{abs}(\tau_i)} \left[I_{Ep}(\tau_i) - I_{Ep}(\tau_{i-1}) e^{-\Delta\tau_i} - \frac{I_{Ep}(\tau_i) - I_{Ep}(\tau_{i-1})}{\Delta\tau_i} (1 - e^{-\Delta\tau_i}) \right] \quad (28)$$

Here $\Delta\tau_i = \tau_i - \tau_{i-1} = \kappa_{abs}(s_i - s_{i-1})$ is the optical absorption thickness of the cell for quanta with energy E. Using Eq. (28), the spectral intensity along the radiation ray can be calculated. Next, all quanta of energies is integrated to find the total components of the radiation flux:

$$S_R(r_0, z_0) = 2 \int_0^{\pi} d\varphi \int_0^{\pi} \cos \varphi \sin^2 \theta \left[\int_0^{\infty} I_E(r_0, z_0, \varphi, \theta) dE \right] d\theta$$

$$S_Z(r_0, z_0) = 2 \int_0^\pi d\varphi \int_0^\pi \cos\theta \sin\theta \left[\int_0^\infty I_E(r_0, z_0, \varphi, \theta) dE \right] d\theta \quad (29)$$

Integration by Spectrum. The total radiation flux in the point is found by angular integration of the total intensity values from Eq. (29). The total intensity is the result of integrating by the energy quanta:

$$I = \int_0^\infty I_E(r_0, z_0, \varphi, \theta) dE \quad (30)$$

The energy spectrum grouping is used to obtain a numerical approximation of the last integral solution. Each group E_k is defined by the boundary values of energy quanta E_k и E_{k+1} and the mean group absorption and emission coefficients. Then, the total radiation intensity is found by summation of the intensity values, obtained for the spectral groups:

$$I = \sum_k \int_{E_k}^{E_{k+1}} I_E(r_0, z_0, \varphi, \theta) dE \quad (31)$$

Based on Eq. (21), the Planck function for each group is integrated by its boundary values as:

$$I_{E_k P} = \int_{E_k}^{E_{k+1}} \frac{\kappa^3 T^3}{4\pi^2 c^2 \hbar^2} \cdot \frac{x^3}{e^x - 1} dE = \frac{\kappa^4 T^4}{4\pi^2 c^2 \hbar^2} \int_{E_k}^{E_{k+1}} \frac{x^3}{e^x - 1} dx \quad (32)$$

Estimation of the quantum energy that can be ignored with a given error ($\sim 10^{-4}$) is carried out to reduce the calculation time before integrating the intensity along the ray. The following inequality can be used:

$$\int_{E_k}^\infty I_{E_p} dE < 10^{-4} \int_0^\infty I_{E_p} dE, \quad \text{or} \quad \int_{E_k}^\infty \frac{x^3 dx}{e^x - 1} < 10^{-4} \int_0^\infty \frac{x^3 dx}{e^x - 1} \quad (33)$$

The maximum value of temperature T_{\max} along the ray is found for that inequality. The

approximate integral value is calculated as $\int_0^\infty \frac{x^3 dx}{e^x - 1} = \frac{\pi^4}{15}$, from which it follows that

$$\frac{15}{\pi^4} \int_{x_k}^{\infty} \frac{x^3 dx}{e^x - 1} \approx \frac{15}{\pi^4} e^{-x_k} [x_k^3 + 3x_k^2 + 6x_k + 6] < 10^{-4}, \quad \text{where } x_k = \frac{E_k}{T_{\max}} \quad (34)$$

From this estimation, the energy groups with contribution less than 10^{-4} are not taken into account when the intensity integration along the ray is carried out. Tables of absorption and emission coefficients with the detailed resolution on the quanta energy, density, and temperature are used for the calculation of the spectral group intensity.

Integration by Rays. Each ray is divided into intervals with equal length Δl from the starting point of ray (r_0, z_0) to the exit from the hydrodynamic domain. It is assumed that the change in temperature and density (and accordingly, the spectral coefficients) is insignificant within the bounds of one cell. Then, the intensity on the observation ray is calculated from Eq. (28).

Integration by Angles. The total intensity is integrated by angles within the ranges $0 \leq \varphi \leq \pi$ and $0 \leq \theta \leq \pi$. Integrals over angles are approximated by the Gauss quadrature method:

$$A = \int_a^b f(x) dx = \frac{b-a}{2} \int_{-1}^1 f(\xi) d\xi = \frac{b-a}{2} \sum_i f(\xi_i) C_i \quad (35)$$

Here, C_i are weights of the Gauss quadrature, and $\xi_{i,j}$ are abscissas (changing from -1 up to 1).

The splitting is carried out at the nodal values φ_i and θ_j equal to $\varphi_i = \frac{\pi}{2}(1 + \xi_i)$ and

$\theta_j = \frac{\pi}{2}(1 + \xi_j)$. Then final equations for the calculation of flux components can be written as:

$$S_R(r_0, z_0) = \frac{\pi^2}{2} \sum_i C_i \sum_j \cos \varphi \sin^2 \theta I(r_0, z_0, \xi_i, \xi_j) C_j$$

$$S_Z(r_0, z_0) = \frac{\pi^2}{2} \sum_i C_i \sum_j \cos \theta \sin \theta I(r_0, z_0, \xi_i, \xi_j) C_j \quad (36)$$

Depending on the order of Gauss quadrature used, the integration can be carried out using 8, 12, 16, 20, 24, 32, 64, 80, or 96 points of an angular grid. Accordingly, the total flux value in

each point is calculated by integration of the intensity in the direction of 64, 144, 400, 576, 1024, 4096, 6400 or 9216 observation rays, going out from that point. The angular integration accuracy increases with increasing order of the Gauss. This method is, however, very time-consuming and resource intensive, that makes hard to provide an accurate study of any particular application. Understanding the importance and of the accuracy of the radiation transport calculation in reasonable time and to ensure the validity of our simulation, an alternative method of calculating the radiation transport by means of Monte Carlo model was developed.

2.3.3 Monte Carlo Radiation Transport

Alternative to the direct resolution of the RTE, where one searches the continuous function of the radiation intensity, the probabilistic model of the energy redistribution operates using the discrete portions of the radiative energies. Each energy portion is individually analyzed. Studying the trajectory and the behavior, as well as the number of emitted and absorbed energy portions in each point of the plasma domain (or in the points which represent major interest), one can then calculate the re-distribution of the energy due to photon transport. The energy and the trajectory of photon movement are played out by Monte Carlo technique. Each portion of the spectrum is assumed as a monochromatic set of photons. The total energy of a portion is a sum of the energies of the component photons, and the portion is called macro-photon, or photon bundle.

Depending upon the hydrodynamic parameters of a cell, some number of probe macro-photons is carried out by the Monte-Carlo radiation transport method (MCRT). The energies of the macro-photons are distributed according to the emission coefficient of the cell. Later on, the history, the behavior, and the track of the photons are statistically accumulated in the form of

energy redistribution within the domain. To improve the efficiency of the method, several innovative weight factors of the statistically collected events are utilized.

Emission of Photons. Monte Carlo methods have the advantage of being relatively straightforward to apply for complex geometries

(Fig. 10). HEIGHTS Monte Carlo model for radiation transport uses a numerical algorithm with weight factors to speed up calculations. Two major weight factors are developed: normalization of emitted photon "bundles" relative to the most radiated cell of the computational domain, and normalization of the photon bundle magnitudes relative to the optical thickness of cell. The first weight coefficient enables to detail the emission

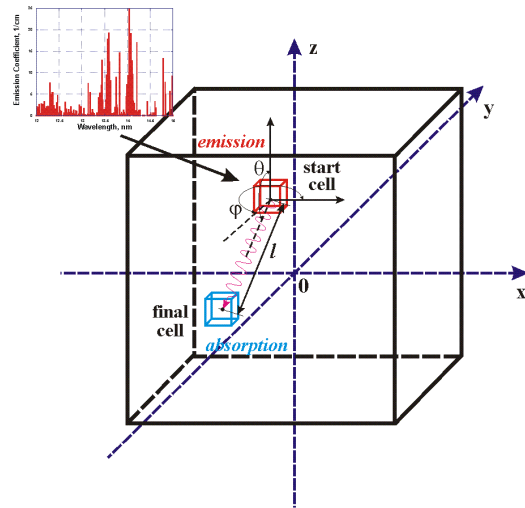


Fig. 10. Monte Carlo modeling of radiation transport in plasma [18]

process by neglecting cold cells emission, while in the second coefficient, "idle" processes are ignored, i.e., situations with photon emission and absorption within one cell (absorbed lines). These coefficients allowed significantly decreasing the computational burden. As preliminary calculations for a nonuniform mesh showed, a third weight coefficient can be useful. The volume of emitting cell can be so small that the amount needed to simulate photon bundles will not be sufficient for proper results. The volume weight coefficient increases computation accuracy in this case.

It is well known [43], that one needs to integrate the emission coefficient k_{emi} with Planck's function $B(\omega)$ in full spectrum to obtain the number N of photons emitted in space (from the volume unit in the time interval):

$$N = 4\pi \int_0^{\infty} \frac{k_{emi} B(\omega)}{\hbar \omega} d\omega, \quad B(\omega) = \frac{\hbar \omega^3}{4\pi^3 c^2} \left(e^{\frac{\hbar \omega}{T}} - 1 \right)^{-1} \quad (37)$$

After substitution and change of variables the following expression convenient for numerical calculations is obtained:

$$N = \int_{E_{min}}^{E_{max}} \frac{k_{emi}(E, T, \rho) E^2}{\hbar^3 \pi^2 c^2} \left(e^{\frac{E}{T}} - 1 \right)^{-1} dE \quad [\text{cm}^{-3} \text{s}^{-1}], \quad (38)$$

where E is the energy of emitted photon [eV]; E_{min}, E_{max} are the spectral range [eV]; $k_{emi}(E, T, \rho)$ is the emission coefficient [cm^{-1}]; T is the plasma temperature [eV]; ρ is the plasma density [g/cm^3]; $\hbar = 6.58217 \times 10^{-16}$ [eV·s] is the Planck's constant; $c = 2.9979 \times 10^{10}$ [cm/s] is the speed of light.

From the cell volume, temperature, and density values the total number of photons that are emitted in time unit is calculated as:

$$N_{i,j,k} = V_{i,j,k} \int_{E_{min}}^{E_{max}} \frac{k_{emi}(E, T_{i,j,k}, \rho_{i,j,k}) E^2}{\hbar^3 \pi^2 c^2} \left(e^{\frac{E}{T_{i,j,k}}} - 1 \right)^{-1} dE \quad (39)$$

where $V_{i,j,k}$ is the volume of cell (i,j,k) .

One of the most important points in Monte Carlo simulation algorithm is to search for the most radiative cell. The total number of photons in most radiative cell is then used for the normalization of photon bundles. This technique significantly increases the efficiency of calculations. From this point, the following algorithm was developed for Monte Carlo modeling of photons emission:

- The total number of emitted photons is calculated in the most radiative cell by integration range-by-range:

$$N^{\max} = \frac{V^{\max}}{\hbar^3 \pi^2 c^2} \sum_{k=1}^M k_{emi}(E_n, T^{\max}, \rho^{\max}) \int_{E_k}^{E_{k+1}} E^2 \left(e^{\frac{E}{T^{\max}}} - 1 \right)^{-1} dE \quad (40)$$

This expression assumes that the emission coefficient $k_{emi}(E_n, T^{\max}, \rho^{\max})$ is constant within one spectral range. M is the total number of ranges.

- The first weight coefficient W_1 is calculated.
- The spectral range distribution of emitted photons is obtained for the (i,j,k) cell:

$$N_{i,j,k}^n = \frac{V_{i,j,k} k_{emi}(E_n, T_{i,j,k}, \rho_{i,j,k})}{\hbar^3 \pi^2 c^2} \int_{E_k}^{E_{k+1}} E^2 \left(e^{\frac{E}{T_{i,j,k}}} - 1 \right)^{-1} dE \quad (41)$$

- The spectral range distribution of the second weight coefficient is determined for the (i,j,k) cell.
- Taking into account these weight factors, the total sum of Monte Carlo emission tests in the (i,j,k) cell is calculated:

$$N_{i,j,k}^{sim} = \frac{1}{W_1} \sum_{n=1}^M \frac{N_{i,j,k}^n}{W_{2\{i,j,k\}}^n} \quad (42)$$

Absorption of Photons. Attenuation of light intensity as a result of matter absorption is

described by the expression $I = I_0 e^{-\int_0^l k_{abs}(\omega, l) dl}$ [44] or, in photon number terms

$$N(\omega) = N_0(\omega) e^{-\int_0^l k_{abs}(\omega, l) dl} \quad (43)$$

Here $N_0(\omega)$ is the initial number of photons with frequency ω and l is the path length.

Considering the photon path within one cell (where the absorption coefficient is constant) the attenuation can be calculated as:

$$N(\omega) = N_0(\omega) e^{-k_{abs}(\omega)l} \quad (44)$$

The absorption/transition probability of the photon in cell (i,j,k) , following the expression (42), is given then as:

$$P_{i,j,k}^{abs}(\omega) = 1 - \frac{N(\omega)}{N_0(\omega)} = 1 - e^{-k_{abs\{i,j,k\}}(\omega)l}$$

$$P_{i,j,k}^{trans}(\omega) = e^{-k_{abs\{i,j,k\}}(\omega)l} \quad (45)$$

Emission and absorption/transition of all simulation results represent information about the energy redistribution in the computational domain due to radiation transport.

In analysis of radiation transport processes, two general aspects can be indicated. Radiation fluxes should be determined for (1) correction of the plasma thermal energy and, as a result, correction of the plasma motion in the MHD domain, and (2) investigation of the final, useful, e.g., for EUVL application, part of plasma radiation. Correct calculation of the energy spatial redistribution in the full spectrum plays a critical role in the solution of first problem. The total spectral range should be optimized to accurately describe the radiation energy redistribution using reasonable computational resources.

Plasma thermodynamic properties and optical coefficients are calculated using the self-consistent Hartree-Fock-Slater (HFS) model implemented in HEIGHTS [45]. The populations of atomic levels, ionization balance, and the ion and electron plasma concentrations are obtained based on the collisional-radiative equilibrium (CRE) approximation. Tabulated plasma properties and optical coefficients for wide range of temperatures and densities are used during the simulation of whole cycle of plasma evolution in LPP. Spatial attention was paid to the accuracy and details of plasma optical coefficients in the EUV range [46]. Based on HEIGHTS calculations the five ions starting from Sn^{+9} to Sn^{+13} contribute to the EUV emission near 13 nm

in Sn plasma, which is considered as the main source of radiation in this region. Detailed description of models for calculation of atomic data and plasma properties is given elsewhere [45].

To make the complex analysis of LPP devices and to take into account different aspects which can influence successful development of EUV source, energetic ions production in LPPs was calculated and benchmarked; and the response of optical multilayer mirrors to impact of kinetic ions was modeled for various energies. Our ITMC-DYN (Ion Transport in Materials and Compounds) dynamic Monte Carlo package was used to study surface damage of the MLM optical collection system due to the energetic ions produced during the laser interaction with tin targets. The package includes Monte Carlo models for ions interaction with target atoms as well as models for particles diffusion, surface segregation, molecular recombination, and desorption for gaseous species. The integrated models are time-dependent and self-consistent among all physical processes involved with continuous dynamic updating of target layers composition to accurately simulate realistic experimental conditions [47, 48].

2.4 Models testing and benchmarking

Plasmas in intense LPP sources have high gradients of radiation energy density at small spatial lengths and require special treatment. Therefore, accurate physical/mathematical models and appropriate numerical methods should be implemented and carefully benchmarked for correct calculation of plasma evolution, opacity, photons generation, and their transport and distribution. One of the most important processes in understanding plasma evolution and EUV source generation and location is photon transport in such complex plasma environment. Two separate methods for calculating radiation transport have implemented and compared, i.e., direct

integration of the radiation transport equation along photon path and Monte Carlo models with several novel weight factors to enhance the accuracy and the speed of calculations. These two independent methods agree well with each other and highlight the importance of accurate full 3D solution of radiation transport equations for the correct simulation of LPP sources. Detailed description of laser energy absorption and dynamics of target vaporization are also quite important for various laser/plasma interaction regimes in EUVL devices. Hydrodynamic effects during plasma evolution and containment can significantly influence EUV emission, which usually follows laser intensity profile in ideal LPP conditions.

The models implemented in HEIGHTS are extensively tested and benchmarked separately in each physics phase of laser/target interaction as well as in the entire integrated system without any parameters adjustments or fitting routines. Final benchmarking was done for a completely EUV lithography application. The EUV output was calculated from the LPP device with planar geometry of the tin target and compared to published data [16]. The arrangement of the experiment is shown schematically in Fig. 11.

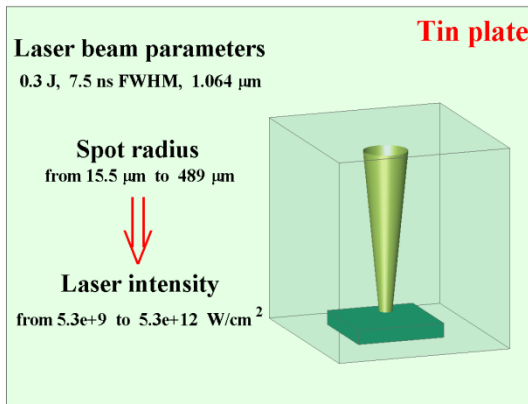


Fig. 11. Experimental parameters used in modeling for benchmarking

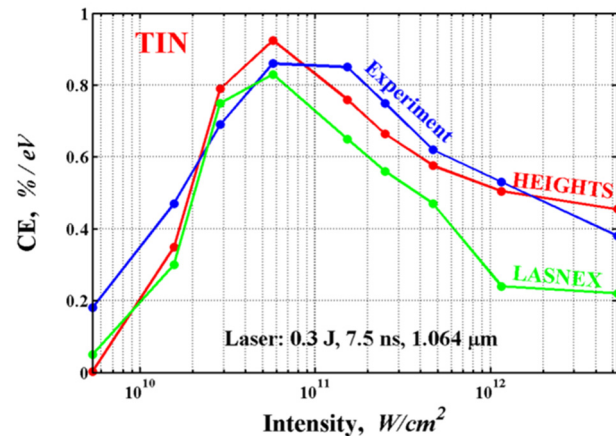


Fig. 12. Efficiency of LPP devices using tin planar target. Comparison of experimental and theoretical data [16, 49]

The device used in the assembly and modeled with the HEIGHTS package is using an Nd:YAG laser, delivering 0.3J at 1.064 μm in a 7.5 ns pulse. Laser light was focused onto the target surface at normal incidence by an aberration- and chromatic corrected lens with a 20.3 cm focal length. The laser radiation intensity is controlled by tuning the laser spot radius. The minimum spot size at the target was about 20 μm .

The physical and mathematical model assembled for this problem included all the blocks of HEIGHTS package: Eulerian/Lagrangian description of plasma hydrodynamic evolution in multidimensional finite volume approximation, implicit sparse matrix solution for parabolic terms, Monte Carlo radiation transport, Monte Carlo laser absorption, and Monte Carlo modeling of EUV output registration. The model was tested with two and three dimension numerical schemes, with equal results. Also several variants of spatial meshes were tested: for 2D 100 \times 250 cells with minimal size of cell in region of interest $\sim 1\mu\text{m}$ and 65 \times 110 with size $\sim 5\mu\text{m}$; for 3D 40 \times 40 \times 45 cells with cell size $\sim 10\mu\text{m}$ for large spot sizes only. A final parameter that served as a criterion for the code work evaluation was the total EUV output into 2π sr solid angle, that is, the CE of the LPP device:

$$c_{EUV} = \frac{Q_{EUV}^{13.4nm \pm 1.1eV}}{Q_{las} \cdot 2.2eV} \cdot 100\%, \quad (46)$$

where $Q_{EUV}^{13.4nm \pm 1.1eV}$ is the amount of EUV radiation energy registered in the 2.2 eV bandwidth centered at 134 \AA . The efficiency is normalized to 1 eV. Figure 12 shows a comparison of experimental results, well-known theoretical data (LASNEX), and results simulated by the HEIGHTS package.

HEIGHTS models were benchmarked considering several parameters and conditions, which can influence the in-band photons production, i.e., laser beam wavelength, spot size and target geometry.

Figure 13 compares the results of HEIGHTS modeling with the experimental results, where tin droplets with 100 μm diameters were irradiated by a CO₂ laser beam with 100 μm spot size and with different intensities [50]. HEIGHTS showed very good agreement with the data over a wide range of laser intensities. HEIGHTS results showed also that the CE exhibits similar peaking behavior to the experimental data with the laser intensity and laser wavelength, with maximum CE predicted at relatively lower intensity for the longer wavelength.

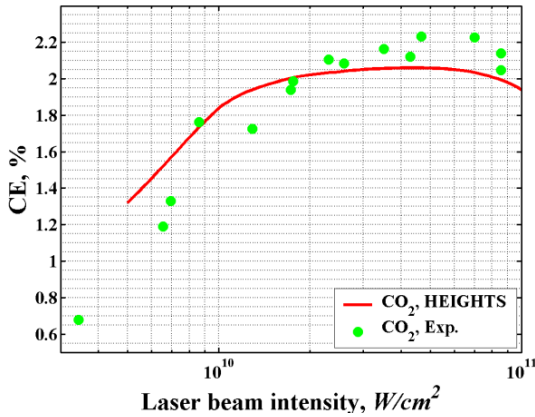


Fig. 13. Dependence of CE on CO₂ laser beam intensity in experiments [50] and HEIGHTS modeling [18]

The HEIGHTS integrated modeling was also compared with the experimental data obtained in our CMUXE laboratory. Nd:YAG laser with 1064 nm wavelength and with 8 ns duration and 150 μm spot size on planar target was used in both the experiment and for the HEIGHTS simulation. The dependence of the CE on laser beam intensity is shown in Fig.14 and demonstrates a good agreement with the models in both the magnitudes and the trends.

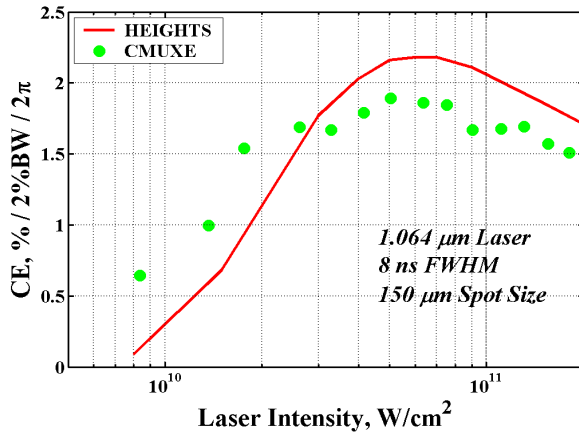


Fig. 14. Dependence of CE on Nd:YAG laser intensity both experimentally (CMUXE laboratory) and simulation (HEIGHTS package) [51]

As shown above, the HEIGHTS numerical results agree well with the published data. The numerical scheme demonstrated stability of results with changing spatial discretization and with expanding to the full 3D system. These results indicate that the HEIGHTS package can be used effectively to study complex optimization problems in LPP devices for efficient EUV photons output and collection.

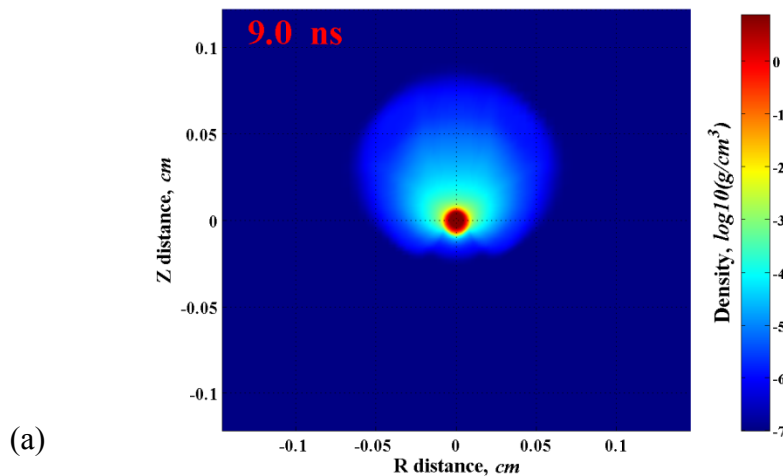
3. MODELING, ANALYSIS, AND OPTIMIZATION OF EUVL SOURCES

Advanced computer simulation of LPP can be important tool for designing and optimizing LPP devices and can significantly reduce the cost and the time of conducting extensive experiments. However, accurate simulation of LPP devices for EUVL requires advanced multidimensional physical models and numerical methods. The influence and the importance of various processes implemented in the HEIGHTS package, on plasma evolution dynamics and as result on the EUV source intensity, location, and size were studied.

3.1 Effect of laser parameters and geometrical containment on EUV photons output

3.1.1 Laser wavelength influence

To analyze the effect of laser wavelength on EUV source from Sn target, the interaction of a single laser beam with a droplet target was simulated [52]. The spherical tin target had a 100 μm diameter and was located at the point of origin of a cylindrical coordinate system. The laser beam coincided with the z-axis. Three laser wavelengths were tested for 10 ns pulse duration: 355, 532, and 1064 nm. Typical density, temperature, and velocity of plasma are plotted in Fig. 15. Distributions are shown for the case $\lambda = 1064$ nm, $E_{\text{pulse}} = 45$ mJ, time moment 9 ns after the laser pulse starts.



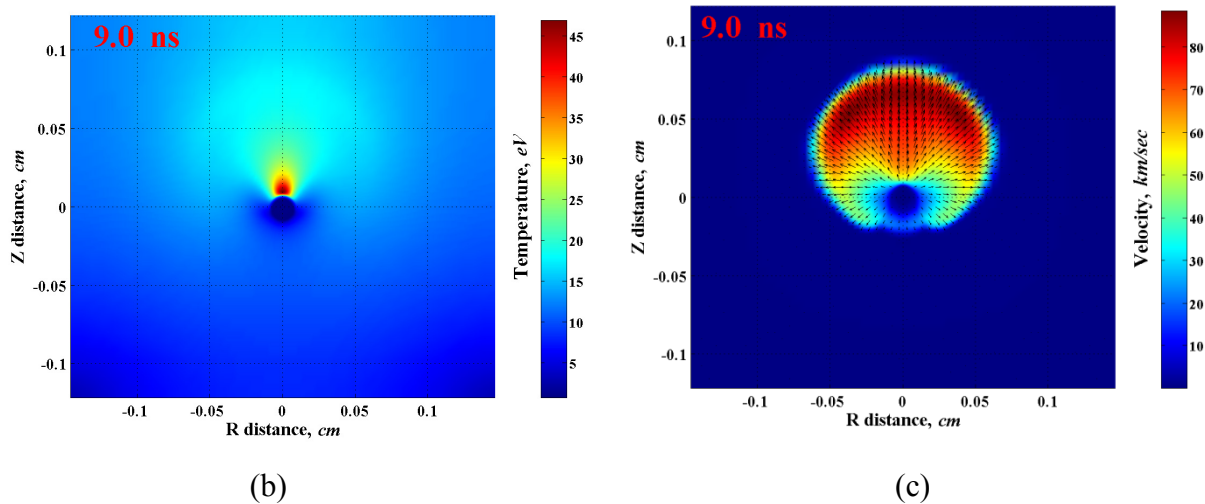


Fig. 15. (a) density, (b) temperature, and (c) velocity of tin plasma distributions at 9.0 ns. Single laser case: energy of laser pulse 45 mJ, wavelength 1064 nm.

The efficiency of the simulated EUV device is shown in Fig. 16 as a function of laser power density. The CE was calculated as the ratio of total EUV output (13.5±1% nm) into 2π sr solid angle to the energy of the initial laser pulse. Experimental data showed HEIGHTS similar behavior on wavelength intensities of Nd:YAG lasers [53]. As shown in Fig. 16, the maximum of the efficiency is obtained around 5×10^{10} W/cm² with a laser wavelength of 1064 nm. The optimum laser irradiance corresponds to total laser energy of 30–50 mJ irradiated in 10 ns as predicted by HEIGHTS simulations.

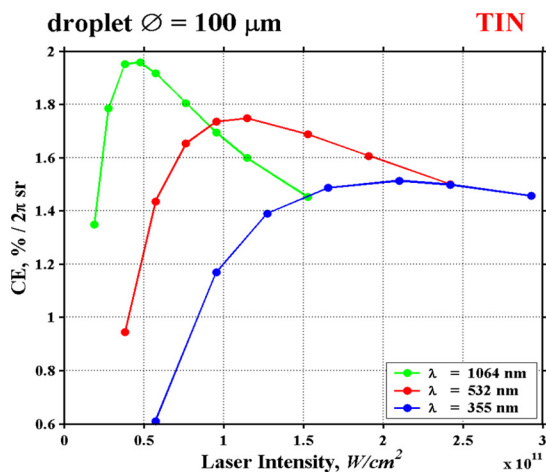


Fig. 16. Efficiency of the LPP device as a function of laser beam intensity for three laser wavelengths [52]

3.1.2 Target geometry influence on plasma evolution

For studying the spatial hydrodynamic effects of spherical and planar targets on the EUV production, Nd:YAG laser interaction with both a tin droplet and a slab target was modeled [51]. Similar laser parameters were used in both cases, i.e., 1.064 μm laser wavelength with 70 μm spot size and 8 ns (full width, half maximum) duration. The diameter of the droplet was chosen to be two times larger than the spot size to allow efficient utilization of the laser energy and the target can still be considered as spherical.

One of the main goals of this thesis is to determine the role of the hydrodynamic evolution and containment processes as the main cause for the differences in the CE between the planar and spherical targets. HEIGHTS showed that planar targets provide greater geometrical plasma containment in comparison to the spherical case. This hydrodynamic containment prevents the plasma to quickly escape from the EUV production zone.

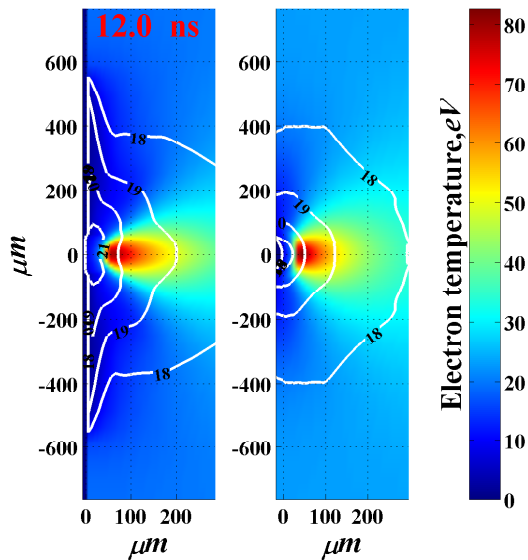


Fig. 17. Electron temperature and density (white contours) distribution in planar (left) and droplet (right) target models [51]

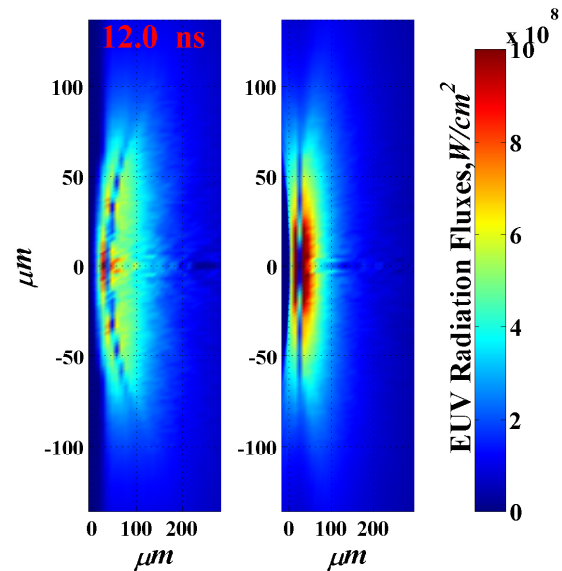


Fig. 18. Radiation fluxes in EUV range in planar (left) and droplet (right) target models [51]

Figure 17 shows the electrons temperature and density distributions at 4 ns after the peak of the laser beam with an intensity of 5×10^{11} W/cm² (FWHM) irradiated the target surface. The target surface is located in all cases near the zero point. The plasma near target surface with electron density of around 10^{20} cm⁻³ and electron temperature of ~ 30 eV forms most productive EUV radiation area for these conditions. As shown in Fig. 18, significant part of the emitted photons is absorbed around this area in the denser zone (close to target surface) or in the more hot areas. The EUV radiation fluxes have larger values in surrounding regions.

HEIGHTS Monte Carlo model for radiation transport simulation allows determining the location and intensity of photons source for EUV output in 2π sr (Fig. 19). The shape of EUV source area corresponds to the shape of the optimum plasma plume for photon production and depends on the area of the absorbing plasma. Figure 19 illustrates the source of EUV photons collected during 20 ns with laser pulse width 8 ns (FWHM).

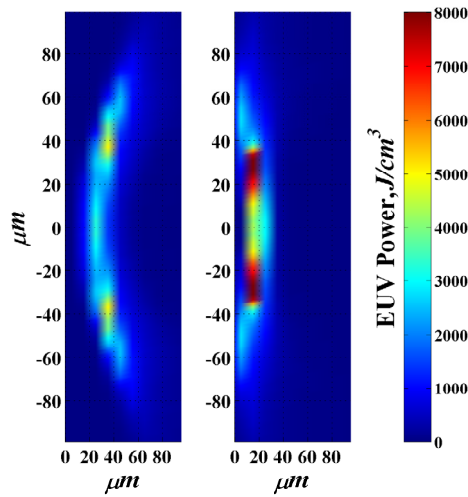


Fig. 19. Location and intensity of EUV power collected during 20 ns in 2π sr in planar (left) and droplet (right) target models [51]

Figures 17-19 correspond to an intense laser heating of $5 \times 10^{11} \text{ W/cm}^2$. This analysis shows that the effective plasma containment in the case of high laser energy input causes plasma overheating and therefore, decreases the CE. Figure 20 confirms this observation. Planar target is more effective than droplet target for small and medium laser radiation intensities. The overheating reverses this situation for laser intensities higher than $\sim 2.5 \times 10^{11} \text{ W/cm}^2$.

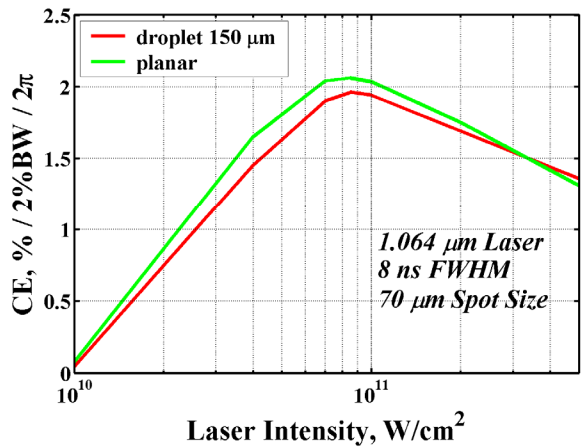


Fig. 20. Dependence of CE on laser intensity for sphere and planar targets [51]

At lower laser intensities the plasma is not excessively overheated and the size of EUV area is larger for the planar geometry because of better plasma evolution and containment. The EUV radiation area produced by laser heating of intensity $7 \times 10^{10} \text{ W/cm}^2$ is shown in Fig. 21. Most significant EUV photons generation zone is located around the spot center, in contrast to previously described regime.

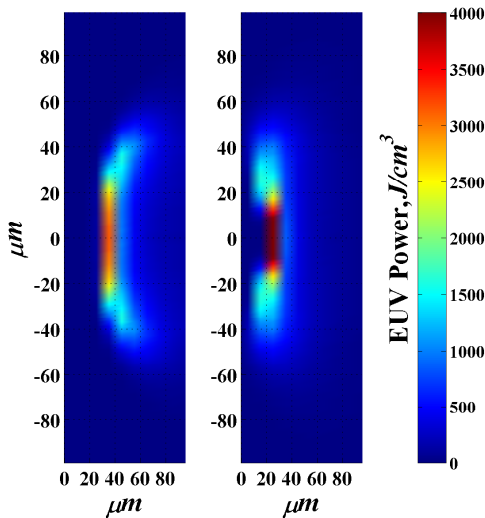


Fig. 21. Location and intensity of EUV power collected during 20 ns in 2π sr in planar (left) and droplet (right) target models [51]

At higher laser intensities hydrodynamic plasma evolution moving away from the area of laser energy deposition/absorption prevents further plasma overheating in the system with the spherical configuration (Fig. 19). Hence, the difference in CE for planar and spherical target is explained by the nature of hydrodynamic geometrical containment. Condition with high plasma density and stable temperature should be created to get an optimum CE. The plasma temperature stability is provided by the balance between the incoming and escaping energy, i.e., laser energy absorption, radiation energy loss, and plasma expansion. The last term is mainly controlled by hydrodynamic containment.

The geometrical hydrodynamic effects control the plasma motion, i.e., limit and control the escaping plasma from the laser heating area and from the most productive EUV generation zone. In the case of the larger laser heating region, lower laser intensities are needed to create the efficient EUV production area because of the longer time of the plasma motion under the laser beam. The smaller laser irradiation spots produce opposite effects. As a result, the hydrodynamic containment believed to be the cause of the right shift of the maximum CE due to the decrease of the laser beam radius (see Fig. 22). This is a consequence of the hydrodynamic evolution where the plasma containment can play an important role. In order to maximize EUV production, one has to create the proper plasma density and temperature conditions with maximum size for the longest possible period of time.

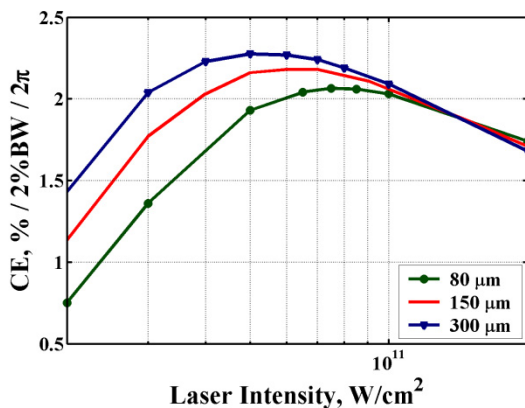


Fig. 22. Laser intensity and spot size dependence of CE [51]

The difference in combination of plasma density and temperature in most EUV emissive areas and in surrounding plasma determines photon source efficiency. Distribution of these parameters depends among other factors on hydrodynamic expansion and containment, which can be controlled by lasers [52, 49], target geometry [54], or a combination of both.

3.1.3 Plasma production and containment by multiple laser beams

To achieve efficient conditions for EUV photons output, the space- distributed laser beam assembly shown in Fig. 23 was constructed. The three laser beams can effectively confine the plasma density by any optimal axial angle θ . The proposed laser beam configuration should organize along the z-axis the plasma jet confined in the radial direction. The case $\theta = 0$ corresponds to a single-laser device construction. The 3D problem was simulated for a tin droplet with diameter 100 nm. Energy of pulse (45 mJ) was distributed in equal parts between three lasers started at one time. The duration of the pulse was 10 ns. The laser wavelength was 1064 nm. Initial conditions of this numerical experiment correspond to the most optimal single-laser case shown in Fig. 16. The square distribution of laser energy in time and the Gaussian distribution in space were used in this numerical experiment.

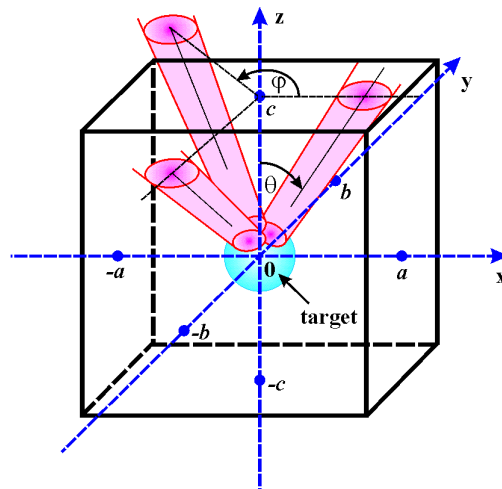


Fig. 23. Three-beam LPP device, ϕ - radial angle, and θ - axial angle [52]

Influence of the plasma containment on the efficiency of LPP device is plotted in Fig. 24 as the dependence on the axial angle θ .

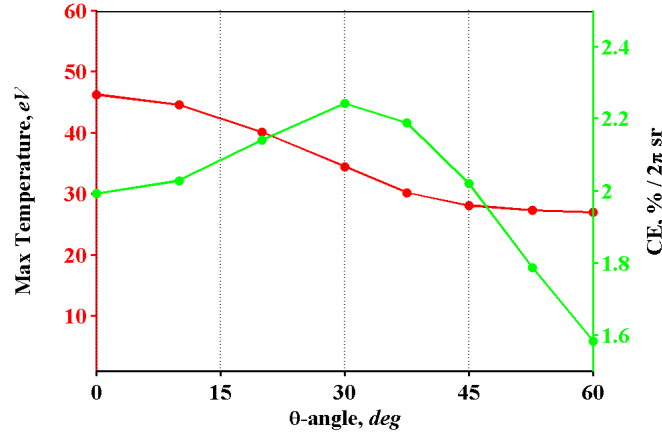


Fig. 24. Efficiency of the three-beam LPP device as a function of axial angle (green line). Maximum temperature of plasma (red line) [52]

The second numerical experiment confirms the existence of the optimal axial angle ($\theta \sim 30^\circ$), where plasma containment gives an advantage in the EUV output CE (Fig. 25).

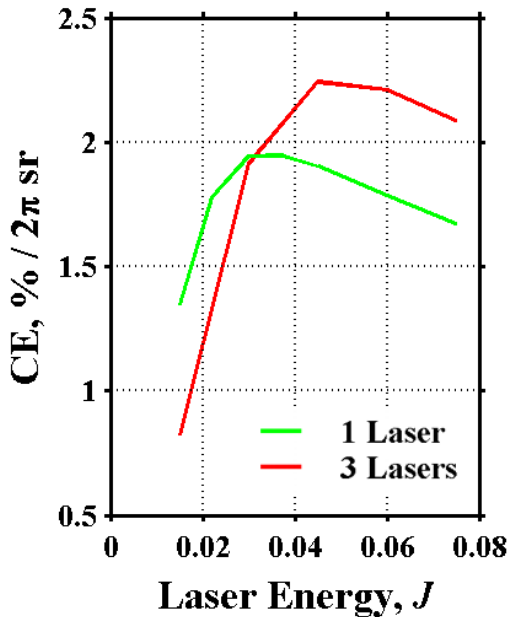


Fig. 25. Efficiency of the three-beam LPP device as a function of the total pulses energy for the axial angle $\theta = 30^\circ$ [52]

As it was assumed, a new plasma jet appears and obtains energy in area between the laser beams. The efficiency of the three-beam device should be higher in comparison to the single-

beam device only with enough laser pulse energy: optimal plasma temperature and density cannot be achieved in the central jet with initially cold plasma. EUV efficiency dependence on the laser pulse energy is plotted (Fig. 25) for the optimal axial angle $\theta = 30^\circ$ and confirmation of this statement was obtained.

Figure 26 shows temperature fields in x-y-plane cross-sections that correspond to the maximum temperature points (see Fig. 24).

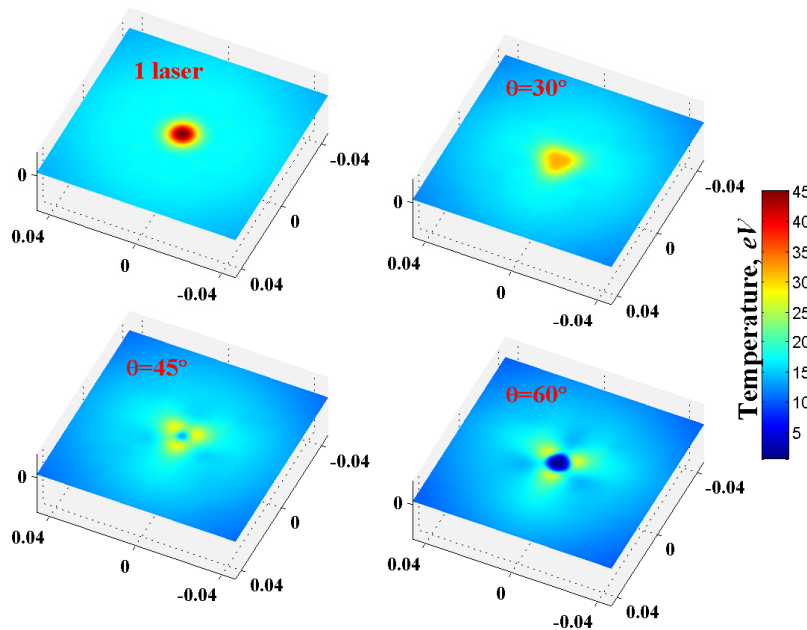


Fig. 26. Temperature fields for (x-y) cross-section in point of maximum temperature at 9 ns. One-laser case corresponds $\theta = 0^\circ$

The plasma motion initiated with three laser beams is illustrated in Fig. 27. Here are presented (z-x) cross-sections of density, temperature, and velocity fields. The black arrow indicates the direction of the formed plasma jet.

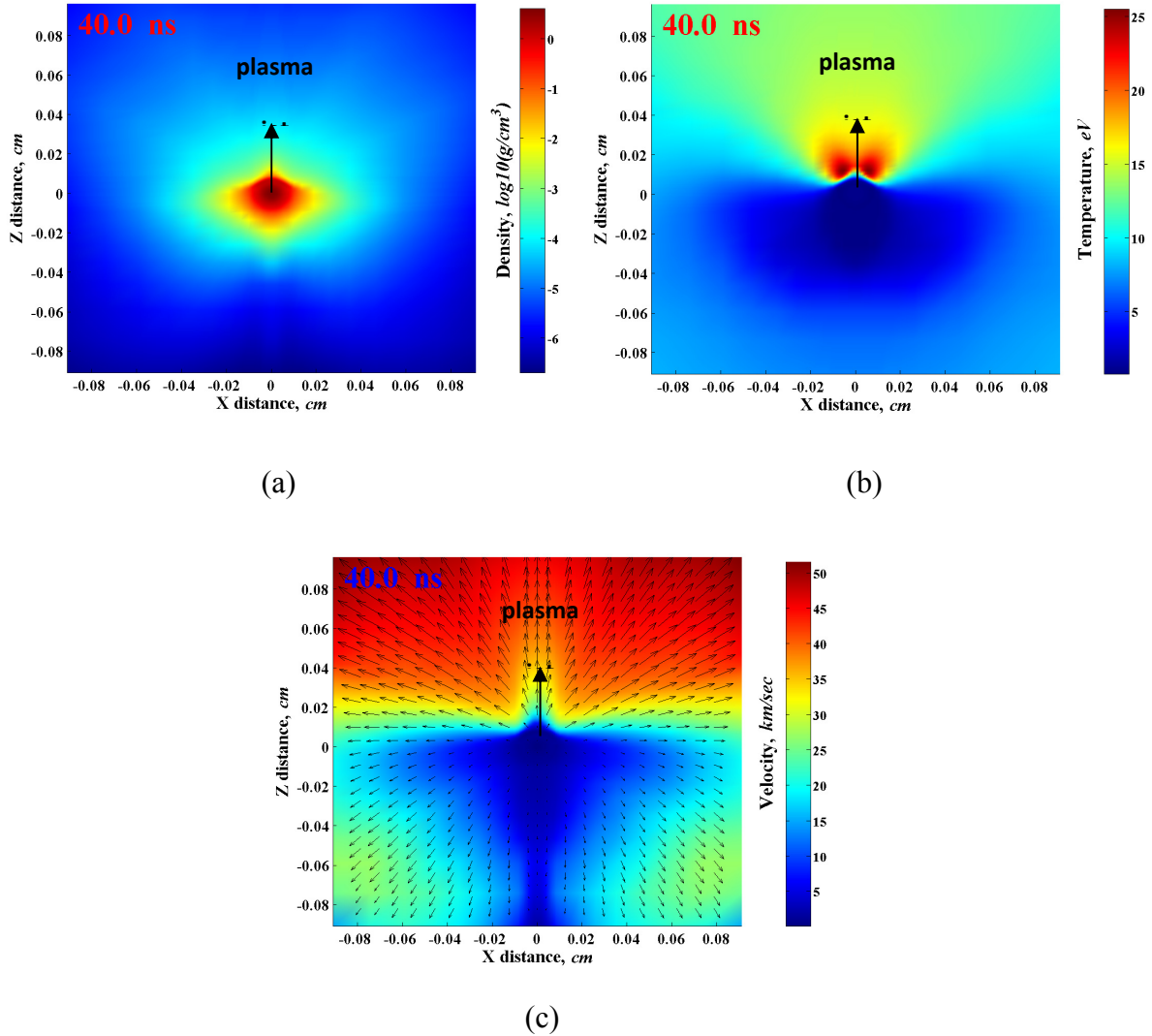


Fig. 27. (a) density, (b) temperature, and (c) velocity of tin plasma distributions at 40 ns in z-x plane [52]

Hydrodynamic plasma evolution requires accurate description and precise modeling especially in the simulation of smaller laser spots and targets. The desire for the smallest possible target is based on the requirement for longer chamber components lifetime mainly the mirrors collecting system [55]. Mass-limited targets such as small droplets allow reducing debris fluence to the optical system preventing contamination and surface damage. However, small size of target leads to reducing laser spot size and, as consequence, a significant decrease in CE of laser energy to EUV useful photons [16].

3.1.4 Comparative analysis of plasmas created by CO₂ and Nd:YAG lasers

Currently two laser sources are considered for EUV plasma source production using pre-pulse technique, viz. Nd:YAG (1.06 μm) or CO₂ (10.6 μm). The wavelength effects of the laser light on the temporal and spatial features of EUV radiation emission were studied and approximately the same CE from plasmas created from a tin foil by CO₂ and Nd:YAG lasers was obtained with optimized parameters for both lasers. The situation differs when small droplets are used as the target for plasma creation. Efficiency of such systems for EUV radiation is significantly lower than efficiency of devices using planar targets. While such decrease is less pronounced in the case of Nd:YAG laser, the CE of the CO₂ laser decreases by several times in comparison to planar targets where larger laser spots can be used.

The efficient release of 13.5 nm radiation by the plasma is related to plasma opacity, which depends on the level populations of different ionic states, ionization balance, and electron density. The density of plasma is governed both by laser and target properties. For nanosecond (ns) LPP, the leading edge of the laser pulse creates plasma, and the remaining part of the laser pulse heats the plasma instead of interacting with the target.

The influence of the deposition time of the laser energy on the total EUV output in 2π -solid angle with time was analyzed [56]. Typically CO₂ laser beam has a long pulse length and complicated spiky shape while the Nd:YAG laser in general possesses Gaussian temporal profile.

The intensity profiles in Figures 28 and 29 demonstrate the strong dependence of the EUV emission on the temporal profiles of CO₂ and Nd:YAG laser pulses. In the case of 1.06 μm laser the EUV radiation output is quite longer than incident laser pulse width. This can be explained by the chosen laser parameters in the modeling with a larger spot size (500 μm) and 10 ns

(FWHM) deposition time. This laser beam parameters produced relatively hot dense plasma that led to more time for cooling of such plasma.

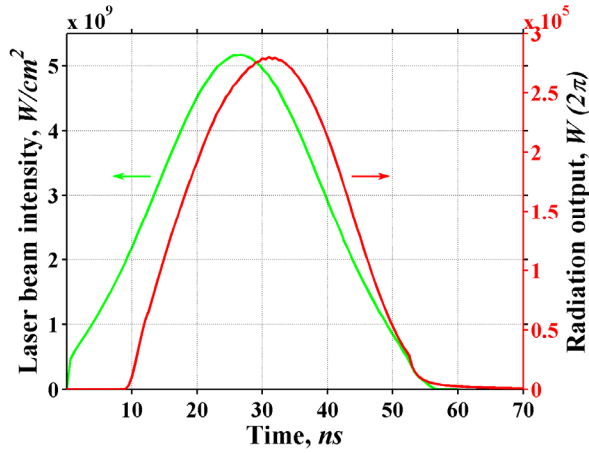


Fig. 28. Time profile of laser beam intensity and EUV radiation output for 10.6 μm laser wavelength [56]

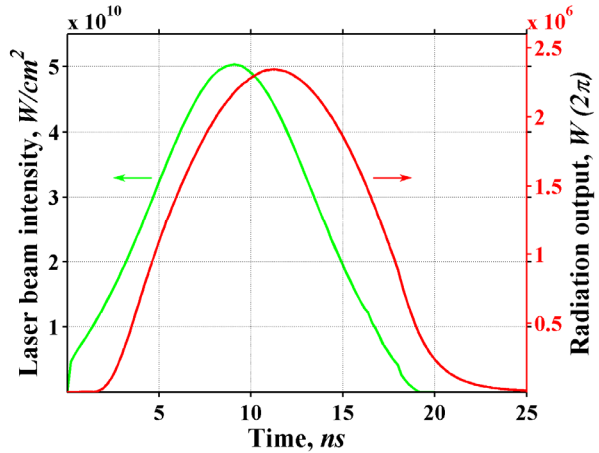


Fig. 29. Time profile of laser beam intensity and EUV radiation output for 1.06 μm laser wavelength [56]

A special case with pulse profile typical for CO₂ lasers found in CMUXE experiments and then implemented in our HEIGHTS modeling is shown in Figure 30.

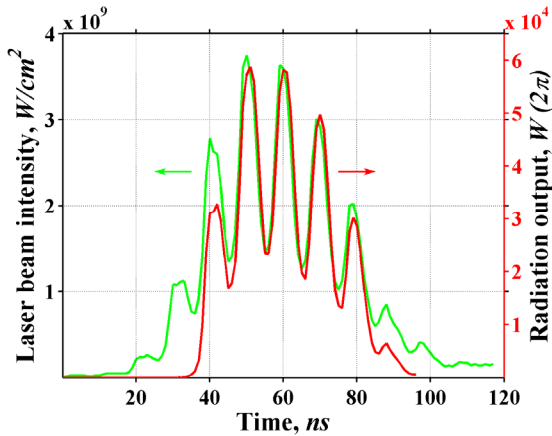


Fig. 30. Experimental time profile of laser beam intensity and modeled EUV radiation output for 10.6 μm laser wavelength [56]

The complex temporal pulse shape of this laser significantly influences the time dependence of the EUV radiation output. The time dependence of the plasma temperature follows similar behavior with maximum values varied from 45 eV at 50 ns to 30 eV at 55 ns which influences

the EUV radiation output. Figure also illustrates that an initial part of CO₂ typical pulse is inefficient for the EUV production.

The dependence of the source location and intensity on plasma conditions created by Nd:YAG and CO₂ lasers was analyzed [57]. Figures 31 and 32 show that optimum temperature for EUV emission is around 30-40 eV in plasmas created by both lasers.

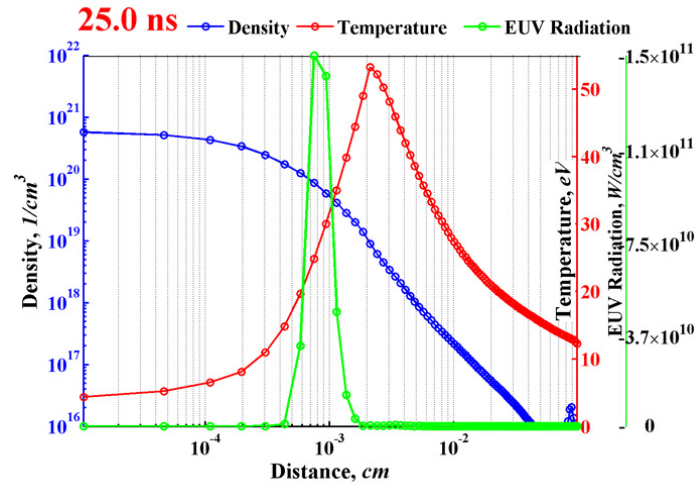


Fig. 31. EUV source location and intensity in relation with density and temperature of plasma created by CO₂ laser [57]

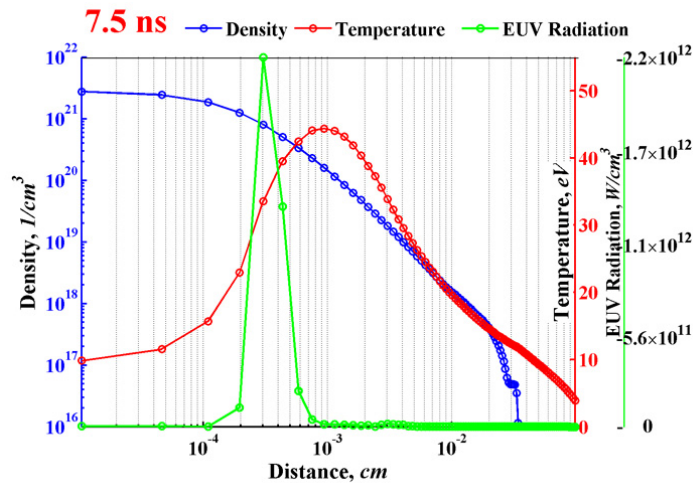


Fig. 32. EUV source location and intensity in relation with density and temperature of plasma created by Nd:YAG laser [57]

Since 10 μm wavelength radiation is absorbed in region with plasma density of 10^{19} cm^{-3} , location of maximum EUV output is determined by this density value. Laser with 1064 nm wavelength is absorbed by plasma with the density $10^{20} - 10^{21} \text{ cm}^{-3}$ near the target surface, that also determines the location of EUV source. In these simulations, the optimized intensities for lasers with considered spot size (30 μm) were used, such as $5 \times 10^{10} \text{ W/cm}^2$ with 30 ns (FWHM) duration for CO_2 and 10^{11} W/cm^2 with 10 ns (FWHM) duration for Nd:YAG. The presented results correspond to the peak intensities of these lasers.

Figures 31 and 32 show also that the intensity of EUV source in denser plasma (created by Nd:YAG) is one order of magnitude higher. It is explained by the optical properties of tin plasma with high EUV emissivity at specific temperature values (30-40 eV), where EUV emission (and correspondingly absorption) is increased significantly with density increase, however emission (and absorption also) is decreased abruptly at higher temperature values, located above EUV source.

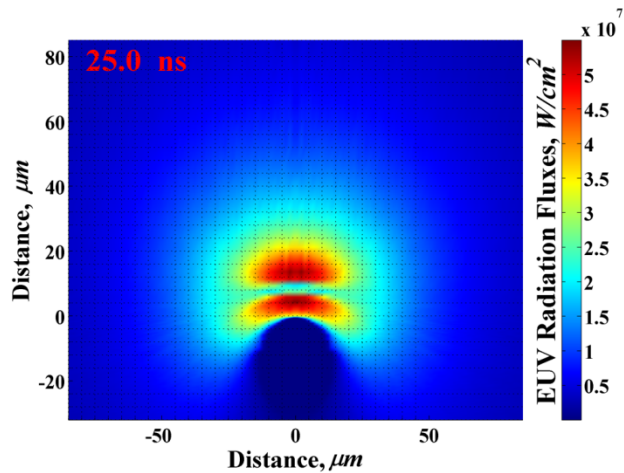


Fig. 33. EUV radiation fluxes in plasma created by CO_2 laser [57]

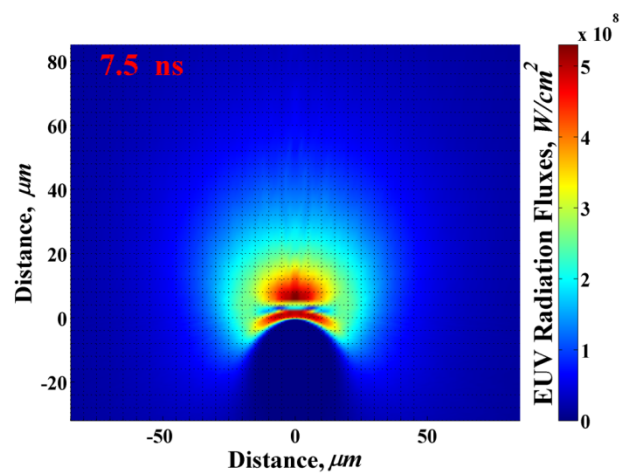


Fig. 34. EUV radiation fluxes in plasma created by Nd:YAG laser [57]

Figures 33 and 34 illustrate EUV energy distribution for the above cases, that is, EUV radiation fluxes (W/cm^2) that describe energy redistribution from the source, i.e., most intensive

EUV emission area. EUV source (W/cm^3) in Figs. 31 and 32 corresponds to the area between peaks in figures (for fluxes).

As shown in Figs. 33 and 34, significant part of the emitted photons is absorbed around the source, i.e., in the denser zone closer to the target surface or in the hotter areas above. The EUV radiation fluxes have larger values in surrounding regions. Radiation fluxes in plasma created by Nd:YAG laser are one order of magnitude larger; resulting EUV radiation power, reached the walls of the modeled chamber or the collecting location, is several times higher. In these cases modeling was done for 30 μm Sn droplet. The CEs of 1.3% for Nd:YAG laser and 0.45% for CO_2 were obtained.

3.1.5 Low efficiency of EUV sources from small droplets

The decrease in CE for Nd:YAG laser in systems with small spherical targets is not so significant (see Fig. 22) and explained mainly by the necessity to use reasonable small spot size in correspondence with droplet diameter. The decrease of CO_2 laser efficiency is, however, also influenced by lower vaporization rate that results in small plasma/vapor plume developed by this laser from the small droplet.

One of the main important processes during target/plasma evolution in LPP systems is the rate of laser energy absorption and reflection during the course of laser pulse deposition. Figure 35 illustrates the difference in the absorption of CO_2 laser (10.6 μm wavelength) during the development of plasma plumes created from a planar target and from a droplet with the same laser beam parameters, i.e., in this case 30 μm spot, $5 \times 10^{10} \text{ W}/\text{cm}^2$ intensity and laser pulse width 30ns (FWHM). Less energy is absorbed in droplet target configurations due to the plasma geometrical evolution and motion around the droplet.

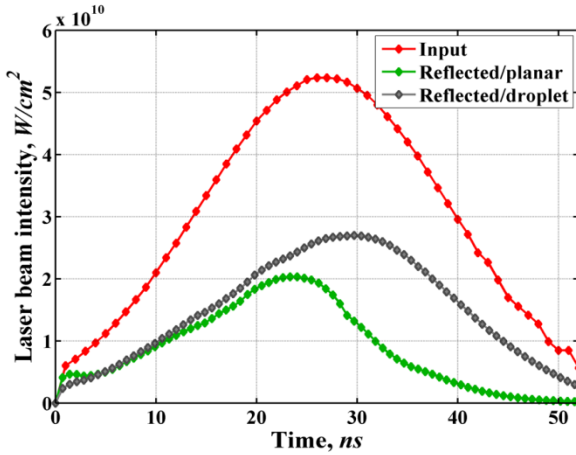


Fig. 35. Incident and reflected laser energy in plasmas created from tin planar and droplet targets with 30 μm spot size [58]

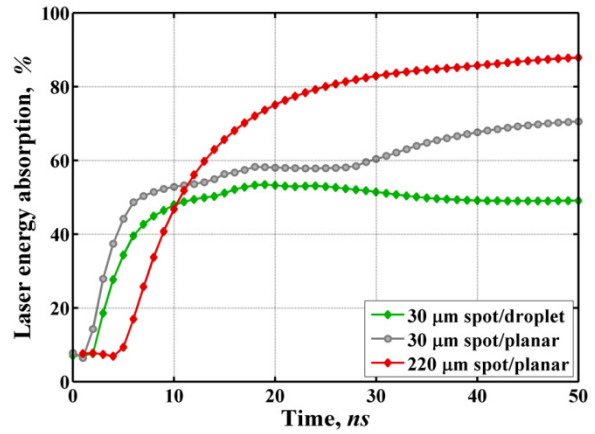


Fig. 36. Comparison of absorbed laser energy in plasmas created from tin planar and droplet targets using laser with small spot size and from planar with large laser spot size [58]

In these simulations as well as in experiments [59], the CE of source from 30 μm droplet heated by CO_2 laser is very low, around 0.5%. The CE for planar target with the same laser beam parameters is 1%. Figure 36 shows the difference in the absorbed energy for these conditions and also, in comparison with the energy absorption of laser beam with larger spot size, which gives higher CE of EUV of about 2.15% in HEIGHTS simulations compared well to 2.3% in recent experiments of similar conditions [60]. The processes of intense absorption of laser photons in plasma were delayed in the case of larger laser spot (Fig. 36) due to almost 10 times lower laser intensity. The lower intensity delayed the process of vapor/plasma plume formation, suitable for CO_2 laser photons absorption. The intensities of $5 \times 10^{10} \text{ W/cm}^2$ and $6.5 \times 10^9 \text{ W/cm}^2$ were used for the small and large spot sizes, respectively, since these produce most efficient plasma for EUV source with approximately the same range of plasma temperatures, i.e., up to 55eV.

With similar initial reflection rate in both planar and spherical target cases, during laser beam heating solid targets, the subsequent absorption in the developed plasma plume is almost two times less in the case of spherical target. Spatial distribution of the absorbed laser energy at this

time (Figs. 37 and 38) shows that planar target provides larger area in the direction of laser beam suitable for CO₂ photons absorption. One of the main reasons for this behavior is higher, more than five times, vaporization rate from the planar target due to plasma and geometrical effects. The differences in vaporization process and hydrodynamic evolution of plasma plumes from planar and spherical targets determined the difference in location and shape of area for the laser photons absorption and, as consequence, the location and intensity of EUV emission area.

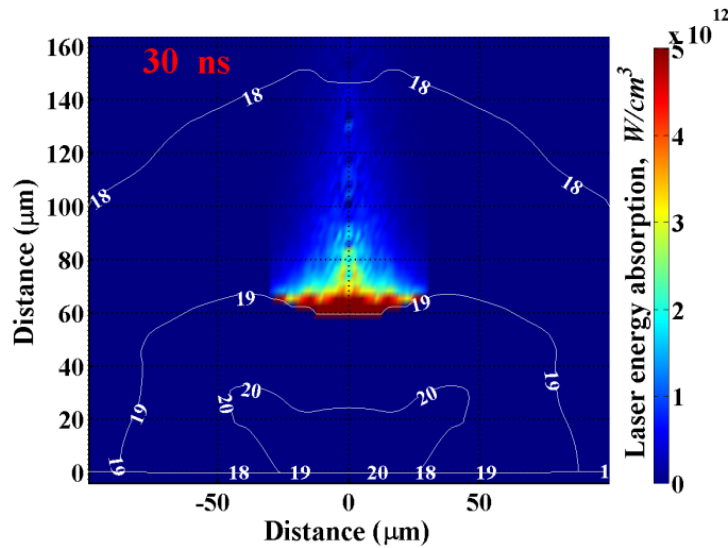


Fig. 37. Laser energy absorption at 30 ns in plasma created from tin foil by CO₂ laser. Plasma density is shown by white contours [58]

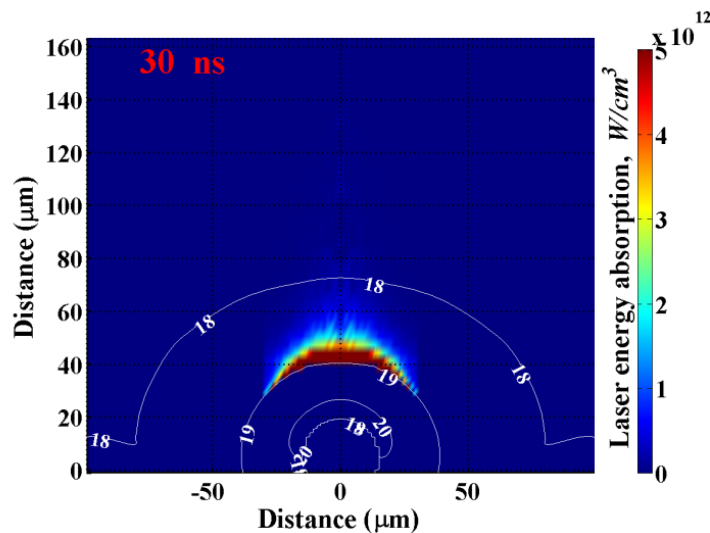


Fig. 38. Laser energy absorption at 30 ns in plasma created from tin droplet by CO₂ laser. Plasma density is shown by white contours [58]

Figures 39 and 40 show the spatial distribution of plasma temperature and density from planar and droplet targets, respectively, with approximately similar maximum temperature values. However, plasma from the planar target has larger area with better parameters for EUV photons emission, such as 30–40 eV temperature and 10^{19} - 10^{20} cm³ electron density.

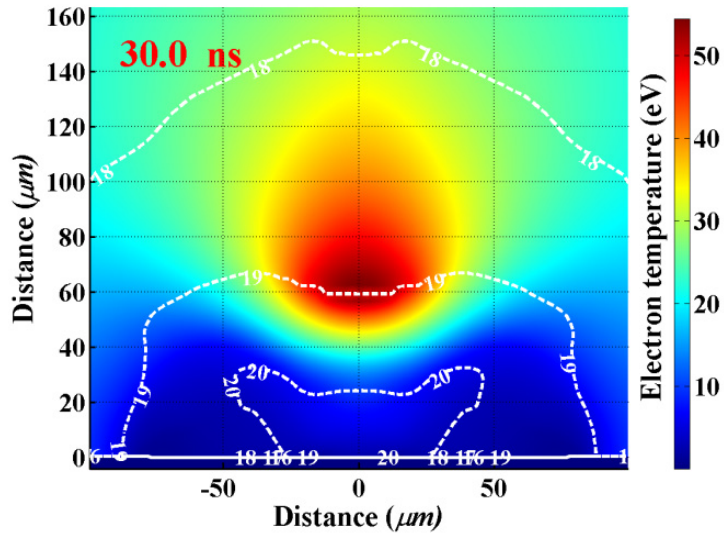


Fig. 39. Temperature and density (white contours) distribution at 30 ns in plasma created from tin foil by CO₂ laser [58]

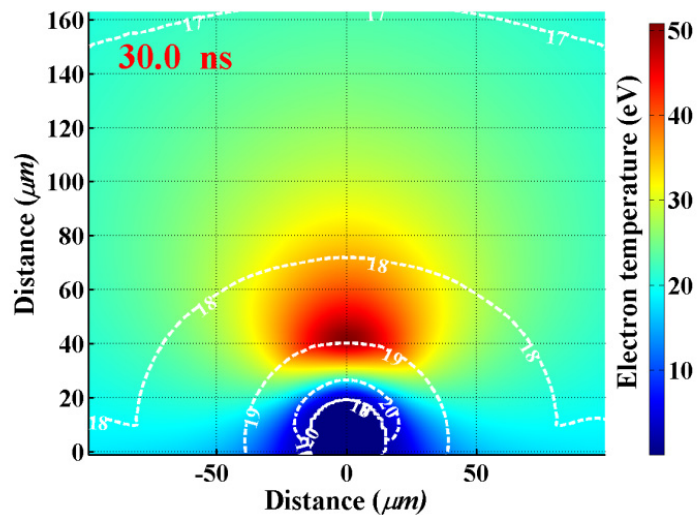


Fig. 40. Temperature and density (white contours) distribution at 30 ns in plasma created from tin droplet by CO₂ laser [58]

The implemented models in HEIGHTS Monte Carlo description for the radiation transport include detailed calculation of the opacities that allow precise prediction of EUV source location and strength based on the fundamental description of plasma radiation processes. Figures 41 and 41 show the EUV source location and intensity in plasma created by CO₂ laser from planar and spherical targets, respectively. Planar target produces EUV radiation source with lower intensity, because of the higher absorption of EUV photons in upper plasma layers with high temperature values. However, the source has larger EUV volume explained by the larger area with overall conditions appropriate for the better EUV radiation emission.

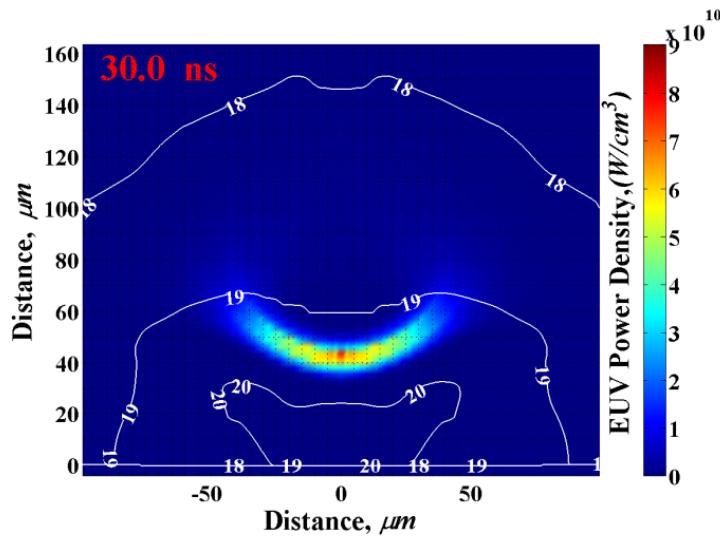


Fig. 41. Location and intensity of the EUV source at 30 ns from the planar target [58]

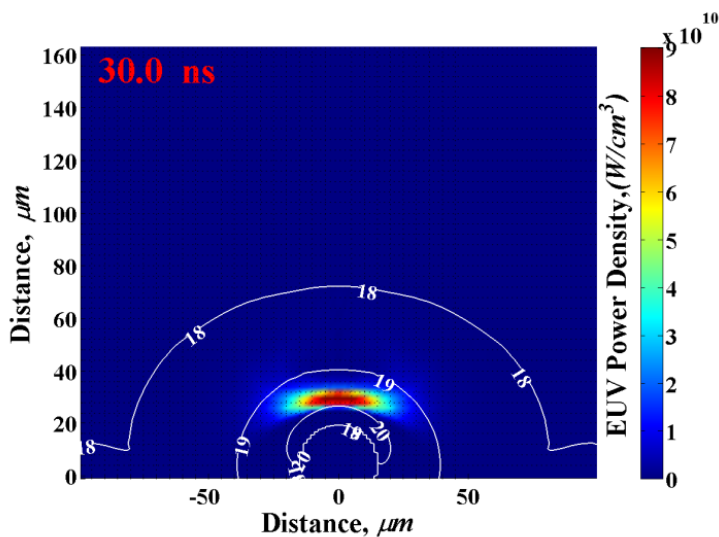


Fig. 42. Location and intensity of the EUV source at 30 ns from the droplet target [58]

Planar targets yield two times higher CE for the same CO₂ laser parameters, i.e., 1% (planar) vs. 0.45% (spherical). The low efficiency even for planar target in this case is due to the very small spot size used. Comparative analysis of plasma temperature and mass density distribution (Figs. 39 and 40) shows larger potential area for EUV photons emission in the planar target geometry. Increasing droplet size, e.g., to 100 μm, using the same laser parameters given above allowed slight increase in CE, up to 0.6%, that is still lower than for planar target and can be explained due to the combined effect of low plasma containment for the given geometry and the low efficiency of the CO₂ laser with the considered spot size (Fig.43). Figure 44 shows the distribution of plasma temperature and mass density for the case with larger laser spot size but the same intensity and duration were utilized. Such increase in the laser spot size together with the larger target surface allowed having the CE comparable to that of the planar geometry. All simulations described in this section utilized the CO₂ laser with 30 ns pulse (FWHM) and 5×10^{10} W/cm² intensity.

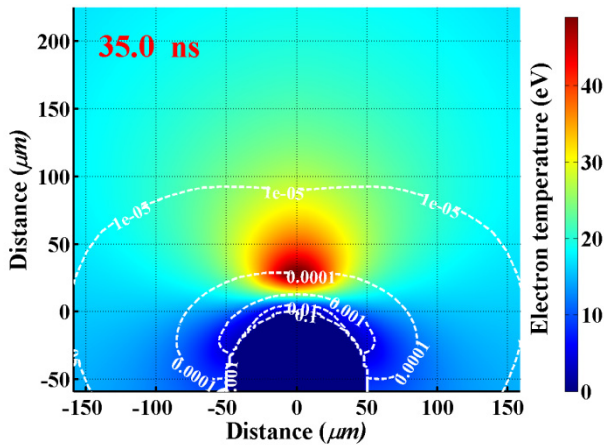


Fig. 43. Electron temperature and mass density (g/cm^3) distribution at 35 ns in plasma created from 100 μm droplet by CO₂ laser with 30 μm spot (0.6% CE) [61]

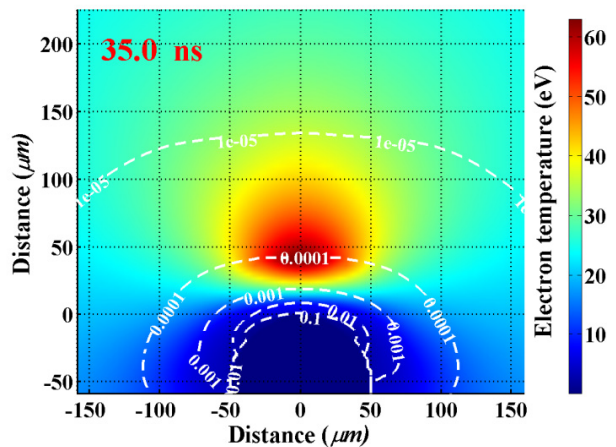


Fig. 44. Electron temperature and mass density (g/cm^3) distribution at 35 ns in plasma created from 100 μm droplet by CO₂ laser with 50 μm spot (0.9% CE) [61]

Figures 45 and 46 illustrate the difference in density and temperature distribution in plasmas created from tin foil by CO₂ laser with large and small spot diameters.

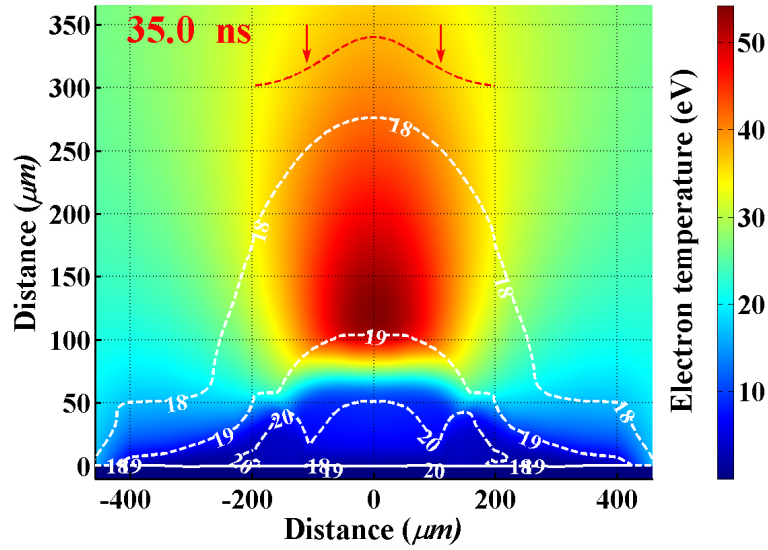


Fig. 45. Plasma temperature and density (white contours) distribution at 35 ns of CO₂ laser pulse with 220 μm spot diameter [62]

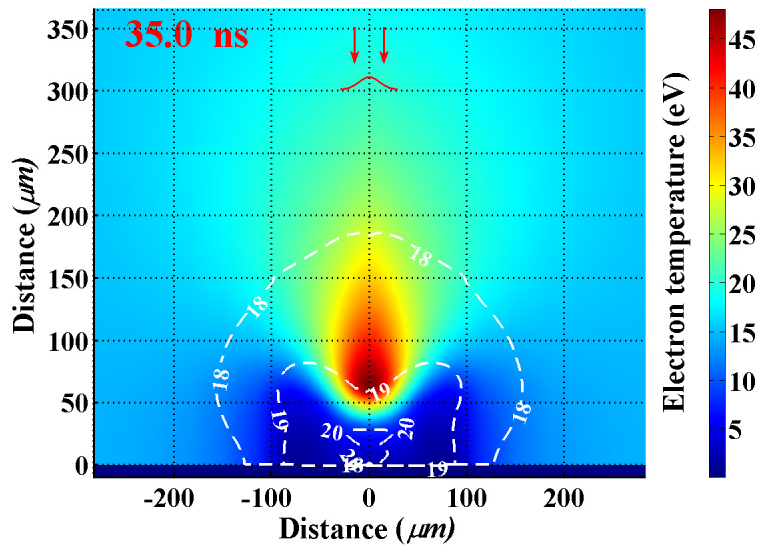


Fig. 46. Plasma temperature and density (white contours) distribution at 35 ns of CO₂ laser pulse with 30- μm spot diameter [62]

Optimized laser intensities were used for the considered spot sizes, 5×10^{10} W/cm² for smaller spot and 7×10^9 W/cm² for the larger one. Utilizing of these intensities allowed achieving approximately the same plasma temperatures range for both beams. The difference in plasma conditions in these two cases is related to the density distribution. Laser with larger spot created larger volume of plasma that provided better containment. This results in extended area with densities relevant to EUV photons emission correspondent to the ionic species of Sn⁸⁺-Sn¹⁴⁺.

Low efficiency of sources created by CO₂ lasers with small spots is more expressed in devices with small, i.e., 10-50 μm droplets. These devices have several advantages for the development of systems with high volume manufacturing such as possibility of efficient mechanism for target delivery and longer optical system and components lifetime due to reduced target mass and, therefore, reduced debris production. However, they require significant efforts for analysis and optimization to provide CE comparable with planar targets.

This modeling for small spherical targets showed another tendency in the effect of spot size on source efficiency for Nd:YAG and CO₂ lasers. In the case of Nd:YAG laser, reasonable reduction in spot diameter (FWHM) to the size smaller than droplet diameter allows producing more efficient EUV source. This is due to relatively high absorption of 1.064 μm wavelength on the target surface and in dense plasma above. Therefore, reducing spot size prevents laser photons loss due to target missing. Opposite situation appears for CO₂ laser. Laser photons with 10.64 μm wavelength are preferentially absorbed in relatively low density region. Hence larger volume with low dense plasma provides better conditions for the laser photons absorption. Therefore, laser beam with spot diameter even exceeding the droplet size can produce more efficient EUV source.

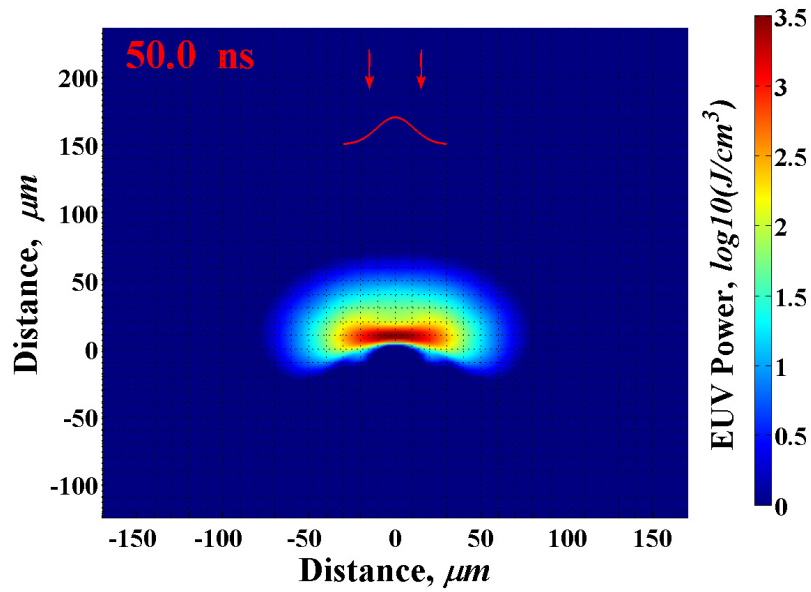


Fig. 47. EUV source from 30- μm droplet heated by CO₂ laser with 30 μm spot size [62]

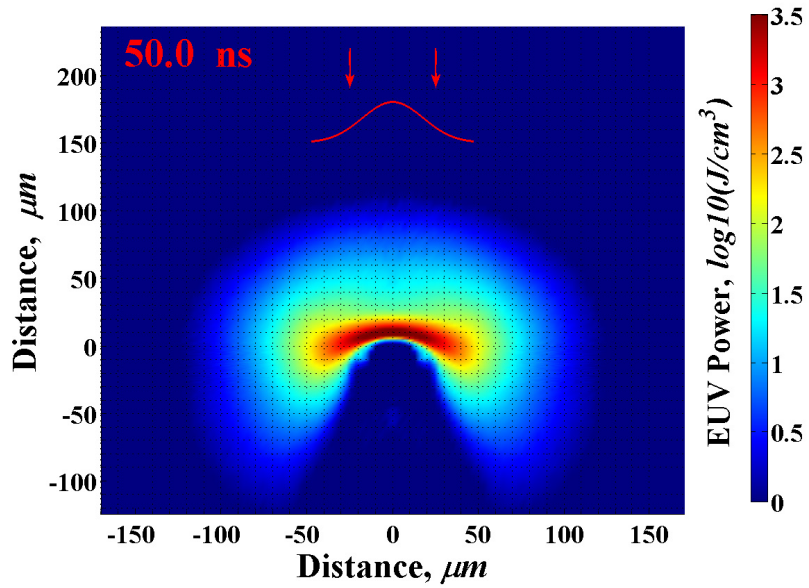


Fig. 48. EUV source from 30- μm droplet heated by CO₂ laser with 50 μm spot size [62]

Figures 47 and 48 show the EUV source size and intensity in plasmas created from 30 μm tin droplet by CO₂ laser with 30 μm (Fig. 47) and 51 μm spot diameters (Fig. 48). EUV photons were collected in 2π sr during 50 ns laser pulse. Increase of spot size in these cases allowed

increase in CE from 0.45% to 0.67%. These values are still much lower than the efficiency from a foil heated by laser with large spot; however, this example illustrates the way for such devices optimization that is a preparation of large volume of low dense plasma. The utilization of pre-pulses for target preparation prior to the main pulse can significantly increase CE of LPP sources with small droplets.

3.2 Complex mechanisms in optimization of dual-beam systems

The requirements for high EUV power, longer optical system and components lifetime, and efficient mechanisms for target delivery have narrowed investigators towards the development and optimization of dual-pulse laser sources with high repetition rate of small liquid tin droplets and the use of MLM optical system for collecting EUV photons. LPP sources with dual-beam lasers considering tin droplet sizes from 10 to 100 μm in diameter as single droplets as well as, for the first time, distributed fragmented micro droplets with equivalent mass were comprehensively simulated. The latter is to examine the effects of droplet fragmentation resulting from the first pulse and prior to the incident second main laser pulse. The effect of target mass and size, laser parameters, and dual pulse system configuration on EUV radiation output and on atomic and ionic debris generation was studied to obtain an ideal target. The ideal target is to generate a source of maximum EUV radiation output and collection in the $13.5\pm 1\%$ nm range with minimum atomic debris. This modeling and simulation included all phases of laser target evolution: from laser/droplet interaction, energy deposition, target vaporization, ionization, plasma hydrodynamic expansion, thermal and radiation energy redistribution, and EUV photons collection as well as detail mapping of photons source size and location. The potential damage to the optical mirror collection system from plasma thermal and energetic

debris and the requirements for mitigating systems to reduce debris fluence were also simulated and predicted.

3.2.1 Dual-pulse systems as ways for optimization of sources from small droplets

For obtaining the highest CE for EUV LPP source, ideal plasma temperatures and densities should be created for the longest possible period of time with the maximum size. There are several ways for optimizing LPP sources with mass-limited targets: 1) adjustment of target size and spot size; 2) increasing the time of laser pulse duration; and 3) preparing initial plasma by a pre-pulse. These options were studied in this optimization analysis.

Above simulation results showed that adjustment of target size and spot size in device with small droplets and single laser beam cannot provide EUV sources with high efficiency. Another concern of such devices is related to the high contamination of surfaces in LPP chamber by droplet fragments due to their low evaporation by single laser.

The lower mass ablation rate by the CO₂ laser beams with the longer wavelength and comparatively low value of the critical density for absorption of these photons allow source operation using longer pulses (100 ns and more) without significant reduction in the efficiency of EUV output [63]. Increased pulse duration, however, leads to increasing ionic debris producing and accumulation and therefore, decreasing mirror lifetime. Another disadvantage of longer pulses is the increase in EUV source size due to the large plasma expansion. While usually LPP devices provide smaller source sizes (compared to discharge produced plasma devices) that satisfy the optical system requirements for the etendue [64], CO₂ laser systems using larger spot sizes and long pulse duration (tend to increase the source size) compared to Nd:YAG lasers may cause difficulties in EUV photons collection.

The EUV source size from a tin plasma produced from both plate and droplet targets with the same parameters of a CO₂ laser was analyzed. A 100 μm spot size (FWHM) and long pulse duration of 90 ns were used. The difference in the hydrodynamics of plasma motion in these two systems determines the differences in the EUV source size and shape.

Figures 49 and 50 show the areas of emitting EUV photons that are collected in 2π sr during 150 ns. The expanded source in the planar case is explained by the changes in the source location with time, and this is related to the movement of plasma plume with the optimal combination of temperature and density values. This is specifically related to the CO₂ laser system, where EUV radiation is produced in low-density region that moves and expands more easily. Plasma motion around droplet in the spherical target case prevents plasma accumulation above the target. Planar target provided more efficient source with increasing CE of more than 30% for these conditions. This is a consequence of the hydrodynamic evolution where the plasma geometrical containment can play an important role.

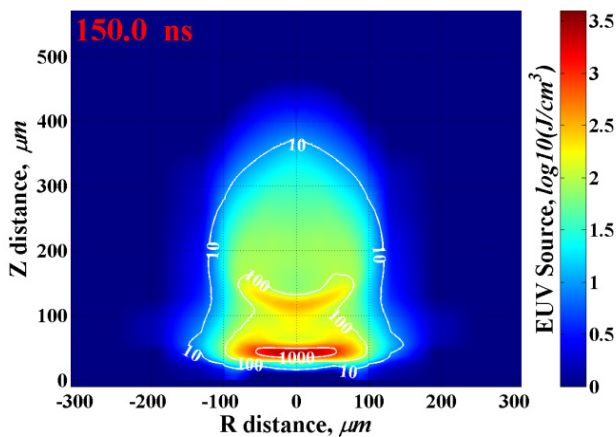


Fig. 49. Location and intensity of the EUV power collected during 150 ns in 2π sr in planar target [18]

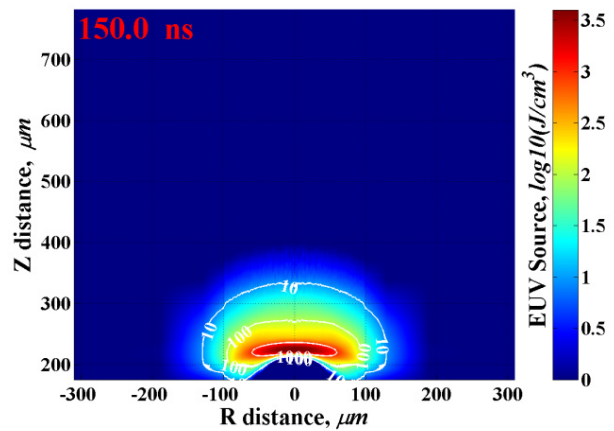


Fig. 50. Location and intensity of the EUV power collected during 150 ns in 2π sr in spherical target [18]

The effect of initial pre-pulses of laser energy and the dependence of laser wavelengths on the conversion efficiency for various target and laser beam conditions were studied. This analysis showed that the plasmas produced by both 1.06 μm and 10.6 μm radiate efficiently in the in-band radiation when they possess temperature in the $\sim 30\text{-}50$ eV range. However, the 10.6 μm laser excitation provides higher conversion efficiency from preheated mass-limited targets or from targets with complex geometry. The major difference between plasmas, created by CO₂ and Nd:YAG lasers, lies in the evolution of their densities, both temporally and spatially.

3.2.2 Dependence of laser energy absorption efficiency on plasma conditions

First, the percentage of useful laser energy which is absorbed in matter for the optimum intensity of CO₂ laser beam with 100 μm spot size (FWHM) and 30 ns pulse width on 30 μm tin droplet was evaluated.

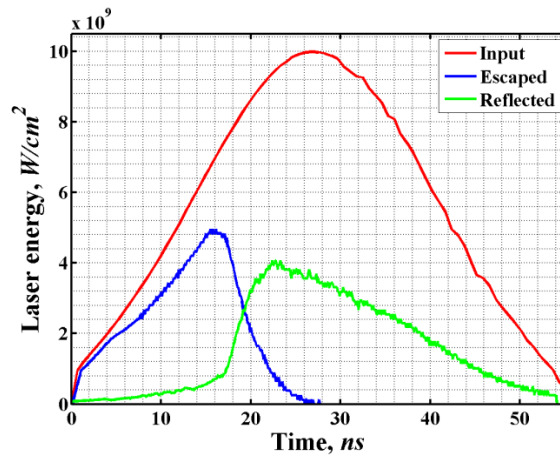


Fig. 51. Laser energy distribution for 100 μm spot size (FWHM), 30 ns duration (FWHM) and $1 \times 10^{10} \text{ W}/\text{cm}^2$ intensity; droplet diameter 30 μm [18]

Figure 51 shows the results of comparison, obtained by means of HEIGHTS package, of the input laser power and the lost power, i.e., escaped and reflected energy as a function of time. Since the spot size of the laser exceeded the droplet diameter in more than three times, major part

of laser photons didn't interact with the target until a plasma plume was formed with sufficient density needed for the absorption of laser photons at this wavelength. The conditions at which the evolving target plasma started to interact with the laser beam are at about 20-25 ns from the start of irradiation. The corresponding mass density distribution of the initial plasma is shown in Fig. 52 at the time of 20 ns.

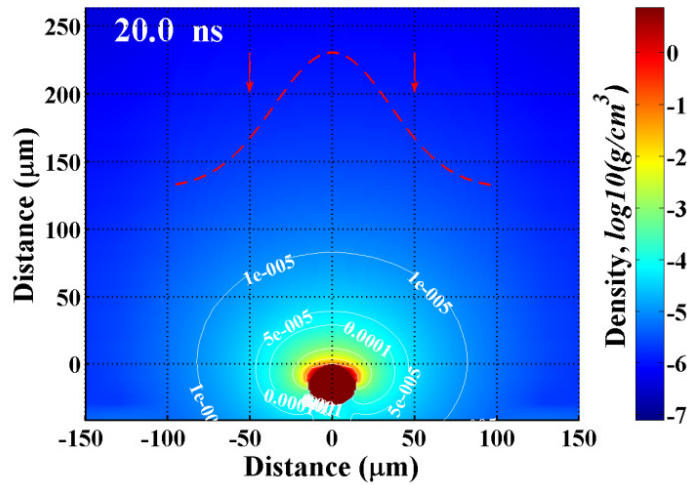


Fig. 52. Mass density distribution of plasma plume from tin droplet of 30 μm diameter [18]

Preheating the droplet by a laser with shorter wavelength and the resulting initial plasma plume formation can reduce energy losses of the main pulse. A second harmonic of Nd:YAG laser was used in these numerical simulations for the heating, evaporation, and initial ionization of the droplet target. Figure 53 shows comparison of laser energy absorption for Nd:YAG (second harmonic of 532 nm) at the intensity of $5 \times 10^{11} \text{ W/cm}^2$ during 10 ns and CO_2 at the intensity of 10^{10} W/cm^2 for two cases with and without pre-pulse interacting with 30 μm initial droplet size. Figure 54 shows the mass density distribution as a result of the pre-pulse laser that expanded during 80 ns. In both cases CO_2 laser heated the plasma up to a maximum temperature of 50 eV; this temperature indicates that plasma plume with optimum conditions for EUV

production was created. The improved absorption of the laser energy increased CE value up to 50%.

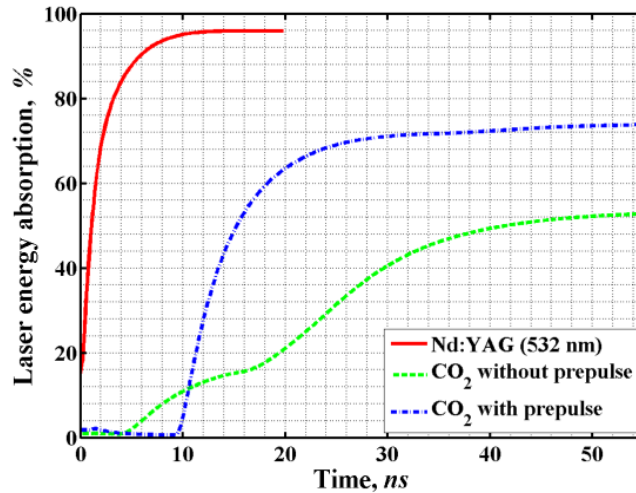


Fig. 53. Laser energy absorption at optimized intensities of: 1) 532 nm laser; 2) CO₂ without pre-pulse; 3) CO₂ after pre-pulse [18]

In this numerical simulation the initial plasma was created by 532 nm laser with the intensity of 10^{10} W/cm², which did not create plasma with conditions suitable for EUV emission during pre-pulse.

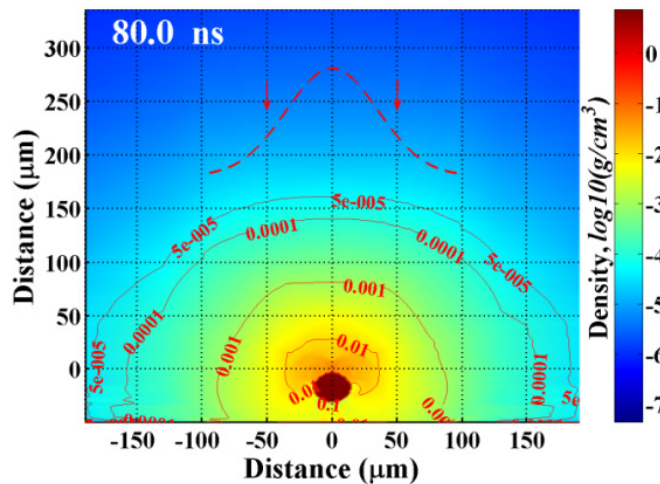


Fig. 54. Mass density of plasma plume from the droplet of 30 μm created by 532 nm laser and expanded during 80 ns [18]

Increasing the delay time between the pre-pulse and the main pulse did not influence much on the EUV production by the main CO₂ laser. After the time moment when the mass density of about 10^{-4} g/cm³ reaches the borders of the spot radius (around 30 ns for this droplet size and the pre-pulse energy), additional plasma expansion does not significantly improve EUV production. The change in the CE for 30 ns and 80 ns delay times was only about 10%. A more important parameter in this case is the spot size of the main laser beam, which can be adjusted to the delay duration and as a result to the evolving plasma size. Double increase in spot size of CO₂ laser led to an increase in CE of more than two times with a conversion efficiency that is comparable to that received for planar targets, i.e., of about 1.8%.

Since the time dependence of EUV output always follows the time profile of the laser beam, it is also reasonable to use the pre-pulse laser intensity suitable for in-band emission at this stage. To achieve the maximum EUV output optimized parameters for pre-pulse beam were used, i.e., 10^{11} W/cm² of 1064 nm with 100 μm spot on the same diameter of a tin droplet. We obtained a conversion efficiency of about 1.7% for this pulse. Next we allowed the plasma plume to expand during 40 ns and then applied a main CO₂ laser pulse with 30 ns duration and an intensity of 10^{10} W/cm² with various spot sizes. Figure 55 shows the influence of the spot size on EUV production at the above stated conditions.

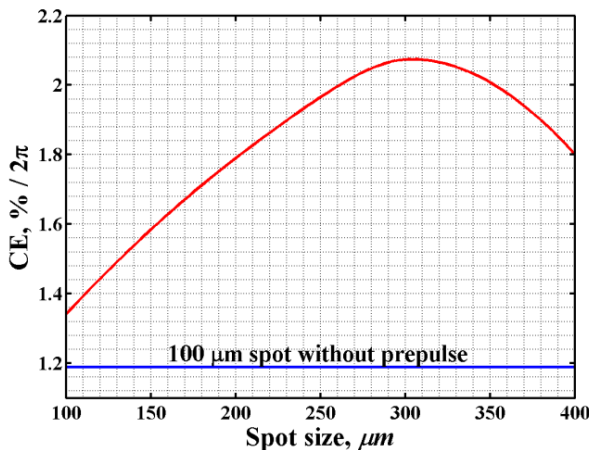


Fig. 55. The dependence of CE on CO₂ spot size applied after pre-pulse on tin target. For comparison CE of CO₂ laser with 100 μm spot size and 100 μm droplet without pre-pulse is given [18]

Two parameters can influence the efficiency of the EUV source in mass-limited target systems: relatively larger spot size and sufficiently prepared mass density to absorb the incident laser energy with such spot size. Mainly lasers with short wavelengths (harmonics of Nd:YAG) can be used for the first stage since they have better absorption in solid and liquid matter. The CO₂ laser can then be the best choice for the second stage, i.e., EUV production stage, since the evolving plasma plumes are more suitable for the absorption of such longer laser wavelength.

The models for self-consistent description of laser energy absorption combined with target material vaporization are critical parts in the simulation of LPP systems [61]. This is more pronounced in the case of lower laser intensities, i.e., 10^8 - 10^{10} W/cm², and in plasma development from small targets with non-flat geometries. This becomes important because of the complex hydrodynamic flow near the target surfaces where one should take into account various energy input from laser radiation, i.e., absorption/reflection in solid/liquid target, in target vapor, and in evolving plasma layer. The entire processes should consider various phases of transition from the laser interaction with material only (in vacuum chamber) to the preferential absorption in the developed hot plasma. The CE of EUV sources depends on many parameters including the initial target preparation stage as well as the efficiency of laser energy absorption in the developed plasma plume. In this regard, taking into account laser photons absorption after reflection from the target surface can be very important in determining the overall CE of the source.

Figure 56 demonstrates the efficiency of the CO₂ laser energy absorption on the surface and in the developed plasma from small 30- μ m droplet. Figure 57 shows the same but for the pre-plasma created by low intensity Nd:YAG pre-pulse from same size droplet after 450 ns expansion. Only 50% of laser energy was absorbed by the target and by plasma in LPP without

pre-pulse, while in device with pre-plasma about 90% of laser photons was utilized. It should be noted that the 266 nm wavelength laser for the pre-pulse with low intensity of 2.5×10^{10} W/cm² and 10 ns pulse duration was used. Laser with these parameters vaporized most of the droplet. This allowed accurate simulation of vapor/plasma expansion before the main CO₂ pulse and without concerns about target fragmentation processes. The CEs stated in Figs. 56 and 57 labels are the optimized values for these systems.

More than half of the initial laser energy was reflected from the surface of small spherical targets (Fig. 56) – corresponding to the sum of both green and gray plots. However during the increase in the laser intensity with time, that caused increase in plasma density and temperature, many of the reflected photons were absorbed in the evolving plasma. When the laser intensity starts to decrease, plasma above the surface begins to cool down and density of the plasma is subsequently reduced because of plasma expansion and the flow around droplet as well as lower evaporation rate in comparison with the beginning of laser pulse. These processes resulted in lower absorption of the reflected photons that can affect and be an indicator for lower LPP source efficiency. It was shown in the previous analysis of comparing plasma behavior in LPP with planar and spherical targets using the same laser parameters [58] that the laser absorption rate in plasma for planar target is 30% higher than from droplets. The CE of the planar target is two times larger in these cases. Modeling and implementation of laser photons absorption in plasma after reflection from the target can, therefore, significantly affect the final EUV collected power. Not taking into account this effect during laser-target/plasma interaction of these small droplets and small spot sizes significantly decreased the CE of this system of more than three times.

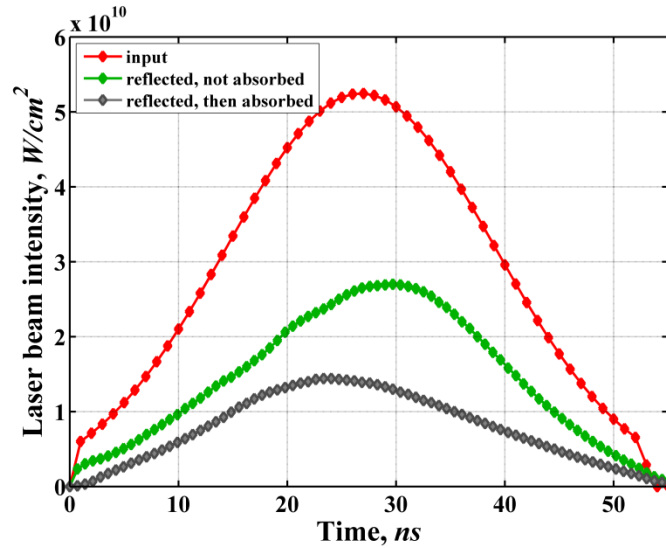


Fig. 56. CO₂ laser energy absorption in material and in plasma from 30 μm droplet without pre-pulse – 0.45% CE. Gray curve shows laser energy which was absorbed in plasma after reflection, green curve shows reflected laser energy which was not absorbed in evolving plasma [61]

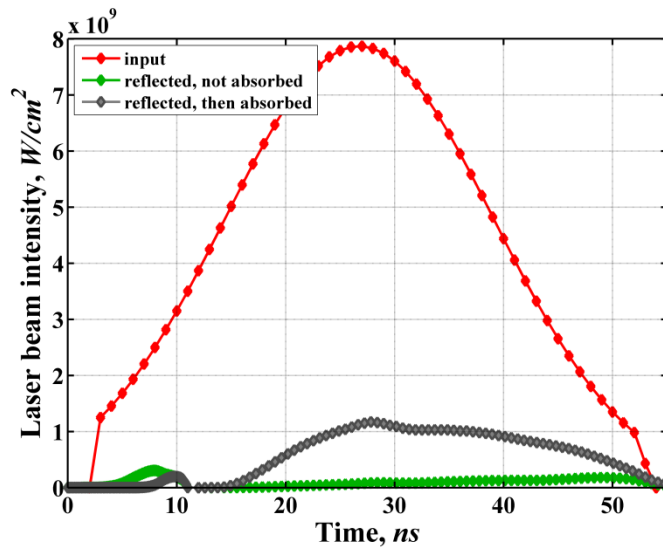


Fig. 57. CO₂ laser energy absorption in pre-plasma created from 30 μm droplet by 266 nm laser and expanded during 450 ns – 2.9% CE. Gray curve shows laser energy which was absorbed in plasma after reflection, green curve shows reflected laser energy which was not absorbed in evolving plasma [61]

The time history of laser photons reflection and absorption after reflection during reheating of the pre-plasma by the main CO₂ laser is shown in Fig. 57. This illustrates the evolution of

processes in pre-plasma starting from cold vapor/plasma where almost all photons were transmitted through matter. Reflection processes and following absorption after reflection correspond to the time of the intense interaction of laser photons with the remained non-vaporized part of the droplet. When the laser intensity increased almost all photons were absorbed in the heated pre-plasma zone, far from the target surface. Then due to the hot plasma dynamics and compression toward the target position (specificity due to CO₂ laser interaction with pre-plasma), area of preferential laser absorption also moved closer toward the target. Laser photons then had more interactions with target surface and as a consequence more reflected and reabsorbed photons occurred at this time.

Figures 58 and 59 stress these points and illustrate areas of accumulated laser energy absorption during the pulse with the corresponding location of droplets.

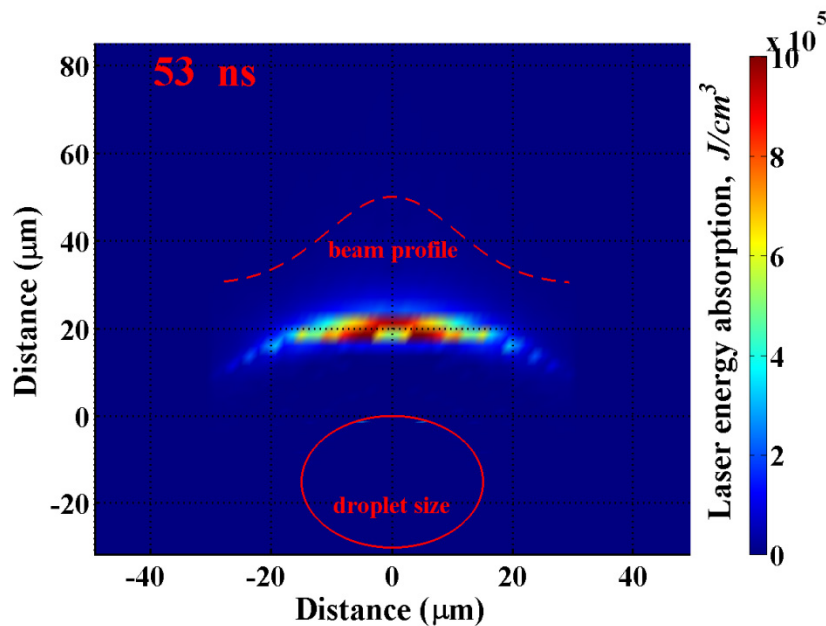


Fig. 58. CO₂ laser energy absorption during pulse in material and plasma from 30 μm droplet without pre-pulse. Laser pulse was used with 30 ns (FWHM) duration and 30 μm (FWHM) spot size [61]

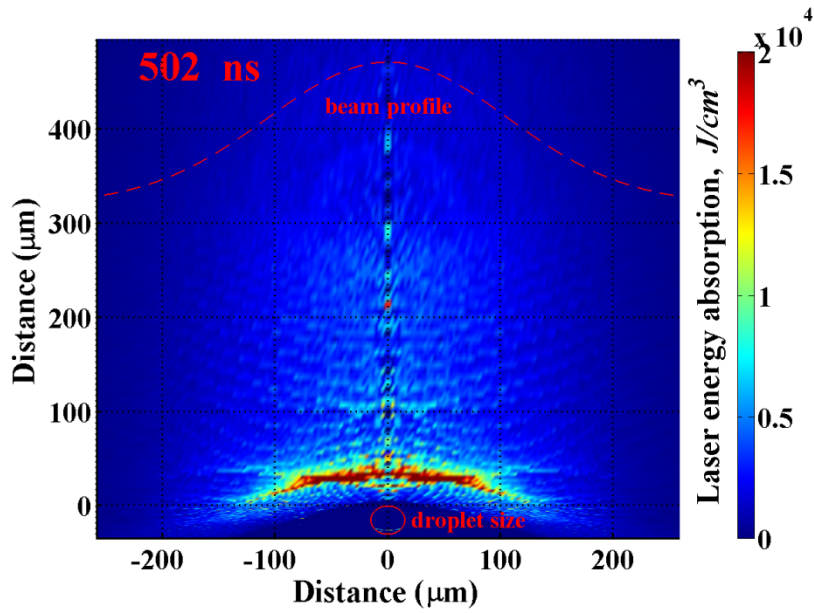


Fig. 59. CO₂ laser energy absorption during pulse in pre-plasma created from 30 μm droplet by 266 nm laser and expanded during 450 ns. Laser pulse was used with 30 ns (FWHM) duration and 300 μm (FWHM) spot size [61]

Currently, small droplets with sizes of 10 - 30 μm are considered as the most perspective targets, since one of the main goals in the development of EUV source for high-volume manufacture is increasing optical components lifetime that is to minimize the debris generation and deposition in the source chamber. Small sizes of target leads to utilizing reasonable small spot size of the laser beam and such restriction of sizes results in: 1) increasing the relative part of laser energy for initial heating of the target, since decreasing FWHM of the laser beam intensity having Gaussian spatial distribution leads to spending larger part of the energy for heating target surface due to thermal conduction; 2) delaying the processes of vaporization and plasma plume formation, since smaller spot size leads to lower evaporation rate that results in slower process of vapor/plasma plume formation suitable for laser photons absorption; 3) reducing the size of EUV source area and, therefore, decreasing the brightness of source, and 4)

loss of the plasma geometrical containment, that is related to the hydrodynamic motion of plasma around the spherical target reducing plasma density above the droplet. As a result, small spherical targets give significantly lower CE, especially in the case of CO₂ laser.

Dual-pulse systems allow increasing efficiency of LPP devices with small droplets. The process of heating Sn droplets by laser energy results in formation of vapor (detached neutral atoms), fragments (clusters of atoms), and plasma. Final target decomposition to these elements depends on the droplet size and laser beam parameters. In this regard two modes for utilizing prepared target matter can be considered. The first one is based on the heating by the main laser of plasma plume created at the pre-pulse stage and expanded during the short time, up to 100 ns. The second one is related to utilizing the evaporated and fragmented parts of the droplet. Heating of this matter is reasonable after delay in the μ s range, since velocities of this components is 10-100 times lower than plasma velocity [65] and spatial expansion of such matter to areas covered by the larger plasma spot requires longer time.

Just as a note, previous theoretical [66] and experimental [19] studies showed significant increase of CE due to implementation of dual-pulse with 1064 nm laser as the pre-pulse and 10 μ m for the main pulse. However, 1064 nm pre-pulse laser cannot efficiently evaporate the entire droplet due to the relatively low critical density value. For example, low intensity, 5×10^8 W/cm², of pre-heating laser in [66] will lead to the low evaporation rate of 40 μ m droplet, considered in this study, that results in large tin debris accumulation in the chamber. High intensities of pre-pulse laser used in [19] will result in producing tin ions with high energies that also can affect the collecting optics system lifetime.

The evaporation rate of small droplet in dependence on the pre-pulse laser wavelength was analyzed. Then, the effect of pre-pulse conditions on EUV source efficiency was evaluated and

plasma/vapor expansion developed from the most vaporized target (e.g., 80% of 30 μm droplet) was modeled, optimizing delay between pre-pulse and main pulse and then adjusting spot size of the main, CO_2 , laser to get efficient conditions for EUV photons output. Experimental results for the same droplet diameter as in this study [59] showed from 2.3% CE to 3.25% CE with various pre-pulse techniques. The CE of 3% CE was obtained in these simulations that is close to the above data.

3.2.3 Influence of laser wavelength and intensity on vaporization dynamics

Accurate description of the following two processes can also be important in the modeling of LPP with lower laser intensities and pre-plasma creation from small targets with non-flat geometries, i.e., (1) laser energy absorption and (2) target material vaporization. Ideally, the laser absorption by a target should be treated in two phases: first by the cold, unperturbed solid/liquid target and then by the target having an evolving plasma layer above the remaining solid/liquid target. This becomes important because of the complex hydrodynamic flows near the target surfaces where the various energy input from laser radiation should be taken into account, i.e., absorption/reflection in solid/liquid target, absorption/reflection in target vapor, and absorption/reflection in plasma layer. Because, for example, the production of the initial EUV radiation area above the target surface consumes part of the laser beam energy and part of main pulse duration, the final efficiency of LPP devices increases with decreasing the time needed for such preparation stage. This entire process includes gradual decreasing of laser absorption in cold material and increasing absorption in the hot plasma. It is also important to take into account the re-absorption of laser radiation in the evolving plasma after the reflection from the liquid target surface. Vaporized layer above the target surface initializes process of laser photons absorption in vapor/plasma that prevents their penetration to the target surface. At the same time,

radiated plasma photons add their energy to the heating of droplet and this energy load to the target can be significant from the well-developed hot plasma plume.

The mechanisms and models in the formation of laser-produced plasma described above and implemented in the HEIGHTS package allow prediction of vaporization rate with acceptable accuracy. For the considered time of the pre-pulse laser duration, 10 ns, possible target fragmentation and fragments distribution can be neglected. Gaussian spatial and temporal profiles of laser beam energy and the same beam diameter along laser path in simulated domain were assumed. Time counting starts from the beginning of the pre-pulse laser.

Figures 60-63 illustrate the process of pre-plasma creation, i.e., vaporization and plasma formation by the pre-pulse lasers with two different wavelengths and with the same other parameters such as 10 ns pulse duration and 10^{10} W/cm² intensity, 30 μm spot on 30 μm droplet. Tin droplet with this size has mass of 10^{-7} g. Laser beam with 266 nm wavelength and this intensity only vaporized one third of the droplet.

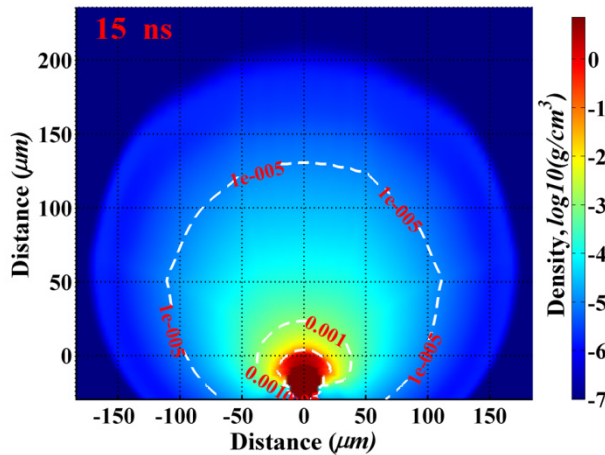


Fig.60. Mass density distribution at the end of pre-pulse laser beam with 1064 nm wavelength and intensity of 10^{10} W/cm² [57]

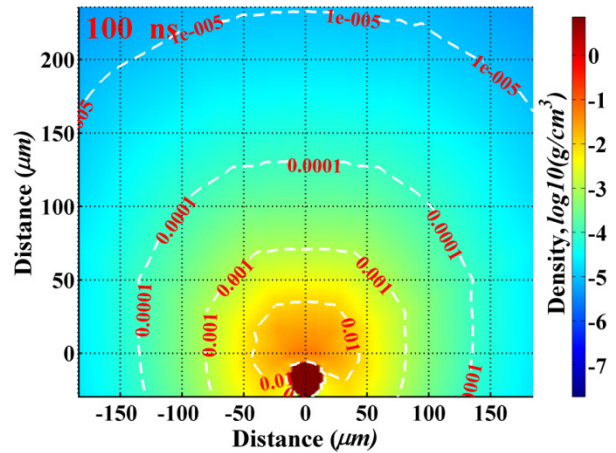


Fig.61. Mass density distribution after 100 ns delay in pre-plasma created by the laser beam with 1064 nm wavelength and intensity of 10^{10} W/cm² [57]

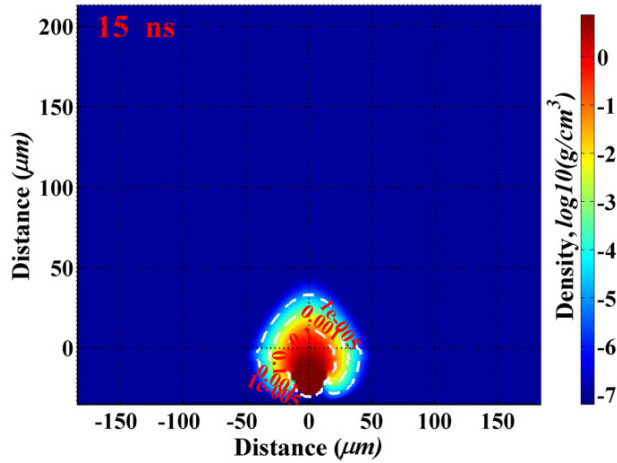


Fig.62. Mass density distribution at the end of pre-pulse laser beam with 266 nm wavelength and intensity of 10^{10} W/cm² [57]

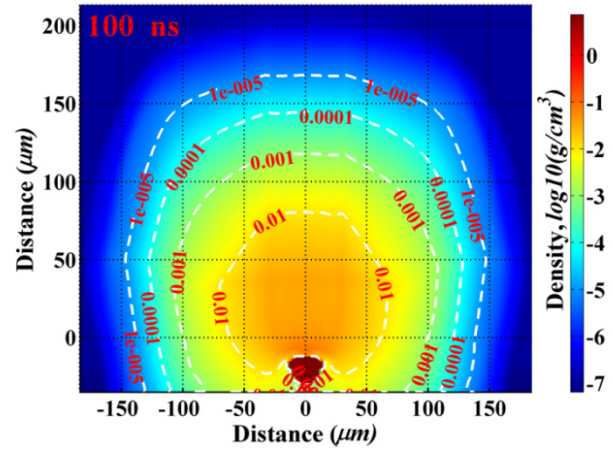


Fig.63. Mass density distribution after 100 ns delay in pre-plasma created by the laser beam with 266 nm wavelength and intensity of 10^{10} W/cm² [57]

The dependence of vaporization rate on laser beam wavelength, energy, and spot size is nonlinear since this process, in self-consistent simulation, depends on 1) the time of initiation of laser energy absorption in plasma that reduces energy load to the target; 2) geometry of target, since heating of the droplet by the laser and by the plasma itself can cause vaporization from the sides of droplet; and 3) generated photon flux in evolving plasma and transport to original target surface.

Figure 64 shows evaporated mass during the laser beam pulse for two laser wavelengths. Figure 65 illustrates dependence of droplet vaporization, of the 1064 nm wavelength laser, on the intensity indicating less vaporized mass by more intensive laser beam. Laser with 1064 nm wavelength and high intensity evaporated sufficient mass during the first 2 ns. After this, almost all laser photons were absorbed in the developed plasma plume and the vaporization rate was low. This case clearly illustrates the vapor shielding effect.

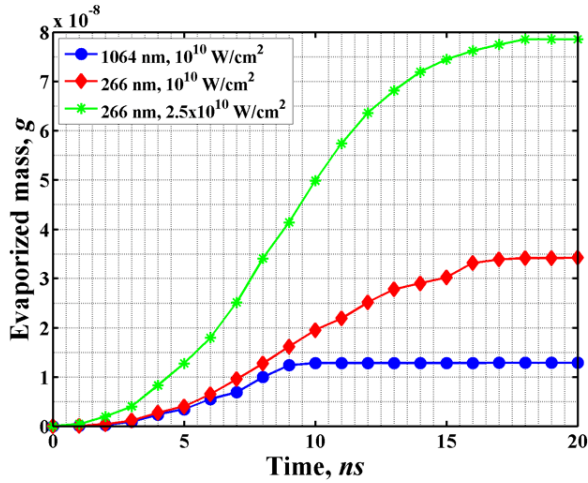


Fig.64. Dependence of evaporation dynamics on pre-pulse laser wavelength at different intensities. Laser beam parameters used are 30 μm spot size and 10 ns duration [57]

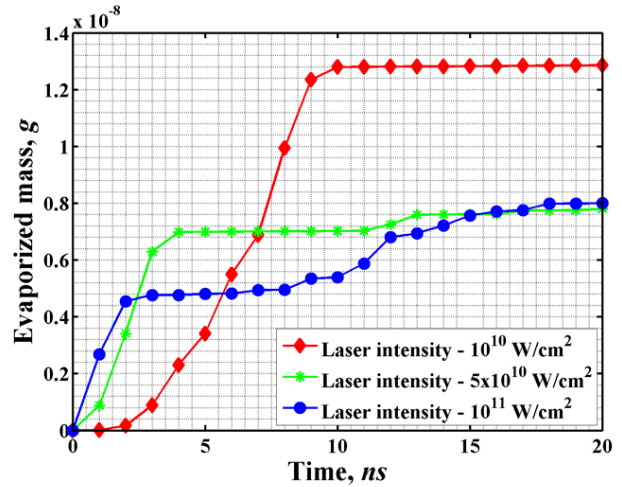


Fig.65. Dependence of evaporation dynamics on pre-pulse laser intensity at 1064 nm wavelength. Laser beam parameters used are 30 μm spot size and 10 ns duration [57]

The self-consistent modeling of processes during target ablation is necessary for the accurate predictions of plasma evolution and CE calculation. Initially laser photons start to heat the target surface initiating target vaporization. Subsequent laser interaction with the developed vapor/plasma results in reducing laser penetration to the target, however it initiates heating of the target from plasma radiation. Thermal conduction in plasma redistributes energy of absorbed laser photons that also affects dynamics of target vaporization through the radiation from the warm plasma around the target surface. Hydrodynamic effects such as spherical expansion of plume and plasma motion around the droplet result in density redistribution that changes dynamics of laser photons absorption as well as plasma radiation emission and absorption in evolving plasma and on the target surface.

Radiation transport can be one of the main mechanisms responsible for target heating and vaporization. Figures 66 and 67 show simulation results of tin foil ablation by CO₂ and Nd:YAG

laser with the same pulse parameters, i.e., 10^{11} W/cm² intensity, 100 μm spot, and 10 ns duration. This intensity of lasers created plasmas with temperatures up to 65 eV in case of Nd:YAG and up to 120 eV by the CO₂ laser. Most of laser photons were absorbed in the hot plasma. The temperature distributions in the target and erosion profile are attributed to the plasma radiation. Temperature profile on the surface demonstrates processes of plume expansion in LPP source with planar target, i.e., with denser plasma at the center of laser spot and with hotter less dense plasma correspondent to the wings of surface temperature.

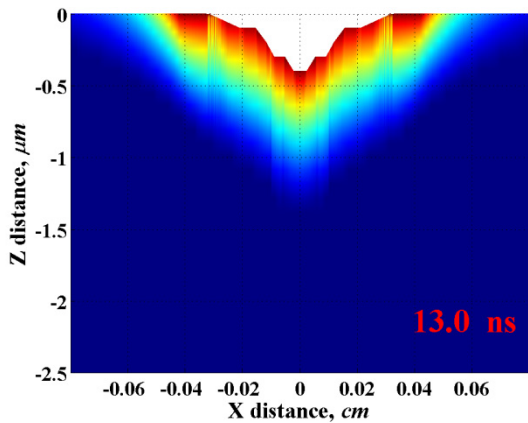


Fig. 66. Sn erosion by CO₂ laser with 100 μm spot and 10^{11} W/cm² intensity [61]

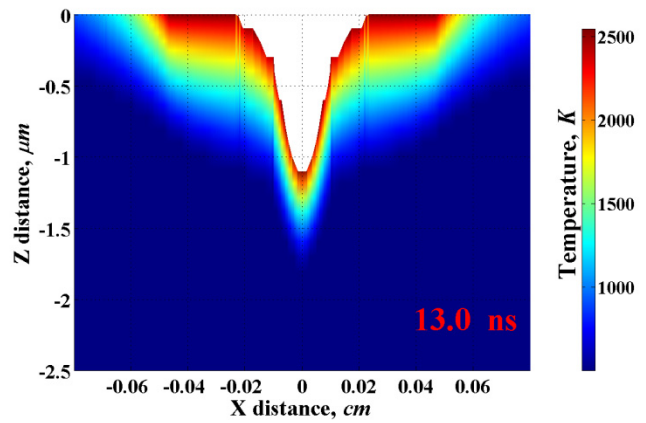


Fig. 67. Sn erosion by Nd:YAG (1064 nm) laser with 100 μm spot and 10^{11} W/cm² intensity [61]

Figures 68 and 69 show the corresponding predicted energy density to the target surface from the direct laser irradiation and from generated plasma integrated in time. These plots together with figures for the temperature distribution illustrate the strong effect of plasma shielding of laser photons as well as the role of plasma radiation for the considered laser beam intensity for both CO₂ and Nd:YAG lasers. Figures 68 and 69 reflect plasma evolution processes in LPP devices with relatively high laser intensity. The extensive evaporation of the target in the central spot area resulted in motion of vapor/plasma flow from the crater. On the other hand,

compression of plasma around the center area of the laser spot initiates free expansion of vapor/plasma around the spot. Radiation fluxes from this plasma heat the target surface in the location outside of laser area. However, due to less intensity but longer duration of this peripheral radiation as well as deposited energy dissipation due to thermal conduction, plasma radiation did not cause significant surface evaporation at this location in contrast to the conditions at the spot center.

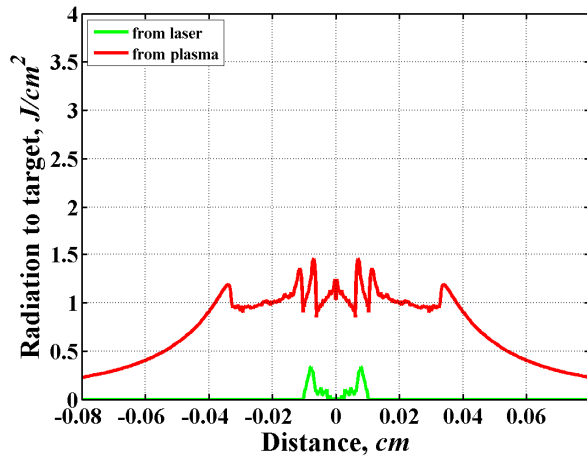


Fig. 68. Radiation to the target from laser and from plasma created by CO₂ laser with intensity of 10^{11} W/cm² [61]

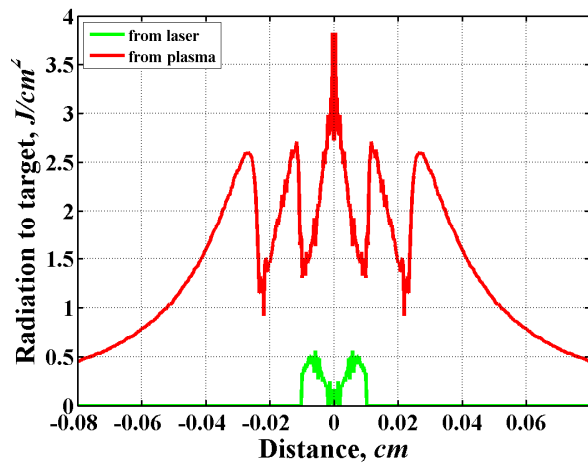


Fig. 69. Radiation to the target from laser and from plasma created by Nd:YAG laser with intensity of 10^{11} W/cm² [61]

Because of the deeper penetration of Nd:YAG laser photons in vapor/plasma plume and therefore higher energy transmitted to the target, such laser is more suitable for the pre-pulse stage. For the same reason, the fourth harmonic of this laser can even be more efficient in preparing the plume mist before the main pulse.

Modeling results [57] as well as experimental data [59] showed the importance of pre-pulse laser parameters for the target vaporization and creation of initial matter for the main laser pulse. Figure 70 shows vaporization rate during the heating of 20 μm droplet by the laser beam with

1064 nm wavelength and different intensities. Tin droplet with such size has mass of 3×10^{-8} g. Laser beam with 10^{12} W/cm² intensity only evaporated half of the droplet utilizing relatively large part of energy (30 mJ) for creation of pre-plasma that can significantly decrease the efficiency of whole dual-beam system.

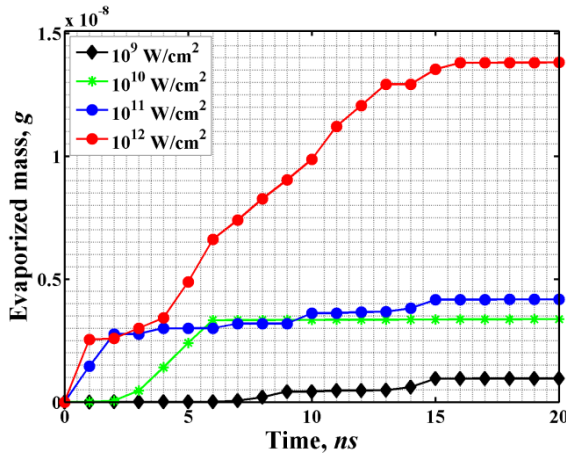


Fig.70. Dependence of evaporation dynamics on pre-pulse laser beam intensity at 1064 nm wavelength: total evaporated mass in g. Laser beam parameters used are 20 μ m spot size and 10 ns [58]

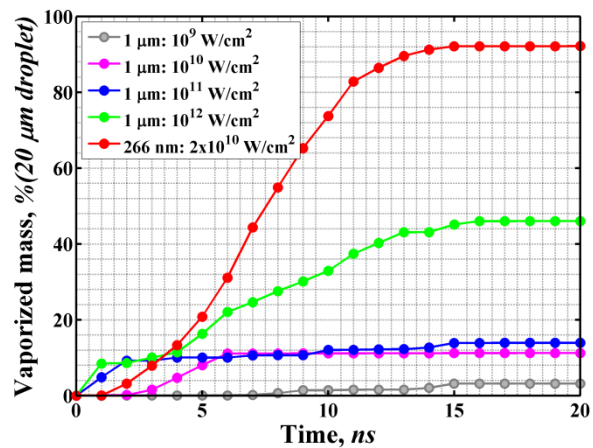


Fig.71. Percentage of evaporated mass from 20 μ m droplet. Laser beam parameters used are 20 μ m spot size and 10ns duration [58]

The high absorption of 1064 nm in the developed plasma plume is the reason of the smaller evaporated mass in this case. The fourth harmonic of Nd:YAG laser has higher critical density value and can be a better solution for higher evaporation of the small droplets with minimum energy loss. In such case, most of the 20 μ m droplet is vaporized when laser beam with 266 nm wavelength and 0.65 mJ energy was used as shown in Fig. 71. This is significant in reducing contamination from macroscopic debris and potential increase in components lifetime.

Laser with longer wavelength created warmer plasma that was expanded faster (Figs. 60-63), however it vaporized less mass that results in less dense plasma/vapor plume developed during 100 ns. The advantages of pre-heating small tin droplets by laser with shorter 266 nm

wavelength is higher evaporation rate therefore, lower accumulation of cluster debris; and lower temperatures of the developed plasma plume therefore lower fluence of energetic ions debris at the pre-pulse stage that can significantly extend optical collecting system lifetime.

Below the evolution of vapor/plasma mist from 50- μm droplet utilizing various lasers is studied in detail.

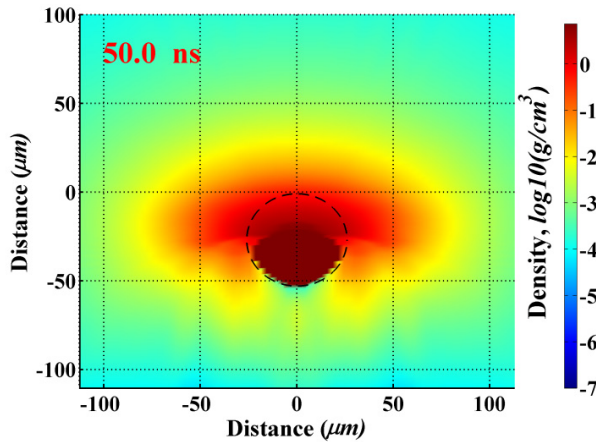


Fig. 72. Mist density from 50- μm droplet created by pre-pulse laser with 266 nm wavelength, ~ 10 mJ, 50 μm spot. Dotted line shows initial shape of droplet [20]

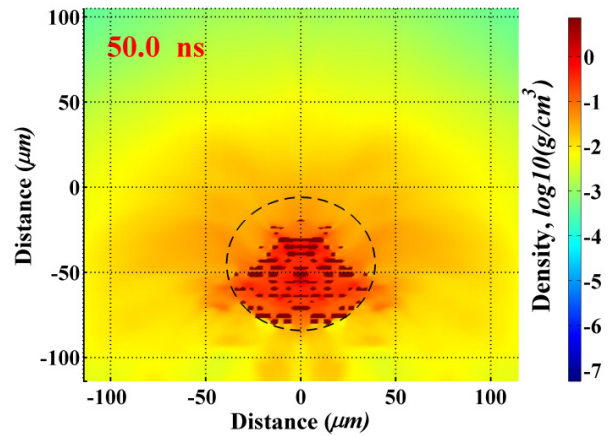


Fig.73. Mist density from 50- μm droplet created by pre-pulse laser with 1064 nm wavelength, 400 mJ, 100 μm spot. Dotted line shows initial configuration of fragmented droplet [20]

Figures 72 and 73 show mass density distributions developed by pre-pulse lasers having 266 nm and 1064 nm wavelengths respectively. In the first case, the 266 nm wavelength laser with about 10 mJ energy evaporated half of droplet. The longer 1064 nm wavelength laser evaporated approximately the same mass but with the intensity of 5×10^{11} W/cm², utilizing 400 mJ. For such high intensity laser and based on experimental results, droplet fragmentation during the laser pulse was implemented in this simulation. Therefore, droplet splitting into many fragments and their distribution during the 10 ns laser was assumed with expanding velocity of ~ 1 km/s predicted by recent experiments [19].

Lasers with 266 nm and 1064 nm wavelengths evaporated the same mass; however, the last stated parameters of laser with longer wavelength have several disadvantages for the pre-pulse stage. First, the laser energy required for the pre-pulse is comparable with the energy of main pulse, and this will significantly decrease the conversion efficiency of the entire system. Second, the maximum temperature of plasma plume developed by the longer wavelength reached 120 eV, while shorter wavelength created plasma with temperature up to 14 eV. Hot plasma with high velocities, up to 150 km/s, will have ions with energies up to 12 keV. The ions energy in the plasma created by 266 nm did not exceed 700 eV for this system. Such plasma expanded more uniformly, which created better conditions for EUV emission during the main pulse.

Because the 1064 nm wavelength laser with this intensity created plasmas with high temperatures, the energy redistribution due to radiation fluxes can play significant role in the hydrodynamic evolution of the plasma. The effect of radiation transport on target evolution was studied by modeling self-consistently all phases of laser/droplet interaction, target vaporization, target hydrodynamics, debris ionization, plasma formation and expansion, thermal energy redistribution, and photon generation and transport. Figure 74 shows vaporization dynamics and the contribution due to direct laser photons and to plasma, i.e., with and without the effects of RT. After the initial evaporation of sufficient mass layer needed for efficient laser absorption and the initiation of ionization processes, all laser photons are absorbed within this initially developed plasma/vapor plume. Photons generation in evolving plasma and their transport to the condensed target during and after the laser pulse caused most target vaporization. The influence of plasma radiation on vaporization rate is more pronounced for CO₂ laser even at low intensity, around 10^{10} W/cm², where more than 90% of evaporated mass was due to plasma radiation interaction with target (Fig. 75).

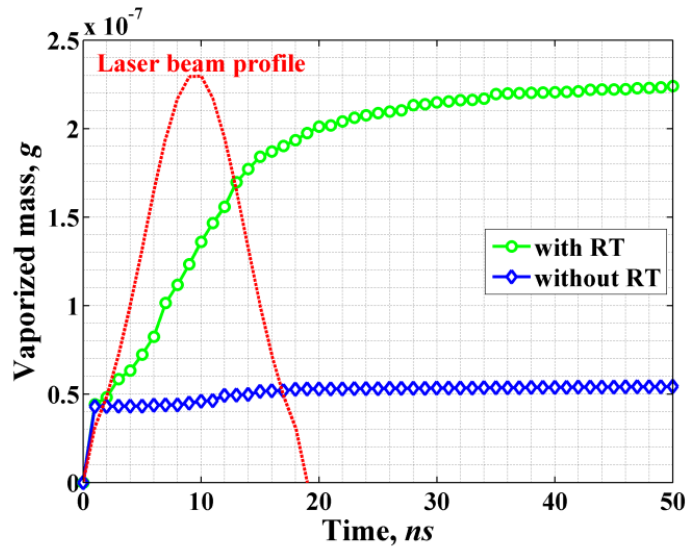


Fig. 74. Vaporization of 50- μm droplet by laser photons and by LPP with 1064 nm wavelength laser, 10 ns FWHM, 400 mJ, 100 μm spot [20]

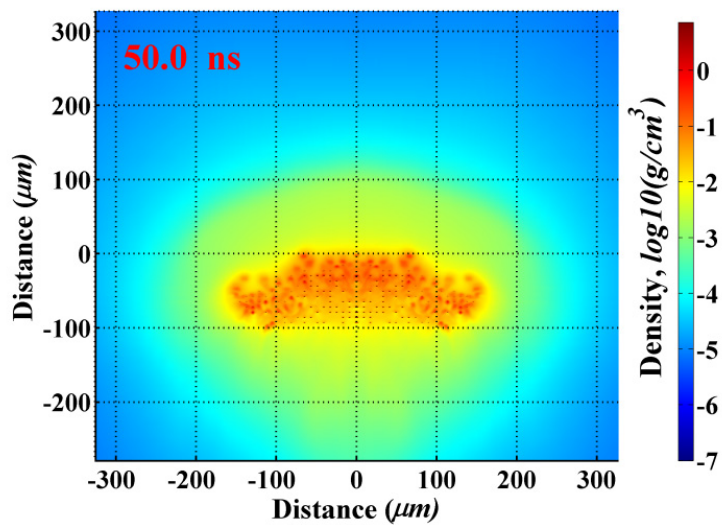


Fig. 75. Mass density evolution of distributed fragments after CO₂ laser pulse heating with total mass equivalent to 50 μm droplet [20]

The last example demonstrates the important effects of incorporating detail RT on mist plume evolution from the distributed fragments, and as a result on EUV photons source dynamics during the main laser pulse. Intensive evaporation of small fragments heated by radiation fluxes from the surrounding plasma leads to the formation of relatively cold dense plasma in the

volume occupied by the fragments. Such plasma cannot be an efficient source for the 13.5 nm EUV radiation. The EUV photons emission is possible only from plasma above the target surface with appropriate conditions, which are determined mostly by plasma region having temperature around 30-40 eV. Due to plasma plume expansion, the region with optimum conditions for EUV emission also moves away from the surface and this movement is more pronounced in the case of CO₂ laser because of the lower critical density and the usual long pulse duration of this laser. Such dynamics of EUV source produced from the larger area of distributed fragments resemble the high EUV emission and collection from a planar target and, as it will be shown later, these targets yield the same CE for the optimized parameters of the laser beam.

3.2.4 Dependence of source location and intensity on plasma conditions

The dependence of the source location and intensity on plasma conditions created by CO₂ laser and on plasmas heated after the pre-pulse was analyzed. The high reflectivity of the 10 μm laser and the small spot size are reasons of the low EUV intensity source and the small volume of EUV emitting area, created by this wavelength that also results in very low efficiency. Pre-plasma created by shorter wavelength extends the area suitable for CO₂ wavelength absorption.

Figures 76 and 77 show the location and intensity of EUV power collected in 2π sr during 70 ns from the plasma created by CO₂ laser without (a) and with pre-pulse (b). In the second case pre-plasma was created by 266 nm wavelength and expanded during 100 ns before the main pulse with 300 μm spot size impacted. For this case the CE of 1.7% was obtained.

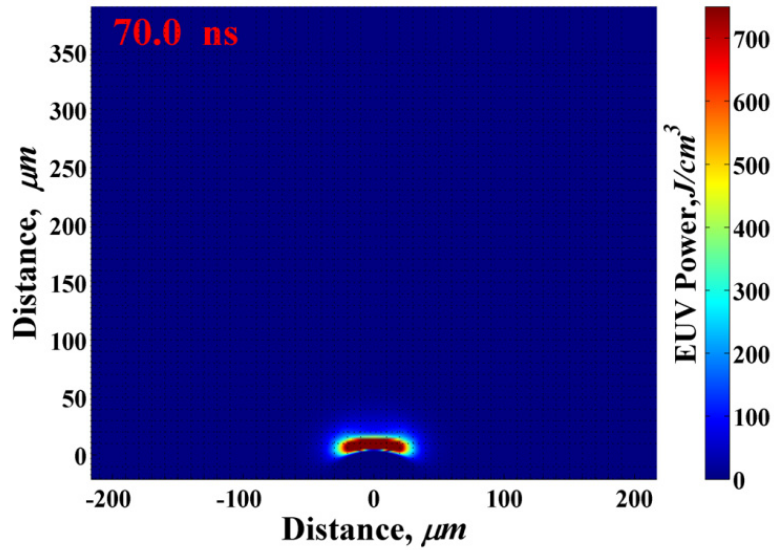


Fig.76. EUV source collected in 2π sr during 70 ns in plasma created by CO₂ laser without pre-pulse [57]

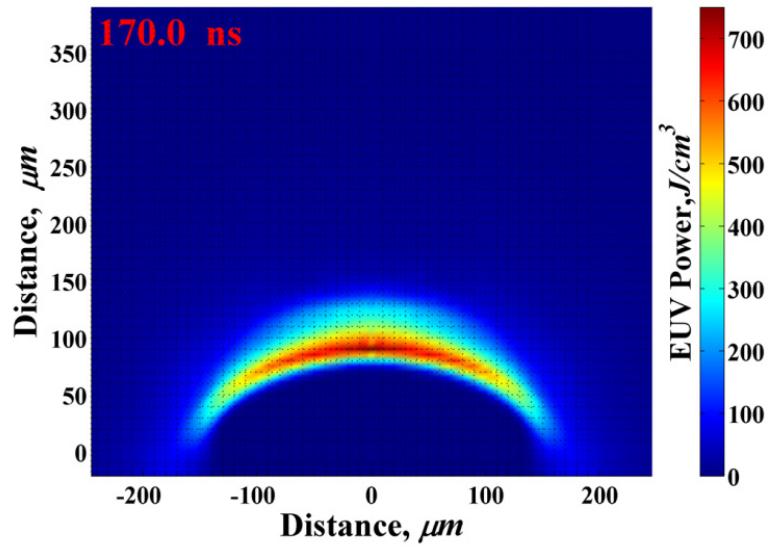


Fig.77. EUV source collected in 2π sr during 70 ns in plasma created by CO₂ laser with pre-pulse [57]

Figures 78 and 79 show another example of the difference in EUV source location and power density of EUV photons collected in 2π sr from plasma heated by the CO₂ laser with different initial plasma conditions.

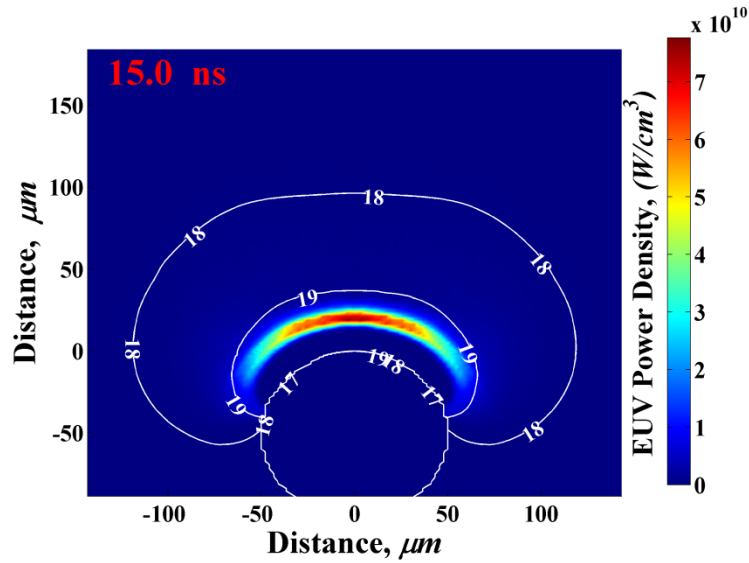


Fig. 78. EUV Source strength and location from 100 μm droplet without pre-pulse; CO₂ laser with 300 μm spot, 30 ns pulse [61]

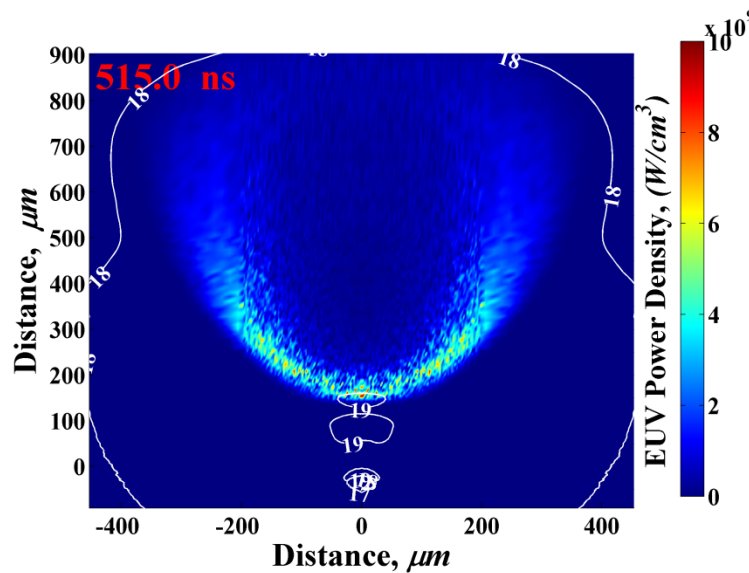


Fig. 79. EUV Source strength and location due to pre-plasma created from 50 μm droplet and expanded during 500 ns; CO₂ laser with 300 μm spot, 30 ns pulse [61]

In the first case plasma was created in vacuum chamber from droplet using single CO₂ laser during 15 ns of exposure (Fig. 78). In the second case plasma was prepared using pre-pulse laser, expanded during 500 ns, and then heated by main laser during 15 ns (Fig. 79). Larger plasma

plume allowed efficient coupling/utilization of laser energy and extended the area for EUV photons emission. Even higher intensity of EUV power from the single pulse did not compensate for the EUV collection from larger volume. Less than 1% CE from single pulse and more than 3% in the second case were obtained. Reducing spot size to match the droplet diameter did not significantly increase the efficiency of single CO₂ devices.

Because the evolving plasma plume above the droplet surface, created by the pre-pulse laser beam, can change the EUV production area during the main pulse similar to the planar target, the spatial distribution of the EUV source will have the same tendency in the size expansion. Therefore, in the optimization processes, one need to further adjust the spot and droplet sizes as well as pre-pulse/delay/pulse times. The resulting source size should be evaluated to satisfy the optical etendue system requirement that is the ability to collect light. Geometrical etendue is influenced by the area of the emitting source and the solid angle into which it propagates. Designed for EUVL optical systems have requirements that the etendue must be smaller than 1-3.3 mm² sr [64].

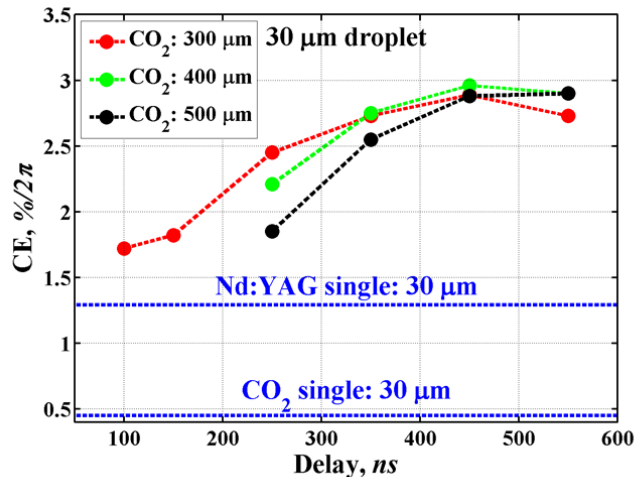


Fig. 80. CE from 30 μm droplet as function of delay between pulses and spot size of CO₂ [57]

Laser beam with 266 nm wavelength and the intensity of 2.5×10^{10} W/cm² vaporized 80% of 30 μm droplet. To evaluate the efficiency of the prepared plasma/vapor plume for EUV photons output the same CO₂ laser intensity, 7.5×10^9 W/cm², and pulse duration, 30 ns were used. Delay time and spot size of the main laser were varied. Figure 80 shows results of optimization of these two parameters. The CE from 30 μm droplet with CO₂ and Nd:YAG laser without pre-pulse are given for comparison.

Optimization of EUV sources from small droplet targets using dual laser pulses depends on many parameters and requires detailed analyses of pre-plasma conditions. For 1064 nm pre-pulse laser, tin evaporation rate decreased with increasing laser beam intensity from 10^{10} to 10^{11} W/cm², utilizing the same spot size as droplet diameter. Laser with 266 nm wavelength, penetrating deeper to the target, created denser but colder plasma/vapor plume that required more time for expansion to be efficient for the absorption of the 10 μm wavelength. Overall, efficient EUV source depends on combination of various parameters including pre-pulse laser wavelength/intensity, initial size of target/vaporization rate, and delay time/spot size.

3.3 Kinetic energies of ions in LPPs and their effect on optic mirrors life-time

To accurately evaluate the potential damage of MLM optical collection system by the energetic tin ions, the energy spectra of ions produced in both single CO₂ laser and dual-pulse systems was calculated and compared with recent experiments at CMUXE laboratory [60, 20].

Very good agreement between modeling and the experimental data was found as shown in Figs. 81 and 82. These results can be used as additional benchmarking of the HEIGHTS package and predict initial debris parameters for the simulation of Sn ions interaction with mirror surface using our ITMC-DYN code for ions/target interaction.

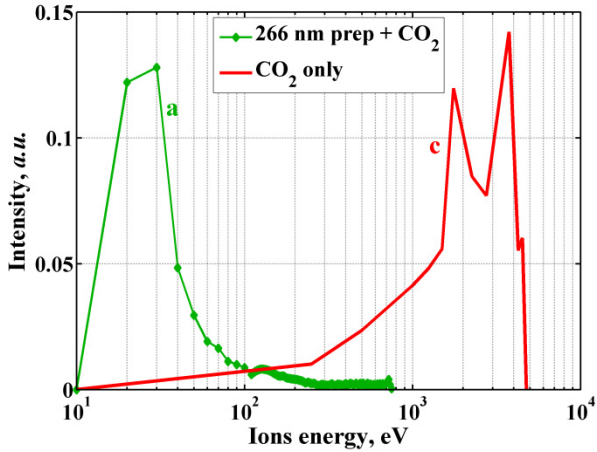


Fig. 81. Ions kinetic energies of HEIGHTS modeling of planar Sn target; 15 mJ for pre-pulse and 90 mJ for CO₂ laser [20]

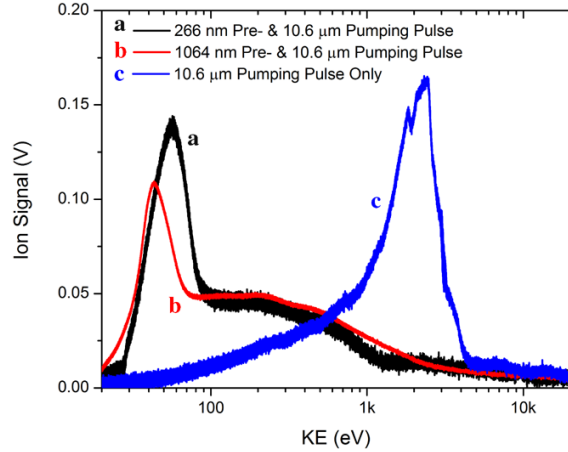


Fig. 82. Ions kinetic energies in CMUXE experiments from planar Sn target; 15 mJ for pre-pulse and 90 mJ for CO₂ laser [60]

As it can be seen from Figs. 81 and 82, the single CO₂ laser pulse system produces much more energetic Sn debris than the Nd:YAG due to the nature of energy deposition and the lower critical density for laser absorption. Hot front plasma created by the single CO₂ laser pulse produces ions with energy peaking around 3 keV. In the dual pulse case, the interaction of the CO₂ main laser pulse with the plasma created by the pre-pulse 266 nm laser helped dissipate the CO₂ main energy deeper into the pre-pulse plasma. The produced ions energy in the dual pulse system has a peak only around 30 eV. These unique results demonstrate the importance of detail inclusions of various processes in LPP devices during different phases of laser-target interactions.

Figures 83 and 84 show spatial distribution of kinetic energies of ions produced during interaction of CO₂ laser with pre-plasma created by Nd:YAG laser and with plasma developed by CO₂ laser in vacuum chamber conditions.

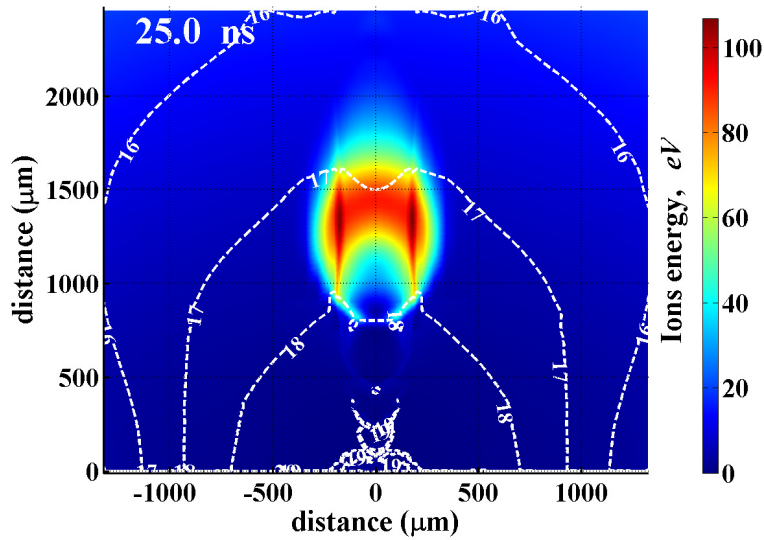


Fig. 83. Ions kinetic energies produced by CO₂ in pre-plasma created by Nd:YAG laser

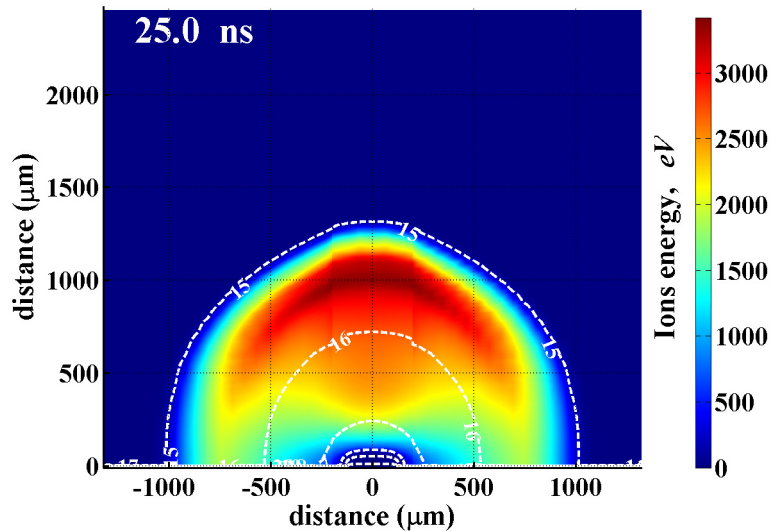


Fig. 84. Ions kinetic energies produced by CO₂ in vacuum chamber conditions

The interaction of Sn ion fluxes predicted from HEIGHTS simulation and verified by CMUXE experiments was then studied using the ITMC-DYN package. Several layers of MLM surface were considered consisted of 4.1 Si and 2.8 nm Mo alternating layers [67] with 3 nm Ru coating/capping layer at the surface [68].

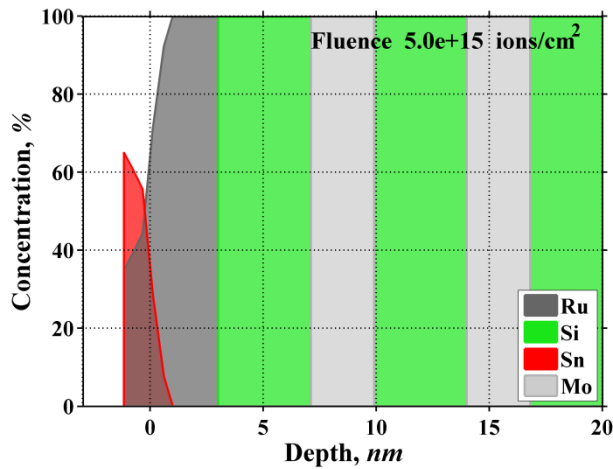


Fig. 85. MLM surface response to Sn ions with Gaussian distribution of energies around 50 eV [20]

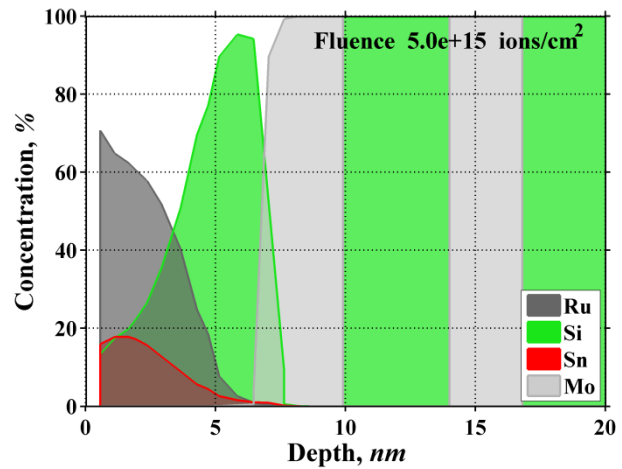


Fig. 86. MLM surface response to Sn ions with Gaussian distribution of energies around 2.5 keV [20]

In the case of dual-pulse system, the pre-pulse laser with relatively low intensity did not produce high fluence of energetic ions. In the developed mist plume the main CO₂ laser photons interacted mainly with plasma surrounded by relatively dense region that prevented producing ions with high kinetic energies. The single pulse device using CO₂ laser in vacuum conditions of the LPP chamber produced plasma with much more energetic ions that can cause serious damage of mirror layers. The damage to MLM surfaces, which reduces mirror reflectivity of EUV photons, can result from either surface deposition or erosion as well as interatomic mixing of the first few layers of MLM system. Ions with low energy will interact mainly with the first coating layer, due to Sn deposition on the surface, buildup, and mixing with Ru capping layer as illustrated in Fig. 85. However, ions with 1-3 keV energy can cause substantial erosion of Ru layer, tin implantation to deeper layers, and mirror interlayers mixing that can significantly degrade mirrors reflectivity as shown in Fig. 86.

3.4 Smallest efficient target and opportunities for EUV power increase

The use of smaller droplets with diameter up to 10 μm was studied in these simulations to predict the minimum size of droplet that is sufficient for production of the efficient EUV source with minimum debris creation.

3.4.1 Mass density requirement for the efficient EUV source

The utilization of pre-pulses for target preparation prior to main pulse has significantly increased CE of LPP sources employing small droplets. The highest CE for CO₂ lasers without pre-pulse with droplets of up to 50 μm is only $\sim 0.5\%$ [59]. Similar values were predicted using these HEIGHTS simulations. Variations in parameters of the CO₂ laser, i.e., increase of pulse intensity or spot size, do not significantly increase CE of such single pulse laser devices using small spherical targets. This is mainly due to the high reflection of 10.6- μm wavelength from solid/liquid tin, low critical density and therefore lower vaporization of droplet by CO₂ laser, and less containment of the evolved plasma plume to efficiently absorb and reabsorb (after reflection) laser photons due to the hydrodynamic motion of plasma around the droplet. The Nd:YAG laser gives higher CE from small droplets, up to 1.3%, however it is still much lower than the CE that can be obtained from planar targets.

The dependence of CE on the delay time between pulses, on main laser energy, and on spot size for dual-pulse systems was analyzed using 50- μm droplet as the initial target. Laser with 266 nm was used for initial mist creation from the 50- μm droplet. This laser vaporized about half of the droplet with the intensity of 2×10^{10} W/cm² and 20 ns duration. Target fragmentation can be neglected in this case and the target as single droplet can be considering during the pre-pulse laser and subsequent time of plume expansion since such low pre-pulse laser intensity cannot

cause significant droplet fragmentation [19]. Next, exploring various parameters of the main laser, it was found that 500 ns delay is an optimum time for mist expansion for efficient coupling with the incoming main CO₂ laser.

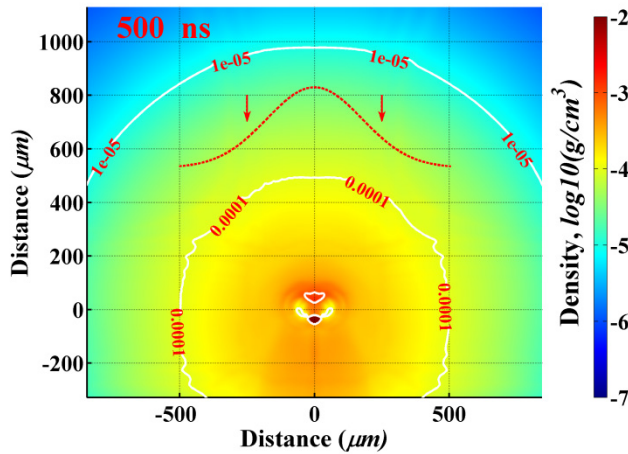


Fig. 87. Mass density distribution developed by 266 nm laser from 50 μm droplet at optimum delay time for efficient coupling with CO₂ laser with 500 μm spot size [20]

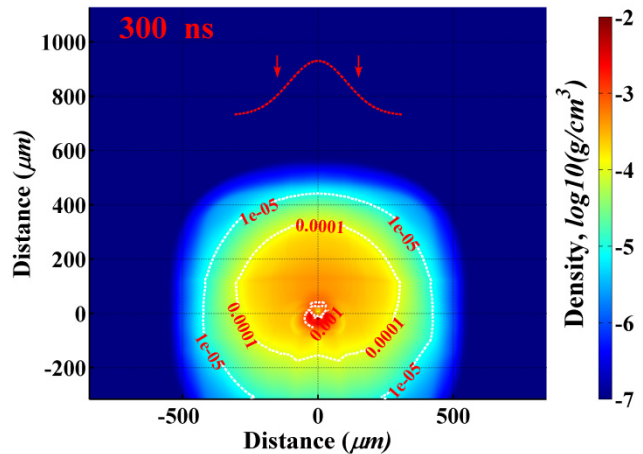


Fig. 88. Mass density distribution developed by 266 nm laser from 20 μm droplet at optimum delay time for efficient coupling with CO₂ laser with 300 μm spot size [20]

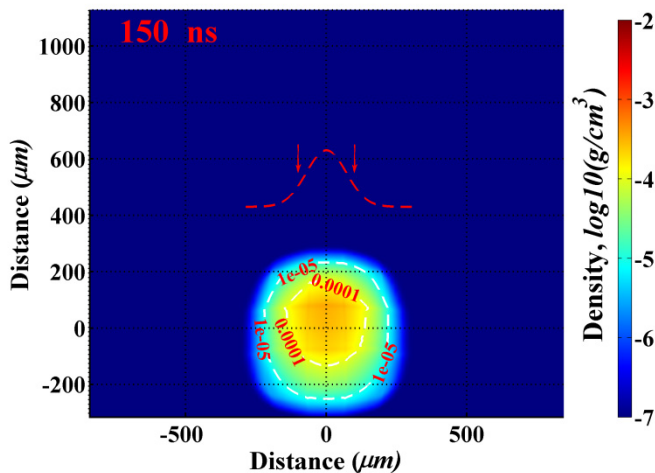


Fig. 89. Mass density distribution developed by 266 nm laser from 10 μm droplet at optimum delay time for efficient coupling with CO₂ laser with 200 μm spot size [20]

Comparative analysis of mass density for optimized EUV output obtained from 50 μm, 20 μm, and 10 μm droplets showed that mist plume should have density of the order of or higher

than 10^{-4} g/cm³ to prevent laser energy loss due to laser photons transmission through matter (Figs. 87-89).

A maximum CE of about 1.3% in the case of 10 μm droplet was obtained and Fig. 89 demonstrates that this value cannot be increased for such small target since the entire droplet was vaporized, mist was uniformly distributed, and plume matched the spot size of main laser that created the best possible conditions for EUV output from this droplet. This value is consistent with recent experimental result [59].

It was found that one of the main parameters for optimization of EUV output in dual-pulse devices with small, 10-20 μm droplets is pulse length of the main laser. Devices with CO₂ laser usually allow source operation using longer pulses (100 ns and more) without significant reduction in the efficiency of EUV output. However, simulations with the CO₂ heating of plasma/vapor mix, created from 20 μm droplet and expanded during 100–500 ns (Fig. 90), show dependence of the CE on pulse duration.

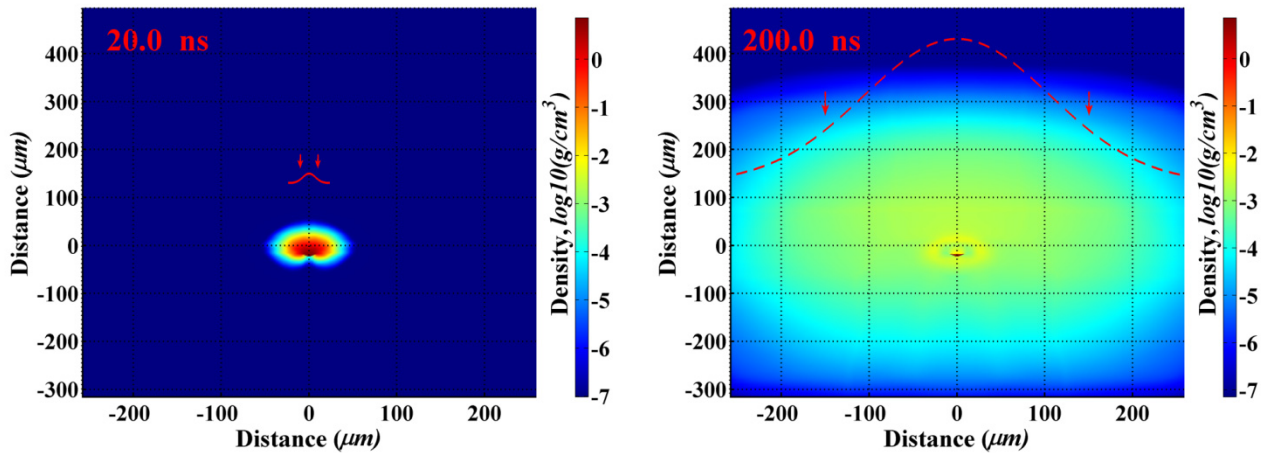


Fig.90. Mass density distribution after pre-pulse (10 ns FWHM) (left) and 200 ns delay (right). Pre-plasma was created from 20 μm droplet by laser beam with 266 nm wavelength and intensity of 2×10^{10} W/cm² [58]

The optimum duration of CO₂ laser beam was predicted, such as 10 or 20 ns (FWHM), to have maximum CE of about 2.8% from a target with 20 μm diameter (Fig. 91). The increase in pulse width to 30 ns resulted in the decrease of maximum CE to about 2 % due to low mass density for development of efficient photons source during the entire course of laser energy deposition.

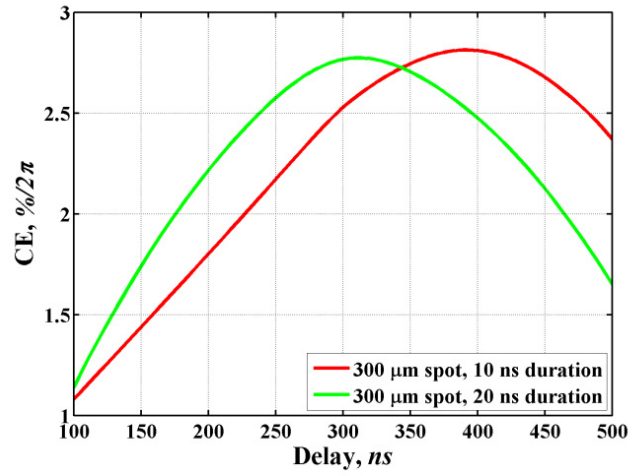


Fig.91. CE from 20 μm droplet as function of delay time between the pre-pulse and the main CO₂ laser pulse [58]

To further analyze the above requirements for mist density, the heating of a large 50-μm droplet by CO₂ laser was simulated assuming droplet fragmentation during the pre-pulse stage and fragments distribution to a surrounding volume within 300-μm diameter. Then, the effect of the background density on CE was studied. Fragments with size ~ 1 μm were randomly distributed in an ellipsoidal volume with the assumed surrounding plume of vapor/plasma. The volume of surrounding plume was varied. For the first time, the entire processes of laser interaction with the distributed fragments and with vapor/plasma was simulated, taking into account laser photons and plasma photons absorption, reflections, and reabsorption after reflection in liquid/vapor/plasma phases. These results showed the same tendency in the

requirements for background density, i.e., 10^{-4} g/cm³ mass density occupying volume of around 10^{-3} cm³, produced EUV source with 3.3% CE while 10^{-5} g/cm³ background density produced 2.1% maximum CE, that is the same as from planar target. Matching of laser spot size to the area of fragments distribution in radial direction is very important in the last case.

3.4.2 Potentials for EUV power increase

The potential use of the larger droplet size with higher laser power was also investigated to allow significant increase the EUV output at the intermediate focus. The EUV source size obtained from pre-plasma developed by 266 nm laser and distributed during 300 ns and 500 ns was calculated giving the optimum delay time for the considered 20- and 50- μ m droplets and pre-pulse parameters. Figures 92 and 93 show the EUV source size, location, and intensity (logarithmic values) collected in 5.5 sr during the main laser pulse in plasmas created from 50 μ m and 20 μ m droplets respectively. EUV energy of 11 mJ collected in 5.5 sr was obtained in the LPP system using the larger droplet and only 3.5 mJ using the smaller droplet. Taking into account industrial optical system parameters [59], EUV power of 600 W and 190 W respectively can be generated at the intermediate focus for 100 kHz laser system. This is very encouraging results for potential expansion to higher EUV power from current LPP system design.

Larger droplets do yield higher CE and offer an opportunity for substantial potential increase of source power. However, larger source sizes could have difficulties in efficient EUV photons collection due to current requirements for etendue of the optical system [64]. Also, debris produced from the non-vaporized part of the droplet can significantly decrease chamber components and optical system lifetime. Therefore, more detailed investigation of droplets with

sizes starting from 25 μm is needed to get efficient EUV source with minimum contamination and least damage to LPP chamber components.

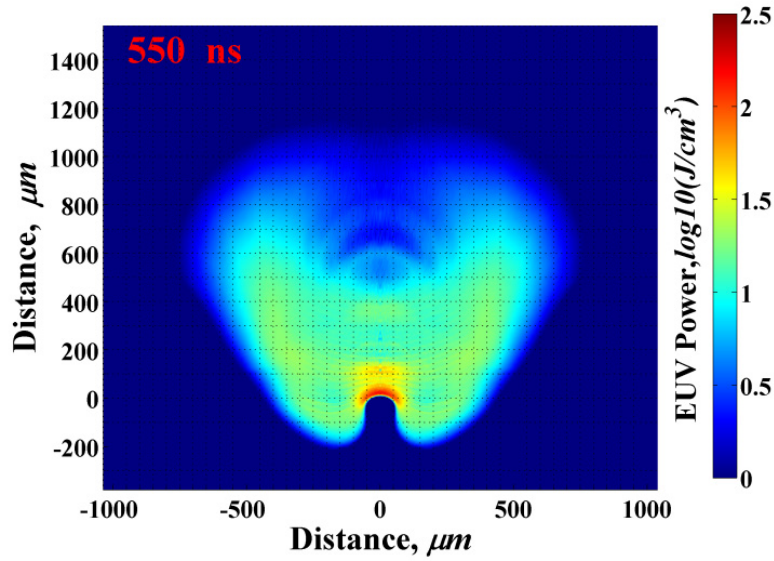


Fig. 92. EUV source from 50- μm droplet preheated by 266 nm laser and distributed during 500 ns. Main laser is CO_2 with 500 μm spot and 350 mJ [20]

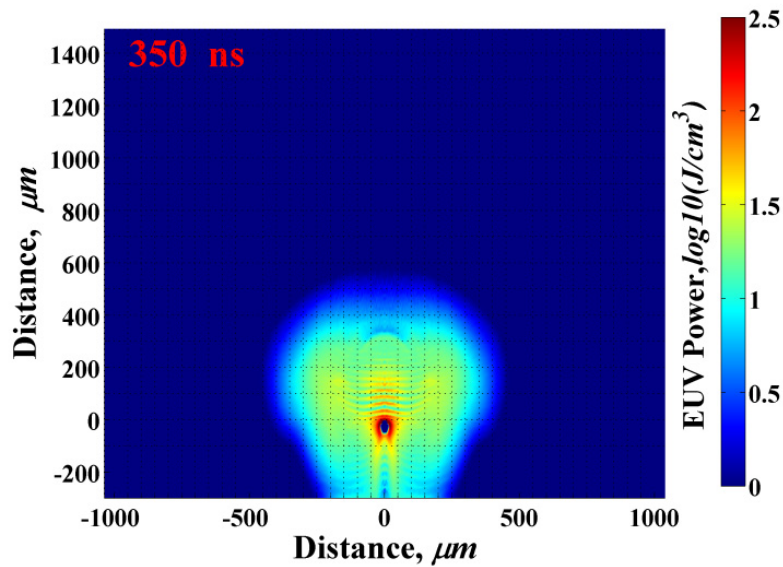


Fig. 93. EUV source from 20- μm droplet preheated by 266 nm laser and distributed during 300 ns. Main laser is CO_2 with 300 μm spot and 140 mJ [20]

4. SUMMARY

Photon sources for EUVL are still facing challenging problems to achieve high volume manufacturing in the semiconductor industry. The requirements for high EUV power, longer optical system and components lifetime, and efficient mechanisms for target delivery have narrowed investigators towards the development and optimization of dual-pulse laser sources with high repetition rate of small liquid tin droplets and the use of MLM optical system for collecting EUV photons.

This work summarizes results of comprehensive analysis of LPP processes, their effect on EUV photons emission and collection and the ways of EUV sources optimization. The work is based on the state-of-the art modeling and simulations using the HEIGHTS computer package. The package includes 3D description of all main processes occurred in LPP devices, that allows self-consistent advanced simulations and predictions without any fittings or adjustment parameters. This modeling and simulation included all phases of laser target evolution: from laser/droplet interaction, energy deposition, target vaporization, ionization, plasma hydrodynamic expansion, thermal and radiation energy redistribution, and EUV photons collection as well as detail mapping of photons source size and location. Testing and benchmarking results showed evidence of correct processes implementation. It showed also that accurate computer simulation with sufficient details can be used with confidence to understand, design, and optimize LPP plasma devices and save significant time and cost compared to conducting numerous expensive experiments.

The author of this thesis contributed significantly to the development of the HEIGHTS comprehensive package, physical models of target response and plasma formation, and utilized

the developed models for analysis of laser-produced plasma (LPP) systems as potential light sources for extreme ultraviolet lithography (EUVL).

The main specific contributions to the models development include:

- Implementation of model for target vaporization based on the surface atoms kinetics;
- Development of models for hydrodynamics and thermal conduction for two-component plasma to simulate plasma evolution in presence of ambient gas;
- Development and improvement of algorithms for parallel calculations on multi-processor computers;
- Models benchmarking and debugging for various geometries;
- Upgrade of ITMC-DYN (Ion Transport in Materials & Compounds-Dynamic Version) - Monte Carlo based package designed for simulation of ions/target interactions. This upgrades included modeling of dynamic update of target composition during interaction processes, particles diffusion, chemical erosion, surface segregation, molecular recombination and desorption of gaseous species from the surface. One main purpose of this development was done to study the effect of energetic ions produces in LPP devices on the photon collection optical mirror system.

An ideal target is to generate the source of maximum EUV radiation output and collection in the $13.5 \pm 1\%$ nm range with minimum atomic debris. The effect of target mass and size, laser parameters, and dual pulse system configuration on EUV radiation output and on atomic and ionic debris generation was studied during the course of this thesis work to obtain the ideal target. The potential damage to the optical mirror collection system from plasma thermal and energetic debris and the requirements for mitigating systems to reduce debris fluence were also simulated and predicted.

The main contributions of the author of this thesis to the analysis of plasmas in LPP systems and following optimization of EUV sources include:

- Comprehensive self-consistent analysis of plasma physics processes and plasma behavior in various LPP systems;
- Thorough and systematic evaluation and optimization of parameters in LPP devices which influence EUV photons production and collection;
- Prediction, for the first time, of location, intensity and size of EUV source in LPP systems;
- Detailed simulation, for the first time, of the output power limits from the smallest possible spherical targets for the most efficient EUV source;
- Proposition, for the first time, of fourth harmonic of Nd:YAG laser as the most efficient way for target preparation in dual-laser beam systems;
- Explanation, for the first time, of many worldwide experimental results, which were obtained before and after models prediction. These include effect of longer laser wavelengths in combination with small targets on having low efficiency of LPP source; effect of target geometry on the CE of LPP systems; and the effect of delay time between pulses in dual-beam laser systems on plasma characteristics and requirements for the second laser parameters to produce the highest CE;
- Prediction, for the first time, opportunities for potential increase in source power (critical for economic impact of the semiconductor industry) and the challenges related to such source power increase;
- Prediction of degradation of the optical multi-layer mirror systems for EUV photons collection in various LPP systems.

LPP sources using different 10-100 μm tin droplet targets, as single droplets as well as distributed microdroplets with equivalent mass were studied and analyzed to predict mass dependence, laser parameters requirements, atomic and ionic debris generation, and to optimize EUV radiation output. The main practical results of this study and analysis are the following:

- Small targets size, 10-50 μm , in LPP devices with single laser beam leads to the significant decrease in the efficiency of EUV photons production. This is more pronounced in devices with CO₂ laser since its longer wavelength, 10.64 μm . CO₂ laser has higher reflectivity from the solid/liquid target, less critical density value, therefore it produces less dense plasma that influences geometrical containment and development of efficient conditions for EUV output.
- Dual-pulse systems allow increasing efficiency of LPP devices with small droplets. Mainly Nd:YAG lasers can be used for the first stage, pre-plasma development, since they have better absorption in solid and liquid matter and have higher critical density. The CO₂ laser can then be the best choice for the second stage, i.e., EUV production stage, since the evolving plasma plumes are more suitable for the absorption of such longer laser wavelength.
- The fourth harmonic of Nd:YAG lasers, 266 nm wavelength, is the best choice for preparing the plume mist before the main pulse. Application of this laser results in higher vaporization rate and lower temperatures of plasma plume. The higher vaporization rate allows near complete droplet vaporization and the lower temperatures of plasma plume reduce the fluence and energy of ions debris.
- Devices with CO₂ laser usually allow source operation using longer pulses (100 ns and more) without significant reduction in the efficiency of EUV output. However, simulations

with the CO₂ heating of plasma/vapor mix, created from 10-20 μm droplets, showed dependence of the CE on pulse duration.

- The plasma created from 10 μm droplet or smaller may not be an efficient source. The maximum obtained CE was about 1.3% with optimized pulse duration of 10 ns and spot size of 200 μm. This value is consistent with recent experimental result.
- Larger droplet, 50 μm for example, can result in higher CE and offer reasonable pathway for potential increase in source power. However, larger source sizes may have difficulties in efficient EUV photons collection within the given etendue limits.
- Therefore, more detailed investigation of droplets with sizes starting from 25 μm is needed for designing efficient EUV sources with minimum debris contamination and least damage to LPP chamber components.
- The ITMC-DYN simulation showed that ions with low energy, in the order of 30-50 eV, would interact only with first coating layer through Sn deposition on the surface and mixing with Ru capping layer. Energetic ions having 2-3 keV kinetic energy can however, cause severe erosion of Ru layer, tin implantations to deeper layers, and layers mixing at interface of the MLM system. This can cause significant degradation and loss of mirrors reflectivity.

These developments and findings were published in several high-quality high-impact physical journals during the course of this thesis work. Recent publications include:

1. A. Hassanein and **T. Sizyuk**, "Laser produced plasma sources for nanolithography: Recent integrated simulation and benchmarking", *Physics of Plasmas* 20 *Art. No.* 053105 (2013).
2. **T. Sizyuk** and A. Hassanein, "The role of plasma evolution and photon transport in optimizing future advanced lithography sources", *Journal of Applied Physics* 114, 083109 (2013).

3. A. Hassanein and **T. Sizyuk**, "Design and Optimization of Laser Produced Plasma Devices for Nanolithography", *Advances in Applied Plasma Science*, Vol.9 (2013).
4. **T. Sizyuk** and A. Hassanein, (2012) "Optimization of extreme ultraviolet photons emission and collection in mass-limited laser produced plasmas for lithography application", *Journal of Applied Physics* 112 *Art. No.*033102.
5. **T. Sizyuk** and A. Hassanein, (2012) "Enhancing EUV photons emission in laser produced plasmas for advanced lithography", *Physics of Plasmas* 19 *Art. No.*083102.

The main results of this analysis were presented at several important conferences:

1. A. Hassanein and **T. Sizyuk**, "Advances in computer simulations of LPP sources for EUV Lithography", SPIE Advanced Lithography conference, San Jose, USA (February 2013).
2. **T. Sizyuk** and A. Hassanein, "Important processes in modeling and optimization of EUV lithography sources", SPIE Advanced Lithography conference, San Jose, USA (February 2013).
3. **T. Sizyuk** and A. Hassanein, "Comprehensive self-consistent 3-D modeling of laser induced target vaporization and crater formation", 7th International Conference on Laser Induced Breakdown Spectroscopy in Luxor, Egypt (September 2012). Invited Talk.
4. **T. Sizyuk** and A. Hassanein, "Modeling and optimization of mass-limited targets for EUV lithography", SPIE Advanced Lithography conference, San Jose, USA (February 2012).
5. A. Hassanein, V. Sizyuk and **T. Sizyuk**, "Computer simulation of hydrodynamics and radiation transport processes for Advanced Lithography applications", 8th International Symposium on Applied Plasma Science, ISAPS `11 Hakone, Japan (09/2011).
6. **T. Sizyuk** and A. Hassanein, "HEIGHTS Simulation and Optimization of Laser Produced Plasma EUV Sources", 2011 IEEE International Conference on Plasma Science - ICOPS 2011, Chicago.
7. A. Hassanein, **T. Sizyuk**, V. Sizyuk, and S. S. Harilal, "Combined effects of pre-pulsing and target geometry on efficient EUV production from laser produced plasma experiments and modeling", SPIE Advanced Lithography conference, San Jose, USA (February 2011).

5. REFERENCES

1. G.E. Moore, "Cramming More Components Onto Integrated Circuits," *Electronics*, 38 (8), 114 (1965).
2. H.J. Levinson, *Principles of Lithography*, SPIE PRESS, Bellingham, Washington (2001).
3. B. Fay, "Advanced optical lithography development, from UV to EUV", *Microelectron. Eng.*, 61-62, 11 (2002).
4. K. Ota, et al., in *EUV Sources for Lithography*, edited by V. Bakshi (ed.), SPIE Press, Bellingham, Washington, USA, Chapter 9, 277-298 (2006).
5. D. C. Brandt, I. V. Fomenkov, A. I. Ershov, D. W. Myers, D. J. Brown, B. M. La Fontaine, M. J. Lercel, A. N. Bykanov, N. R. Bowering, Cymer Inc., "Laser-produced plasma EUV sources for device development and HVM", Proc. SPIE 8322, Extreme Ultraviolet (EUV) Lithography III, 83221I (2012).
6. A. Hassanein, et al., in *EUV Sources for Lithography*, edited by V. Bakshi (ed.), SPIE Press, Bellingham, Washington, USA, Chapter 9, 277-298 (2006).
7. U. Stamm, et al., "High-power EUV lithography sources based on gas discharges and laser-produced plasmas", Proc. of SPIE vol. 5037, 5037-119 (2003).
8. T. Higashiguchi, K. Kawasaki, W. Sasaki and S. Kubodera, "Enhancement of extreme ultraviolet emission from a lithium plasma by use of dual laser pulses", *Appl. Phys. Lett.* 88, 161502 (2006).
9. J. R. Hoffman, A. N. Bykanov, O. V. Khodykin, A. I. Ershov, N. R. Bowering, I. V. Fomenkov, W. N. Partlo, and D. W. Myers, "LPP EUV conversion efficiency optimization," Proc. SPIE 5751, 892–901 (2005).
10. J. Fujimoto, T. Yanagida, T. Ohta, Y. Kawasuji, Y. Shiraishi, T. Abe, T. Kodama, H. Nakarai, T. Yamazaki, H. Mizoguchi, "Development of laser-produced plasma-based EUV light source technology for HVM EUV lithography", Proc. of SPIE vol. 8322, 83220F (2012).
11. K. Koshelev, V. Krivtsun, V. Ivanov, O. Yakushev, A. Chekmarev, V. Koloshnikov, E. Snegirev, V. Medvedev, "New type of discharge-produced plasma source for extreme ultraviolet based on liquid tin jet electrodes", *J. Micro/Nanolith. MEMS MOEMS* 11(2), 021103 (Apr–Jun 2012).
12. V. Sizyuk, A. Hassanein, V. Morozov, V. Tolkach, T. Sizyuk, "Numerical simulation of laser-produced plasma devices for EUV lithography using the heights integrated model", *Numerical Heat Transfer Part A* 49, 215-236 (2006).
13. G. O'Sullivan and P. K. Carroll, "4d–4f emission resonances in laser produced plasmas," *J. Opt. Soc. Am.* 71, 227–230 (1981).
14. T. Tomie, "Tin laser-produced plasma as the light source for extreme ultraviolet lithography high-volume manufacturing: history, ideal plasma, present status, and prospects", *J. Micro/Nanolith. MEMS MOEMS* 11(2), 021109 (Apr–Jun 2012).
15. G. D. Kubiak et al., "Debris-free EUVL sources based on gas jets," *OSA trends in Optics and Photonics* 4 in *Extreme Ultraviolet Lithography*, D. Kubiak and D. R. Kania, Eds., OSA, pp. 66–71 (1996).

16. R.C. Spitzer, T.J. Orzechowski, D.W. Phillion, R.L. Kauffman, and C. Cerjan, "Conversion efficiencies from laser-produced plasmas in the extreme ultraviolet regime", *J. Appl. Phys.* 79 (5) 2251-2258 (1996).
17. G. Schriever, O. Semprez, J. Jonkers, M. Yoshioka, R. Apetz, "Laser-produced plasma versus laser-assisted discharge plasma: physics and technology of extreme ultraviolet lithography light sources", *J. Micro/Nanolith. MEMS MOEMS* 11(2), 021104 (Apr–Jun 2012).
18. A. Hassanein, T. Sizyuk, V. Sizyuk, S. Harilal, "Combined effects of repulsing and target geometry on efficient extreme ultraviolet production from laser produced plasma experiments and modeling", *J. Micro/Nanolith. MEMS MOEMS* 10(3), 033002 (Jul–Sep 2011).
19. S. Fujioka, M. Shimomura, Y. Shimada, S. Maeda, H. Sakaguchi, Y. Nakai, T. Aota, H. Nishimura, N. Ozaki, A. Sunahara, K. Nishihara, N. Miyanaga, Y. Izawa, K. Mima, "Pure-tin microdroplets irradiated with double laser pulses for efficient and minimum-mass extreme-ultraviolet light source production", *Appl. Phys. Lett.* 92, 241502 (2008).
20. A. Hassanein and T. Sizyuk, "Laser produced plasma sources for nanolithography - recent integrated simulation and benchmarking", *Phys. Plasmas* 20, 053105 (2013).
21. A. Hassanein, V. Sizyuk, T. and Sizyuk, "Multidimensional simulation and optimization of hybrid laser and discharge plasma devices for EUV lithography", *Proc. of SPIE* vol. 6921, 692113-1 (2008).
22. H. Shields, S.W. Fornaca, M.B. Petach, M. Michaelian, D.R. Mcgregor, R.H. Moyer, R.J. St. Pierre, "Xenon target performance characteristics for laser-produced plasma EUV sources," *Proc. SPIE* 4688, 94 (2002).
23. G. O'Sullivan, A. Cummings, P. Dunne, P. Hayden, L. McKinney, N. Murphy, and J. White, "Chapter 5: atomic physics of highly charged ions and the case for Sn as a source material," in *EUV Source for Lithography*, edited by V. Bakshi (SPIE, Bellingham, WA, USA 2006).
24. P.-E. Nica, S. Miyamoto, S. Amano, T. Inoue, A. Shimoura, K. Kaku, and T. Mochizuki, "Soft x-ray spectra from laser heated lithium targets," *Appl. Phys. Lett.*, 89, 041501 (2006).
25. T. Abe, T. Suganuma, Y. Imai, Y. Sugimoto, H. Someya, H. Hoshino, G. Soumagne, H. Komori, H. Mizoguchi, A. Endo, and K. Toyoda, "Development of liquid-jet laser-produced plasma light source for EUV lithography," *Proc. SPIE*, 5037, 776 (2003).
26. K. Nagai, Q. Gu, T. Norimatsu, S. Fujioka, H. Nishimura, N. Miyanaga, K. Nishihara, Y. Izawa, and K. Mima, "Nano-structured lithium-tin plane fabrication for laser produced plasma and extreme ultraviolet generation," *Laser Part. Beams*, 26, 497 (2008).
27. T. Nishikawa, A. Sunahara, A. Sasaki, and K. Nishihara, "EUV Source Design Flexibility for Lithography," *J. Phys.: Conf. Ser.*, 112, 042065 (2008).
28. S. Dusterer, H. Schwoerer, W. Ziegler, D. Salzmann, R. Sauerbrey, "Effects of a prepulse on laser-induced EUV radiation conversion efficiency", *Appl. Phys. B* 76, 17-21 (2003).
29. R. de Bruijn, K.N. Koshelev, S.V. Zakharov, V.G. Novikov, F. Bijkerk, "Enhancement of laser plasma extreme ultraviolet emission by shockwave–plasma interaction," *Phys. Plasma* 12, 042701 (2005).

30. L.R. Hoffman, A.N. Bykanov, O.V. Khodykin, A.I. Ershov, N.R. Bowering, I.V. Fomenkov, W.N. Partlo, D.W. Myers, “LPP EUV Conversion Efficiency Optimization”, Proc. SPIE 5751, 892 (2005).
31. B. A. M. Hansson and H. M. Hertz, “Liquid-jet laser-plasma extreme ultraviolet sources: from droplets to filaments”, J. Phys. D: Appl. Phys., 37, 3233–3243 (2004).
32. S. Yuspeh, K.L. Sequoia, Y. Tao, M.S. Tillack, R. Burdt, and F. Najmabadi, “Optimization of the size ratio of Sn sphere and laser focal spot for an extreme ultraviolet light source”, Appl. Phys. Lett., 93, 221503 (2008).
33. S. Fujioka, H. Nishimura, T. Okuno, Y. Tao, N. Ueda, T. Ando, H. Kurayama, Y. Yasuda, S. Uchida, Y. Shimada, M. Yamaura, Q. Gu, K. Nagai, T. Norimatsu, H. Furukawa, A. Sunahara, Y.-G. Kang, M. Murakami, K. Nishihara, N. Miyanaga, Y. Izawa, “Properties of EUV and particle generations from laser-irradiated solid- and low-density tin targets”, Proc. SPIE 5751, 578 (2005).
34. P. Hayden, A. Cummings, N. Murphy, G. O’Sullivan, P. Sheridan, J. White, and P. Dunne, “13.5 nm extreme ultraviolet emission from tin based laser produced plasma sources”, J.Appl.Phys., 99, 093302 (2006).
35. L.D. Landau, E.M. Lifshits, The classical theory of fields, Butterworth Heinemann, Oxford (England), (1995).
36. G. V. Miloshevsky, V. A. Sizyuk, M. B. Partenskii, A. Hassanein, and P. C. Jordan, “Application of finite-difference methods to membrane-mediated protein interactions and to heat and magnetic field diffusion in plasmas”, J. Comp. Phys. 212, 25 (2006).
37. V. M. Kovenya, S. G. Cherny, and A. S. Lebedev, in Computational Fluid Dynamics, edited by G.S. Davis and C. Fletcher (North-Holland, Amsterdam, 1988).
38. G. G. Grigoryan, A. G. Leonov, E. A. Manykin, A. A. Rudenko, M. G. Sitnikov, and A. N. Starostin, Journal of Experimental and Theoretical Physics 97, 678–687 (2003).
39. T. W. Johnston and J. M. Dawson, Phys. Fluids 16, 722 (1973).
40. L. Spitzer, Physics of Fully Ionized Gases, 2nd edition, Interscience Publishers, New York, (1962).
41. A. Hassanein, G. L. Kulcinski, and W. G. Wolfer, “Surface melting and evaporation during disruptions in Magnetic Fusion Reactors”, Nucl. Eng. Des. Fusion 1, 307-324 (1984).
42. A. Unsöld, Physik der Sternatmosphären, Springer-Verlag, Berlin, (1938). (in Germany)
43. Ya. Zeldovich and Yu. Raizer, Physics of Shock Waves and High-Temperature Hydrodynamics Phenomena, Vol. 1, Academic Press, New York and London, (1966).
44. R. Siegel and J. Howell, Thermal Radiation Heat Transfer, Hemisphere Publishing Corp., Washington, New York, London, (1981).
45. V. Tolkach, V. Morozov, and A. Hassanein, Report No. ANL-ET/02-23 (Argonne National Laboratory, 2002).
46. V. Morozov, V. Tolkach, and A. Hassanein, Report No. ANL-ET-04/24 (Argonne National Laboratory, 2004).

47. A. Hassanein, D.L. Smith, "Elastic and inelastic surface effects on ion penetration in solids and resulting sputtering and backscattering", Nucl. Instrum. Method B 13, 225 (1986).
48. T. Sizyuk and A. Hassanein, "Dynamic analysis and evolution of mixed materials bombarded with multiple ions beams", J. Nucl. Mater. 404, 60-67 (2010).
49. V. Sizyuk, A. Hassanein, and T. Sizyuk, "Hollow laser self-confined plasma for extreme ultraviolet lithography and other applications", Laser and Particle Beams 25, 143-154 (2007).
50. G. Soumagne, et al., "Combined Nd:YAG -CO₂ Laser Produced Plasma EUV Source Examination with the Code Z", EUV Source Workshop, Baltimore, USA (2007).
51. A. Hassanein, V. Sizyuk, T. Sizyuk, S. Harila, "Effects of plasma spatial profile on conversion efficiency of laser-produced plasma sources for EUV lithography", J. Micro/Nanolith. MEMS MOEMS 8(4) 041503 (Oct–Dec 2009).
52. V. Sizyuk, A. Hassanein, and T. Sizyuk, "Three-dimensional simulation of laser-produced plasma for extreme ultraviolet lithography applications", J. Appl. Phys. 100, 103106 (2006).
53. Nishimura, H., Fujioka, S., Shimomura, M., Sakaguchi, H., Nakai, Y., Aota, T., Kai, T., Nishihara, K., Miyahara, N., Izawa, Y., Mima, K., Sunahara, A., Shimada Y., and Namba, S., "Development of Extreme-Ultraviolet Light Source by Laser-Produced Plasma", The Review of Laser Engineering, Vol. 36, 1125 (2008).
54. S. S. Harilal, T. Sizyuk, V. Sizyuk, and A. Hassanein, "Efficient laser-produced plasma EUV sources using grooved Sn targets", Applied Physics Letters 96 111503 9 (2010).
55. V.Y. Banine, K.N. Koshelev, G.H.P.M. Swinkels, J. Phys. D Appl. Phys. 44, 253001 (2011).
56. A. Hassanein, V. Sizyuk, S.S. Harilal, and T. Sizyuk, "Analysis, simulation, and experimental studies of YAG and CO₂ laser-produced plasma for EUV lithography sources", Proc. of SPIE vol. 7636, 76360A (2010).
57. T. Sizyuk and A. Hassanein, "Enhancing EUV photons emission in laser produced plasmas for advanced lithography", Phys. Plasmas 19, 083102 (2012).
58. T. Sizyuk and A. Hassanein, "Optimization of extreme ultraviolet photons emission and collection in mass-limited laser produced plasmas for lithography application", J. Appl. Phys. 112, 033102 (2012).
59. H. Mizoguchi, T. Abe, Y. Watanabe, T. Ishihara, T. Ohta, T. Hori, T. Yanagida, H. Nagano, T. Yabu, S. Nagai, G. Soumagne, A. Kurosu, K. M. Nowak, T. Suganuma, M. Moriya, K. Kakizaki, A. Sumitani, H. Kameda, H. Nakarai, J. Fujimoto, Proc. SPIE 7969, 7969-08 (2011).
60. J.R. Freeman, S.S. Harilal, A. Hassanein, B. Rice, "Effect of prepulse laser wavelength on EUV emission from CO₂ reheated laser-produced Sn plasma", Applied Physics A 110, 853-856 (2013).
61. T. Sizyuk and A. Hassanein, "The role of plasma evolution and photon transport in optimizing future advanced lithography sources", J. Appl. Phys. 114, 083109 (2013).
62. A. Hassanein and T. Sizyuk, "Design and Optimization of Laser Produced Plasma Devices for Nanolithography", Advances in Applied Plasma Science, Vol.9 (2013).
63. Tao, Y., Tillack, M. S., Sequoia, K. L., Burdt, R. A., Yuspeh, S., and Najmabadi, F., "Efficient 13.5 nm extreme ultraviolet emission from Sn plasma irradiated by a long CO₂ laser pulse", Applied Physics Letters 92, 251501 (2008).
64. Bakshi, V., "EUV Source Technology: Challenges and Status", EUV Sources for Lithography, ed. V. Bakshi, SPIE Press, 2005, 7.

65. A. Endo, Proc. 2011 International Workshop on EUV and Soft X-Ray Sources, Ireland, (November 7-10, 2011).
66. K. Nishihara, A. Sunahara, A. Sasaki, M. Nunami, H. Tanuma, S. Fujioka, Y. Shimada, K. Fujima, H. Furukawa, T. Kato, F. Koike, R. More, M. Murakami, T. Nishikawa, V. Zhakhovskii, K. Gamata, A. Takata, H. Ueda, H. Nishimura, Y. Izawa, N. Miyanaga, K. Mima, Phys. Plasmas 15, 056708 (2008).
67. V. Bakshi, EUV Lithography, by V. Bakshi (ed.), SPIE Press, Bellingham, Washington, USA, Chapter 7, 333 (2009).
68. S. Bajt, et al., J. Microlith., Microfab., Microsyst. 5(2), 023004 (Apr–Jun 2006).